

Probing the Top-Higgs Sector with Composite Higgs Models at Present and Future Hadron Colliders

Carlos Bautista,^{1,2} Leonardo de Lima,³ Ricardo D'Elia Matheus,¹ Eduardo Pontón,^{1,2,5} Leônidas A. Fernandes do Prado,^{1,4} and Aurore Savoy-Navarro⁴

¹Instituto de Física Teórica – UNESP, São Paulo, Brazil

²ICTP South American Institute for Fundamental Research, São Paulo, Brazil

³Universidade Tecnológica Federal do Paraná, Toledo, Brazil

⁴IRFU-CEA, Université Paris-Saclay and CNRS-IN2P3, France

E-mail: carlos.bautista@unesp.br, leonardolima@utfpr.edu.br,
matheus@ift.unesp.br, leonidas.prado@cern.ch, aurore.savoy.navarro@cern.ch

Abstract. We study the production of $t\bar{t}h$ and $t\bar{t}hh$ at hadron colliders, in the minimal Composite Higgs Models, based on the coset $SO(5)/SO(4)$. We explore the fermionic representations **5** and **14**. A detailed phenomenological analysis is performed, covering the energy range of the LHC and its High Luminosity upgrade, as well as that of a future 100 TeV hadron collider. Both resonant and non-resonant production are considered, stressing the interplay and complementary interest of these channels with each other and double Higgs production. We provide sets of representative points with detailed experimental outcomes in terms of modification of the cross sections as well as resonance masses and branching ratios. For non-resonant production, we gauge the relative importance of Yukawa, Higgs trilinear, and contact $t\bar{t}hh$ vertices to these processes, and consider the prospect for distinguishing the fermion representations from each other and from the Standard Model. In the production of top partners, we find that the three-body decay channel W^+W^-t becomes significant in certain regions of parameter space having a degenerate spectrum, and is further enhanced with energy. This motivates both higher energy machines as well as the need to go beyond the current analysis performed for the searches for these resonances.

⁵Eduardo greatly contributed to the work here presented but sadly passed away in the early stages of the writing of this paper. He will be sorely missed.

Contents

1	Introduction	1
2	The Higgs as a Pseudo-Nambu Goldstone Boson	3
2.1	The Fermion Sector of the MCHM ₅	4
2.2	The Fermion Sector of the MCHM ₁₄	7
2.3	Partial Compositeness and Higgs Couplings	8
2.4	Higgs Decays	10
3	Phenomenological Analysis Strategy	12
3.1	Parameter Space	12
3.2	MCHM Scales, low versus high	14
3.2.1	Definition of the ranges for the Low Scale parameters	15
3.2.2	Definition of the ranges for the High Scale parameters	15
3.3	Simple Physical Observables	15
3.4	Strategy to select example points and benchmark points	17
3.5	Implementation of both MCHM models into the Event Generator	19
3.6	The $t\bar{t}h$ Process	19
3.7	The $t\bar{t}hh$ Process	20
3.7.1	The Non-Resonant $t\bar{t}hh$ Process	21
3.8	Operators Analysis	22
3.8.1	Effect on the $t\bar{t}h$ Process	22
3.8.2	Effect on the $t\bar{t}hh$ Process	22
4	MCHM at Low Scale	25
4.1	Scanning Over Parameter Space	25
4.2	Selection of some example points for each MCHM scenario	29
4.2.1	Selected example points and their main features for the MCHM ₅	30
4.2.2	Selected example points and their main features for the MCHM ₁₄	32
4.2.3	NR- $t\bar{t}hh$ contributions in the MCHM ₅ and the MCHM ₁₄	33
4.3	Cluster Analysis applied to the MCHM at low scale	36
4.3.1	Clustering of the MCHM ₅	36
4.3.2	Clustering of the MCHM ₁₄	40
5	MCHM at High Scale	42
5.1	Scanning Over Parameter Space	43
5.2	Cluster analysis applied to the MCHM at High scale	46
5.2.1	Clustering of the MCHM ₅	46
5.2.2	Clustering of the MCHM ₁₄	48
6	Effective Field Theory Perspective	51
7	Conclusions and Outlook	54

A	Representations of $SO(5)$	56
B	Embeddings of $SO(4)$ into $SO(5)$	58
C	Explicit form of gauge and Higgs interactions	60

1 Introduction

The discovery of the Higgs boson [1, 2], has aroused the interest in measuring with high precision the Higgs properties. This has led to greater emphasis on a strong joint effort between theory and experiments to explore the Higgs sector. The Large Hadron collider, LHC, at CERN, which is also a Top factory, offers an unique playground to perform the searches in the Top-Higgs sector both now and with its upgrade into the High-Luminosity LHC.

Besides, the importance of knowing in depth the Higgs sector, led to studying a Higgs factory as the next machine in Particle Physics as well as the importance of a very high energy hadron collider. While all current measurements within their present precision are consistent with a Standard Model (SM) Higgs boson, there is room for deviations from the SM that could hold the key to a deeper understanding of the phenomenon of electroweak symmetry breaking (EWSB). Furthermore, as the luminosity increases and experiments are progressively upgraded, a number of Higgs-related processes are becoming more and more accessible, in the next years to come. An important open question is whether the observed 125 GeV scalar is a composite bound state of more fundamental constituents, or whether it is elementary down to distances much shorter than currently explored. The experimental program will be essential in illuminating this fundamental question.

The idea of Higgs compositeness received an important boost with the construction of rather complete models that can be consistent with all current measurements [3]. Such constructions incorporated a geometric solution to the hierarchy problem [4], a dynamical mechanism for EWSB, and an appealing understanding of the flavor structure observed in the SM. In these scenarios, the Higgs boson is understood as a pseudo-Nambu Goldstone boson (pNGB), somewhat analogous to the pions in QCD, but also with important differences. While much model building and extensions have been proposed in the literature, in this work we focus on the minimal setup, based on the symmetry breaking pattern $SO(5) \rightarrow SO(4)$. These are referred to as “Minimal Composite Higgs Models” (MCHM).

It is known that there is considerable model-dependence associated with the fermion sector of the MCHM, which is of relevance to our work. In particular, the top sector is expected to play a crucial role in these models, given that the top quark couples most strongly to the Higgs boson. We focus on the production of one or two Higgs bosons in association with a top/anti-top pair. The $t\bar{t}h$ cross section is being actively measured [5, 6], in many different channels, with values compatible with the SM prediction, within approximately 20% uncertainty. An experimental search for the $t\bar{t}hh$ process has been just performed, for the first time at the LHC [7]. Such a process is of particular interest in the present class of models, due to the generic prediction of charge 2/3 vectorlike “top

partners” that can decay in the th channel, thus leading to the previous final state. These resonances are already constrained by previous searches in this channel [8] as well as in combination with tZ and bW decay channels [9, 10].

Since the top partner resonances are under active search with already defined bounds above 1 TeV, we bring here attention to the fact that frequently a large fraction of the $t\bar{t}hh$ cross section is composed of non-resonant production, which then becomes an important discriminator for the MCHM models. This component is also more directly related to the pNGB nature of the Higgs boson, unlike the vectorlike fermionic resonances. This work highlights the complementary role between non-resonant $t\bar{t}hh$ production and the $t\bar{t}h$ and hh channels, specially in terms of measuring the trilinear Higgs couplings. We gauge the relative importance of Yukawa, trilinear Higgs and new contributions to the non-resonant $t\bar{t}hh$ channel, accessing quantitatively the correlation between $t\bar{t}h$ and $t\bar{t}hh$ cross sections.

To illustrate the interest and importance of these two processes for the Higgs sector and within the Composite Higgs context, this work presents a phenomenological analysis at the parton level, with two specific realizations of the MCHM, in the framework of the present and future hadron colliders.

The goal is to establish phenomenological differences between a model with minimal embedding of fermions (the MCHM₅) and the simplest one that can allow for an increased top Yukawa coupling (the MCHM₁₄). We also provide sets of representative points with a large coverage of the parameter space of those models. Beyond these two specific MCHM realizations used as a showcase to scan and thus explore experimentally the MCHM, we link these two cases to the effective field theory (EFT) applicable in the limit of decoupled resonances. To do so and complete this study, we also present our results in terms of modifications to the SM couplings which are more directly comparable to experiment.

Therefore this overall study can be used to guide searches for new physics, bridging the BSM phenomenological and experimental goals. Indeed, starting from the current results being achieved at the LHC (and promptly evolving), this study provides some defined directions and predictions to look for, over the next decades, at the 14 TeV High Luminosity phase of the LHC and at a future High energy Hadron collider in the range of 100 TeV to possibly 150 TeV, as in the proposed FCC-hh at CERN and SppC in China [11–13].

The features of the composite Higgs scenarios directly relevant for this work are reviewed in Section 2. Section 3 sets the overall phenomenological analysis strategy. It includes the definition of the parameter space for the two MCHM scales considered in this work, the simple physical observables relevant here, the strategy and tools to extract the representative points in the parameter space, the implementation of both models into the event generator and the operator analysis with its effects on the $t\bar{t}h$ and $t\bar{t}hh$ processes. The MCHM low scale scenario is described in Section 4 with the corresponding sets of representative points in both models, their detailed experimental outcomes in terms of modification of the cross-sections, of the non-resonant components and new resonances. Similar outcomes are shown in Section 5 for the MCHM at high scale that will be only reachable with the future high energy hadron colliders. Section 6 describes the EFT perspectives, stressing for instance the correlation between some

selected EFT parameters in the MCHM₅ and the MCHM₁₄ both at low and high scales.

Section 7 concludes by stressing how this detailed phenomenological analysis of these two MCHM scenarios, serves as an useful showcase for the exploration of the BSM world by experiments, with well-defined but still broad scope guidelines. It highlights in this way, what can be already achieved at the presently running LHC and the forthcoming HL-LHC era. It emphasizes the unique importance of a future high energy hadron collider to explore in details the Top-Higgs sector.

2 The Higgs as a Pseudo-Nambu Goldstone Boson

We will present only the features of composite Higgs scenarios that are directly relevant to our study. In particular, we will not describe the spin-1 sector, which is fixed by the pattern of symmetry breaking, in our case $SO(5) \rightarrow SO(4)$. We refer the reader to the complete review [14] where the general construction and results for the MCHM bosonic sector are presented. For our purposes, it is sufficient to know that the breaking of the electroweak (EW) symmetry can be parametrized in unitary gauge through the orthogonal matrix

$$U = \begin{pmatrix} \mathbb{1}_{3 \times 3} & \vec{0} & \vec{0} \\ \vec{0}^T & \cos \frac{h_0+h}{f} & \sin \frac{h_0+h}{f} \\ \vec{0}^T & -\sin \frac{h_0+h}{f} & \cos \frac{h_0+h}{f} \end{pmatrix}, \quad (2.1)$$

where h is the Higgs boson, $h_0 = \langle h \rangle$ is its expectation value, and f is the scale at which the breaking $SO(5) \rightarrow SO(4)$ occurs. In Eq. (2.1), $\mathbb{1}_{3 \times 3}$ is the 3×3 identity matrix and $\vec{0}$ is a 3-dimensional null vector. We also recall that in this model one finds

$$M_W^2 = \frac{1}{4} g^2 f^2 \sin^2 \frac{h_0}{f},$$

which leads to the identification

$$f \sin \frac{h_0}{f} \equiv v = 246 \text{ GeV}. \quad (2.2)$$

We will often use the variable

$$\xi = \frac{v^2}{f^2} = \sin^2 \frac{h_0}{f} \quad (2.3)$$

to express our results. It characterizes the deviations from a SM Higgs due to compositeness. The current bound consistent with Higgs data is $f \gtrsim 800 \text{ GeV}$, or $\xi \lesssim 0.1$, [15–21].

Our main focus is on the fermion sector and its interplay with the Higgs boson. This depends on the composite resonances associated with the top quark. Up to EWSB effects, these resonances fall into representations of the unbroken $SO(4)$. One expects to find that sets of these $SO(4)$ representations build up representations of $SO(5)$ with the non-degeneracy arising from the spontaneous breaking of $SO(5)$ (characterized by the scale f). For concreteness, we will focus on two possibilities:

- Resonances falling into a **5** of $SO(5)$, which split into $SO(4)$ multiplets as $\mathbf{5} = \mathbf{4} + \mathbf{1}$.
- Resonances falling into a **14** of $SO(5)$, which split into $SO(4)$ multiplets as $\mathbf{14} = \mathbf{9} + \mathbf{4} + \mathbf{1}$.

The first case allows for the minimal number of extra fermionic degrees of freedom, while imposing the custodial protection of the $Z\bar{b}_L b_L$ coupling [22], which is important when considering EW precision measurements [23–29]. The second possibility is non-minimal and has been considered in [16, 19, 30–35]. It has been pointed out that it allows for an enhancement of certain Higgs couplings w.r.t. to the SM [19, 32], in contrast to the minimal case (and other possibilities) which always leads to suppressions. One of our goals in this work is to contrast these two scenarios from the point of view of searches for the $t\bar{t}h$ and $t\bar{t}hh$ processes at the 14 TeV High Luminosity phase of the LHC, and the High Energy pp collider projected to run at 100 TeV, and even up to 150 TeV.

We describe the relevant features of the previous fermion embeddings in the following sections.

2.1 The Fermion Sector of the MCHM₅

Considering only the top and its partners, the model is comprised by the “elementary” fields $q_L = (t_L, b_L)$ and t_R together with a set of “composite” fermionic resonances. The elementary fields have the $SU(3)_C \times SU(2)_L \times U(1)_Y$ quantum numbers of the SM left-handed (LH) top-bottom $SU(2)_L$ doublet and of the SM right-handed (RH) top $SU(2)_L$ singlet, respectively. The composite resonances fall into $SO(5)$ representations that split into $SO(4)$ representations due to the spontaneous breaking at the scale f . They contain a number of vector-like $SU(2)_L \times U(1)_Y$ representations, that depend on the fermion embedding. The smallest representation compatible with custodial symmetry is the **5** of $SO(5)$, whose decomposition under $SO(4)$ is given by a fourplet, Ψ_4 , and a singlet, Ψ_1 . We denote the corresponding states by

$$\begin{aligned}\Psi_4 &\sim (X_{5/3}, X_{2/3}, T, B) , \\ \Psi_1 &\sim \tilde{T} ,\end{aligned}\tag{2.4}$$

The subindex denotes the electric charge. While not explicitly indicated, the T and \tilde{T} states have charge 2/3 and B has charge $-1/3$. The states (T, B) transform as a $SU(2)_L$ doublet and have hypercharge $Y = 1/6$, i.e. they have the same SM quantum numbers as the elementary field q_L , while an exotic $SU(2)_L$ doublet with $Y = 7/6$ is composed of the $(X_{5/3}, X_{2/3})$ states. Finally, \tilde{T} has the SM quantum numbers of t_R .

The elementary sector is simply described by

$$\mathcal{L}_{\text{elem}} = \bar{q}_L i \not{D} q_L + \bar{t}_R i \not{D} t_R ,\tag{2.5}$$

where D stands for the $SU(3)_C \times SU(2)_L \times U(1)_Y$ covariant derivative.

We write the composite sector directly in terms of the $SO(4)$ multiplets:

$$\mathcal{L}_{\text{comp}}^{\mathbf{5}} = \bar{\Psi}_4 i (\not{D} - i\ell) \Psi_4 - M_4 \bar{\Psi}_4 \Psi_4 + \bar{\Psi}_1 i \not{D} \Psi_1 - M_1 \bar{\Psi}_1 \Psi_1 .\tag{2.6}$$

Here, the covariant derivative contains only the gluon and hypercharge fields, that is, $D_\mu = \partial_\mu + ig_s G_\mu + i\frac{2}{3}g'B_\mu$. The remaining electroweak interactions are inside the d_μ and e_μ symbols, which are defined in terms of the Maurer-Cartan form

$$iU^{-1}(\partial_\mu + ig_a A_\mu^a T^a)U = d_{\mu,\hat{a}}T^{\hat{a}} + e_{\mu,a}T^a \equiv d_\mu + e_\mu \quad , \quad (2.7)$$

where T^a are the generators of the unbroken $SO(4)$ and $T^{\hat{a}}$ are the broken generators. The gauge fields A_μ^a belong to the algebra of $SO(4) \cong SU(2)_L \times SU(2)_R$, in which the electroweak fields are embedded as follows: the W fields gauge $SU(2)_L$ while B_μ gauges T_R^3 and the remaining generators are ungauged. The hypercharge is then given by $Y = 2/3 + T_R^3$.¹ This covariant derivative allows for the non-linear realization of the full $SO(5)$ symmetry in the kinetic terms, even though the Lagrangian (2.6) exhibits explicitly only the $SO(4)$ symmetry [36, 37]. However, note that the SM covariant derivatives break the $SO(5)$ global symmetry explicitly. In App. A we give the $SO(5)$ generators, including those of the gauged $SU(2)_L \times U(1)_Y$ subgroup. The e_μ symbol term contains corrections to the electroweak interactions of the resonances, due to compositeness. These are detailed in App. C. Apart from the “kinetic” terms, we include separate mass terms for Ψ_4 and Ψ_1 . The difference $M_4 - M_1$ arises from the spontaneous breaking of $SO(5)$, which we do not describe here. For our purposes, M_4 and M_1 can be treated as independent phenomenological parameters.

As mentioned above, some of the fermionic resonances have the same SM quantum numbers as the elementary fields, leading to the possibility of mixing between them. In order to write the elementary-composite mixing terms, it is convenient to embed the elementary states using $SO(5)$ notation as follows

$$Q_L^5 = \frac{1}{\sqrt{2}} \begin{bmatrix} -ib_L \\ -b_L \\ -it_L \\ t_L \\ 0 \end{bmatrix} \quad , \quad T_R^5 = \begin{bmatrix} 0 \\ 0 \\ 0 \\ 0 \\ t_R \end{bmatrix} \quad , \quad (2.8)$$

while Ψ_4 and Ψ_1 are similarly written in 5-plet notation as (see App. B for further details)

$$\Psi_4 = \frac{1}{\sqrt{2}} \begin{bmatrix} -iB + iX_{5/3} \\ -B - X_{5/3} \\ -iT - iX_{2/3} \\ T - X_{2/3} \\ 0 \end{bmatrix} \quad , \quad \Psi_1 = \begin{bmatrix} 0 \\ 0 \\ 0 \\ 0 \\ \tilde{T} \end{bmatrix} \quad . \quad (2.9)$$

In terms of these definitions, the mass mixing Lagrangian takes the form

$$\begin{aligned} \mathcal{L}_{\text{mix}}^5 &= f \bar{Q}_L^5 U [y_{L4}\Psi_4 + y_{L1}\Psi_1] + \text{h.c.} \\ &+ f \bar{T}_R^5 U [y_{R4}\Psi_4 + y_{R1}\Psi_1] + \text{h.c.} \end{aligned} \quad (2.10)$$

¹The factor of 2/3 arises because in order to reproduce the SM fermion hypercharges one needs to introduce an extra $U(1)_X$ factor, under which Ψ_5 has charge $X = 2/3$. For further details, see [14]

thus implementing the idea of *partial compositeness* [38].

Finally, we include in our Lagrangian additional Higgs interactions involving the d_μ symbol, which are allowed by the symmetries at the lowest order of derivatives, and are expected to arise from integrating out heavy resonances not included in our low energy theory (see [14] for further details). These are given by

$$\mathcal{L}_{\text{int}}^5 = -i c_L \bar{\Psi}_4 P_L \not{d} \Psi_1 - i c_R \bar{\Psi}_4 P_R \not{d} \Psi_1 + \text{h.c.}, \quad (2.11)$$

where $P_{L,R} = (1 \mp \gamma_5)/2$ are the left and right projectors and c_L and c_R are couplings, expected to be order one.² These terms contain extra Higgs interactions³, detailed in App. C. We should emphasize, however, that these additional couplings do not affect the top Yukawa at tree level, as long as c_{LR} are taken to be real. This can be seen by noting that the operator in Eq. (2.11) is antisymmetric in Ψ_4, Ψ_1 , such that terms with the same mass eigenstate fermion will cancel out between the operator and its complex conjugate. This holds in fact for similar operators built out of any fermion representation, see [32], which will be relevant for the **14** representation described below.

For this reason, these modifications will only be important in characterizing the extended fermionic sector of the models. We find that the shape of distributions is largely unaffected by these terms, barring the possibility of a tuned cancellation between the vertices of Eq. (2.11) and those of Eq. (2.10), as we will see in section 3.

The complete Lagrangian (in the top sector) is

$$\mathcal{L} = \mathcal{L}_{\text{elem}} + \mathcal{L}_{\text{comp}}^5 + \mathcal{L}_{\text{mix}}^5 + \mathcal{L}_{\text{int}}^5. \quad (2.12)$$

The charge 2/3 mass matrix in the $\{\bar{t}_L, \bar{T}_L, \bar{X}_{2/3,L}, \bar{\tilde{T}}_L\}$ vs $\{t_R, T_R, X_{2/3,R}, \tilde{T}_R\}$ basis is then given by

$$\mathcal{M}_{2/3}^5 = \begin{bmatrix} 0 & \frac{1}{2} y_{L4} f (1 + \sqrt{1 - \xi}) & \frac{1}{2} y_{L4} f (1 - \sqrt{1 - \xi}) & \frac{1}{\sqrt{2}} y_{L1} f \sqrt{\xi} \\ -\frac{1}{\sqrt{2}} y_{R4} f \sqrt{\xi} & -M_4 & 0 & 0 \\ \frac{1}{\sqrt{2}} y_{R4} f \sqrt{\xi} & 0 & -M_4 & 0 \\ y_{R1} f \sqrt{1 - \xi} & 0 & 0 & -M_1 \end{bmatrix}. \quad (2.13)$$

Diagonalization of this matrix leads to the physical fermion eigenstates, which are in general admixtures of the original elementary and composite states. The lightest one is identified with the observed top quark. Our numerical analysis follows from this mass matrix, as described in subsequent sections. The remaining resonances have masses

$$X_{5/3} : \quad M_{X_{5/3}} = M_4, \quad (2.14)$$

$$B : \quad M_B = \sqrt{M_4^2 + y_{L4}^2 f^2}. \quad (2.15)$$

²If the strong sector respects parity, we expect $c_L = c_R$. We will take this as a simplifying assumption in the analysis of the **14** representation below.

³It is possible to trade these derivative Higgs couplings to new Yukawa-like terms by a field redefinition (see for instance, [39]), however, we do not take this approach here.

2.2 The Fermion Sector of the MCHM₁₄

In the second scenario, instead of assuming that the composite states span a **5** of $SO(5)$, we assume that they span a **14** of $SO(5)$. This multiplet decomposes under $SO(4)$ as a fourplet and a singlet, as in Eq. (2.4), plus a nonet $\Psi_{\mathbf{9}}$. We denote the corresponding states by

$$\Psi_{\mathbf{9}} \sim (U_{8/3}, U_{5/3}, U_{2/3}, V_{5/3}, V_{2/3}, V_{-1/3}, F_{2/3}, F_{-1/3}, F_{-4/3}) . \quad (2.16)$$

Under $SU(2)_L$, this nonet breaks into three triplets, U with $Y = 5/3$, V with $Y = 2/3$ and F with $Y = -1/3$.

Adding to Eq. (2.6) the nonet $\Psi_{\mathbf{9}}$, we obtain (the precise structure of $\Psi_{\mathbf{9}}$ is given in App. B):

$$\mathcal{L}_{\text{comp}}^{\mathbf{14}} = \mathcal{L}_{\text{comp}}^{\mathbf{5}} + \text{Tr} \left[\bar{\Psi}_{\mathbf{9}} \left(i \not{D} \Psi_{\mathbf{9}} - i [\not{\epsilon}, \Psi_{\mathbf{9}}] \right) \right] - M_{\mathbf{9}} \text{Tr} \left[\bar{\Psi}_{\mathbf{9}} \Psi_{\mathbf{9}} \right] . \quad (2.17)$$

To write the mixing between the elementary and composite sectors, it is convenient to formally embed all the elementary and composite states into “**14**” representations of $SO(5)$, in analogy to what was done for the **5** case. We denote the elementary embeddings by $Q_L^{\mathbf{14}}$ and $T_R^{\mathbf{14}}$ and continue using the notation $\Psi_{\mathbf{9}}$, $\Psi_{\mathbf{4}}$ and $\Psi_{\mathbf{1}}$ for the composite embeddings. All of these become 5×5 traceless symmetric matrices, whose precise form is given in App. B. The mixing Lagrangian is then written as

$$\begin{aligned} \mathcal{L}_{\text{mix}}^{\mathbf{14}} &= f \text{Tr} \left[U^{\text{T}} \bar{Q}_L^{\mathbf{14}} U (y_{L9} \Psi_{\mathbf{9}} + y_{L4} \Psi_{\mathbf{4}} + y_{L1} \Psi_{\mathbf{1}}) \right] + \text{h.c.} \\ &+ f \text{Tr} \left[U^{\text{T}} \bar{T}_R^{\mathbf{14}} U (y_{R9} \Psi_{\mathbf{9}} + y_{R4} \Psi_{\mathbf{4}} + y_{R1} \Psi_{\mathbf{1}}) \right] + \text{h.c.} \end{aligned} \quad (2.18)$$

We also include extra d_{μ} symbol interactions allowed by the symmetries

$$\mathcal{L}_{\text{int}}^{\mathbf{14}} = -i c_4 \bar{\Psi}_{\mathbf{4}} \not{d} \Psi_{\mathbf{1}} - i c_9 \bar{\Psi}_{\mathbf{9}}^{ij} \not{d}^i \Psi_{\mathbf{4}}^j - i \frac{c_{T9}}{4\pi f} \bar{\Psi}_{\mathbf{9}}^{ij} d_{\mu}^i d^{j\mu} \tilde{T} + \text{h.c.}, \quad (2.19)$$

where c_4 , c_9 and c_{T9} are order one couplings and i, j are $SO(4)$ indices. Here, for simplicity we take the strong sector to be parity symmetric. We also expect the two derivatives term with c_{T9} to be subdominant in most channels, since it is suppressed by an extra power of the cutoff $\Lambda \lesssim 4\pi f$. The explicit form of these vertices as well as those arising from the e_{μ} symbol in the kinetic term are reported in App. C.

The complete Lagrangian (in the top sector) is

$$\mathcal{L} = \mathcal{L}_{\text{elem}} + \mathcal{L}_{\text{comp}}^{\mathbf{14}} + \mathcal{L}_{\text{mix}}^{\mathbf{14}} + \mathcal{L}_{\text{int}}^{\mathbf{14}}, \quad (2.20)$$

which leads to the charge 2/3 mass matrix in the $\{\bar{t}_L, \bar{T}_L, \bar{X}_{2/3,L}, \bar{\tilde{T}}_L, \bar{U}_{2/3,L}, \bar{V}_{2/3,L}, \bar{F}_{2/3,L}\}$

vs $\{t_R, T_R, X_{2/3,R}, \tilde{T}_R, U_{2/3,R}, V_{2/3,R}, F_{2/3,R}\}$ basis:

$$\mathcal{M}_{2/3}^{14} = \begin{bmatrix} 0 & \frac{1}{2}y_{L4}fa_+ & -\frac{1}{2}y_{L4}fa_- & -\frac{\sqrt{5}}{4}y_{L1}fs_{2h} & -\frac{1}{2}y_{L9}fb_- & -\frac{1}{2}y_{L9}fs_{2h} & \frac{1}{4}y_{L9}fb_+ \\ \frac{\sqrt{5}}{4}y_{R4}fs_{2h} & -M_4 & 0 & 0 & 0 & 0 & 0 \\ -\frac{\sqrt{5}}{4}y_{R4}fs_{2h} & 0 & -M_4 & 0 & 0 & 0 & 0 \\ y_{R1}f\left(1 - \frac{5}{4}s_h^2\right) & 0 & 0 & -M_1 & 0 & 0 & 0 \\ \frac{\sqrt{5}}{4}y_{R9}fs_h^2 & 0 & 0 & 0 & -M_9 & 0 & 0 \\ -\frac{\sqrt{5}}{4}y_{R9}fs_h^2 & 0 & 0 & 0 & 0 & -M_9 & 0 \\ \frac{\sqrt{5}}{4}y_{R9}fs_h^2 & 0 & 0 & 0 & 0 & 0 & -M_9 \end{bmatrix}, \quad (2.21)$$

where we defined

$$s_h^2 = \xi, \quad s_{2h} = 2\sqrt{\xi}\sqrt{1-\xi}, \quad a_{\pm} = 1 \pm \sqrt{1-\xi} - 2\xi, \quad b_{\pm} = \sqrt{\xi}\left(1 \pm \sqrt{1-\xi}\right).$$

The charge $-1/3$ mass matrix in the $\{\bar{b}_L, \bar{B}_L, \bar{V}_{-1/3,L}, \bar{F}_{-1/3,L}\}$ vs $\{B_R, V_{-1/3,R}, F_{-1/3,R}\}$ basis takes the form

$$\mathcal{M}_{-1/3}^{14} = \begin{bmatrix} y_{L4}f\sqrt{1-\xi} & -\frac{1}{\sqrt{2}}y_{L9}f\sqrt{\xi} & \frac{1}{\sqrt{2}}y_{L9}f\sqrt{\xi} \\ -M_4 & 0 & 0 \\ 0 & -M_9 & 0 \\ 0 & 0 & -M_9 \end{bmatrix}. \quad (2.22)$$

The remaining states have masses

$$X_{5/3} : \quad M_{X_{5/3}} = M_4, \quad (2.23)$$

$$U_{8/3}, U_{5/3}, V_{5/3}, F_{-4/3} : \quad M_{U_{8/3}} = M_{U_{5/3}} = M_{V_{5/3}} = M_{F_{-4/3}} = M_9. \quad (2.24)$$

As in the 5-plet case, the previous mass matrices form the fundamental input to our phenomenological analysis.

2.3 Partial Compositeness and Higgs Couplings

The above models incorporate the partial compositeness paradigm of [38], via linear mixing of the elementary fields q_L and t_R with composite operators transforming as singlets, 4-plets or nonets of the $SO(4)$ symmetry as described by Eqs. (2.10) and (2.18). In addition to giving rise to the top mass, the same operators are responsible for the top-Higgs Yukawa coupling, which is of central importance to this work.⁴

The mechanism is illustrated diagrammatically in Fig. 1, where H is the Higgs doublet [see Eq. (B.2)]. Each green box represents an insertion of the corresponding operator in Eqs. (2.10) or (2.18), to leading order in H/f . For example, the mixing of the singlet Ψ_1 with T_R can happen at 0-th order in H , while the Ψ_1 - Q_L mixing requires an insertion of the Higgs field, which transforms as a **4** of $SO(4)$: $\mathbf{4}_{Q_L} \otimes \mathbf{4}_H \supset \mathbf{1}$. Similarly, the mixing of the 4-plet Ψ_4 with Q_L can happen at 0-th order in H , but requires an

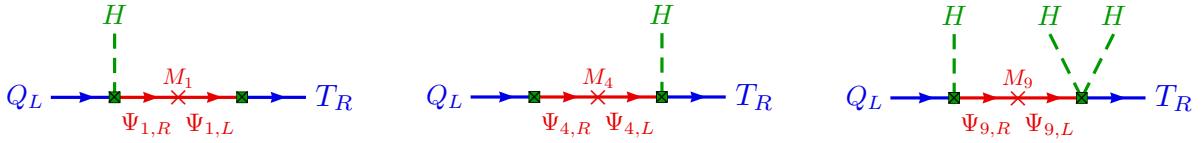


Figure 1. Top-Higgs Yukawa coupling through mixing with singlet, 4-plet and nonet resonances (the mixing is represented by the green squares). The first two cases lead to a SM-like coupling to the Higgs (for $H \ll f$), while the nonet exchange leads to a cubic, non-renormalizable coupling $\bar{q}_L \tilde{H} t_R H^\dagger H$, at leading order in H/f .

H -insertion for the mixing with T_R : $\mathbf{4}_{\Psi_4} \otimes \mathbf{4}_H \supset \mathbf{1}$. Both cases lead to a linear, SM-like coupling $\bar{q}_L \tilde{H} t_R$, plus corrections non-linear in H .

The mixing with a nonet resonance is qualitatively different, requiring one H insertion for the Q_L - Ψ_9 mixing and *two* insertions for the T_R - Ψ_9 mixing: $\mathbf{4}_{Q_L} \otimes \mathbf{4}_H \otimes \mathbf{9}_{\Psi_9} \supset \mathbf{1}$ and $\mathbf{4}_H \otimes \mathbf{4}_H \otimes \mathbf{9}_{\Psi_9} \supset \mathbf{1}$, respectively. As a result, the leading order coupling thus induced is the non-SM like, non-renormalizable operator $\bar{q}_L \tilde{H} t_R H^\dagger H$.

The top mass is obtained by replacing H by its vev, leading to a factor of three in the ratio of the top mass to the top Yukawa (associated to the $\bar{t} t h$ operator) when it is induced by the “cubic” interaction than for the “linear” interaction. The presence of the various channels simultaneously can then lead to an enhancement of the top Yukawa coupling w.r.t. the SM. One should also notice that when $M_1 = M_4$, the linear coupling cancels out,⁵ and the leading order is cubic [19].

Although we will not use it in our numerical analysis, useful approximate expressions for the top mass in the MCHM₅ and in the MCHM₁₄ are given by

$$\begin{aligned}
 m_t^5 &\approx \frac{1}{\sqrt{2}} \sqrt{\xi} \sqrt{1-\xi} \frac{y_L y_R f^2}{\sqrt{|Z_L Z_R|} |M_1|} |1-r_1| \\
 m_t^{14} &\approx \frac{\sqrt{5}}{2} \sqrt{\xi} \sqrt{1-\xi} \frac{y_L y_R f^2}{\sqrt{|Z_L Z_R|} |M_1|} \left| 1-r_1 - \frac{3r_1+5r_9-8r_1 r_9}{4r_9} \xi \right|, \quad (2.25)
 \end{aligned}$$

where we defined the mass ratios $r_1 = M_1/M_4$ and $r_9 = M_9/M_4$ and took $y_{Li} \equiv y_L$ and $y_{Ri} \equiv y_R$ for $i = 1, 4, 9$ (see Section 3.1). The “wavefunction renormalization” factors have the form $Z_{L,R} = 1 + y_{L,R}^2 f^2 / M_{4,1}^2 + \mathcal{O}(\xi)$. The expression (2.25) displays explicitly the behavior described above.

The same effect has an impact on the coupling of the Higgs to two gluons (ggh), normalized to the SM top contribution, which is given by:

$$c_g = \frac{v}{2} \frac{d}{dh_0} \log \det (\mathcal{M}^\dagger \mathcal{M}), \quad (2.26)$$

where \mathcal{M} is the fermion mass matrix, assuming all states are much heavier than the Higgs boson (for our purposes, light state contributions can be neglected).

⁴As said previously, Eqs. (2.11) and (2.19) do not affect the top Yukawa at tree level.

⁵This is the $SO(5)$ symmetric limit of the MCHM₅. See further comments after Eq. (3.2).

For the MCHM₅, using $\mathcal{M} = \mathcal{M}_{2/3}^5$ in Eq. (2.13), this gives

$$c_g^5 = \frac{1 - 2\xi}{\sqrt{1 - \xi}}. \quad (2.27)$$

For the MCHM₁₄, one gets

$$c_g^{14} = c_g^t + c_g^b, \quad (2.28)$$

where

$$c_g^t = \frac{4(1 - r_1)r_9 - (9r_1 + 23r_9 - 32r_1r_9)\xi + 4(3r_1 + 5r_9 - 8r_1r_9)\xi^2}{\sqrt{1 - \xi}[4(1 - r_1)r_9 - (3r_1 + 5r_9 - 8r_1r_9)\xi]}, \quad (2.29)$$

arises from the charge 2/3 sector, $\mathcal{M}_{2/3}^{14}$ in Eq. (2.21), and

$$c_g^b = \xi\sqrt{1 - \xi} \frac{y_L^2 f^2 (1 - r_9^2)}{r_9^2 (M_4^2 + y_L^2 f^2) + y_L^2 f^2 (1 - r_9^2) \xi}, \quad (2.30)$$

arises from the charge $-1/3$ sector, $\mathcal{M}_{-1/3}^{14}$ in Eq. (2.22). For the latter, we explicitly removed the zero-mode (the physical bottom quark) and neglected its contribution to the ggh coupling.

When $M_1, M_4 \gg M_9$ (or $M_1 = M_4$), one finds

$$c_g^t = \frac{3 - 4\xi}{\sqrt{1 - \xi}} \approx 3 - \frac{5}{2}\xi, \quad (2.31)$$

while

$$c_g^b = 1 - \frac{3r_1 + 8r_9 - 11r_1r_9}{2(1 - r_1)r_9} \xi + \mathcal{O}(\xi^2) \quad (2.32)$$

in all other cases, reflecting the underlying cubic versus linear coupling of the top quark to the Higgs field. In all cases, $c_g^b \sim \xi \ll 1$. Global constraints on the gluon fusion process from Higgs measurements, which allow for about 20% deviations from unity in c_g at the 95% C.L. [40], will then also impose constraints on the allowed deviations in the top Yukawa coupling from the SM limit.

2.4 Higgs Decays

While the amplitudes of the processes $t\bar{t}h$ and $t\bar{t}hh$ are determined by the Lagrangians written in the previous sections, it is necessary to specify how the light families of the SM are treated in the context of the composite Higgs models in order to take into account the possible modifications in Higgs decays. Such deviations are expected to be small, since the observed 125 GeV resonance is known to exhibit SM-like properties. The dominant Higgs decay channels are then as in the SM: $h \rightarrow b\bar{b}, W^+W^-, gg, \tau^+\tau^-, c\bar{c}, ZZ$. We neglect the decays into $\gamma\gamma, \gamma Z$ and $\mu^+\mu^-$, which have branching fractions ranging from 0.23%, 0.15% down to 0.01%, as well as even rarer decay channels.

Given the importance of the $b\bar{b}$ channel and the fact that b_L is embedded into $SO(5)$ together with t_L , we must also specify how b_R fits into the models. There are several ways to proceed. Rather than exploring the various possibilities, we choose to supplement the RH bottom with composite resonances that span a $\mathbf{10}$ of $SO(5)$ for both the MCHM₅ and the MCHM₁₄. Such models, called MCHM_{5,5,10} and MCHM_{14,14,10}, were introduced in [16]. For the remaining fermions, we choose to replicate the scheme employed for the third family. We also assume that the lepton sector follows the same scheme as the quark sector. Furthermore, we assume that the mixing angles between the elementary and composite states associated with the light families are small, as in “anarchy” models of flavor (see e.g. [41, 42]).

Under the previous assumptions, it is found that the couplings of the composite Higgs to the vector bosons and to light $f\bar{f}$ pairs are controlled by two model-dependent functions that depend only on ξ . In the MCHM₅ the coupling of the Higgs to a pair of gluons depends also only on ξ , but in the MCHM₁₄ it depends on additional microscopic parameters, as shown in Subsection 2.3.

The partial widths are then simply obtained by rescaling the SM ones. For the MCHM₅, one finds [16]

$$\begin{aligned}
\Gamma(h \rightarrow b\bar{b}) &= F_2(\xi)^2 \Gamma_{\text{SM}}(h \rightarrow b\bar{b}) , \\
\Gamma(h \rightarrow c\bar{c}) &= F_1(\xi)^2 \Gamma_{\text{SM}}(h \rightarrow c\bar{c}) , \\
\Gamma(h \rightarrow \tau^+\tau^-) &= F_2(\xi)^2 \Gamma_{\text{SM}}(h \rightarrow \tau^+\tau^-) , \\
\Gamma(h \rightarrow VV) &= F_2(\xi)^2 \Gamma_{\text{SM}}(h \rightarrow VV) , \\
\Gamma(h \rightarrow gg) &= F_1(\xi)^2 \Gamma_{\text{SM}}(h \rightarrow gg) ,
\end{aligned} \tag{2.33}$$

where

$$F_1(\xi) = \frac{1 - 2\xi}{\sqrt{1 - \xi}} , \quad F_2(\xi) = \sqrt{1 - \xi} . \tag{2.34}$$

For the MCHM₁₄, the bottom channel is controlled by F_1 instead of F_2 , and the ggh coupling is controlled by $c_g^{\mathbf{14}}$ of Eq. (2.28) instead of $F_1(\xi)$.

The total Higgs width in the MCHM models under consideration can then be written as

$$\begin{aligned}
\Gamma_5(h) &= \left\{ F_2(\xi)^2 \left[\text{BR}_{\text{SM}}(b\bar{b}) + \text{BR}_{\text{SM}}(VV) + \text{BR}_{\text{SM}}(\tau^+\tau^-) \right] \right. \\
&\quad \left. + F_1(\xi)^2 \left[\text{BR}_{\text{SM}}(gg) + \text{BR}_{\text{SM}}(c\bar{c}) \right] \right\} \Gamma_{\text{SM}}(h) ,
\end{aligned} \tag{2.35}$$

$$\begin{aligned}
\Gamma_{14}(h) &= \left\{ F_2(\xi)^2 \left[\text{BR}_{\text{SM}}(VV) + \text{BR}_{\text{SM}}(\tau^+\tau^-) \right] \right. \\
&\quad \left. + F_1(\xi)^2 \left[\text{BR}_{\text{SM}}(b\bar{b}) + \text{BR}_{\text{SM}}(c\bar{c}) \right] + (c_g^{\mathbf{14}})^2 \text{BR}_{\text{SM}}(gg) \right\} \Gamma_{\text{SM}}(h) ,
\end{aligned} \tag{2.36}$$

and the branching fractions can also be expressed in terms of the functions F_1 , F_2 , $c_g^{\mathbf{14}}$, and SM quantities. These branching fractions are all that is needed to take into account the effects of compositeness in Higgs decays.

3 Phenomenological Analysis Strategy

3.1 Parameter Space

The top sector of the models described in Sections 2.1 and 2.2 is controlled by the (vector-like) mass parameters, M_i , and by several dimensionless couplings, y_{Li} , y_{Ri} , as well as c_L and c_R for the **5** and c_4 , c_9 and c_{T9} for the **14**. These parameters are a priori complex. However, not all phases are physical. In order to identify the number of physical phases we can proceed as follows. We can start by absorbing the phase of each M_i (thus making it real and positive) by redefining the phases of $\Psi_{i,L}$ or $\Psi_{i,R}$. This leaves one free phase in each such pair, say in $\Psi_{i,R}$, that can be adjusted to absorb the phase of the corresponding y_{Li} (thus making all of the y_{Li} real and positive). Finally, we can absorb the phase of one of the y_{Ri} into T_R^5 or T_R^{14} . We conclude that there are three (five) physical phase(s) in the MCHM₅ (MCHM₁₄). Alternatively, we can choose all the y_{Li} and y_{Ri} to be real and positive, putting the physical phases in M_1 , $c_{L,R}$ for the MCHM₅, and in M_1 , M_4 , c_4 , c_9 , c_{T9} for the MCHM₁₄. In this work, for simplicity, we will assume that all parameters are real, which amounts to imposing CP conservation in the strong sector⁶. This leaves three physical signs in the case of the MCHM₅ and five signs in the MCHM₁₄. We will choose these signs to be $\text{sign}(M_1)$, $\text{sign}(c_L)$ and $\text{sign}(c_R)$ in the first case and $\text{sign}(M_1)$, $\text{sign}(M_4)$, $\text{sign}(c_4)$, $\text{sign}(c_9)$ and $\text{sign}(c_{T9})$ in the second. Finally, in order to simplify our analysis, we will disregard the derivative couplings in eqs. 2.11 and 2.19 until the end of Sec. 3, which leaves us with M_i , y_{Li} and y_{Ri} . The effect of the neglected operators will be considered separately in Sec. 3.8.

While the above parameters respect the $SO(4)$ symmetry, in general they violate the $SO(5)$ symmetry. The $SO(5)$ symmetric limit corresponds to $M_1 = M_4$ and $y_{L1} = y_{L4}$, $y_{R1} = y_{R4}$ for the MCHM₅, and $M_1 = M_4 = M_9$ and $y_{L1} = y_{L4} = y_{L9}$, $y_{R1} = y_{R4} = y_{R9}$ for the MCHM₁₄. It turns out that deviations from the $SO(5)$ symmetric limit in the dimensionless couplings corresponds to a “hard” breaking of the symmetry, in the sense that the Higgs effective potential is finite when the $SO(5)$ symmetry relations are satisfied, but becomes UV sensitive when not⁷. Deviations from the $SO(5)$ symmetric limit in the M_i , on the contrary, correspond to a “soft” breaking, and the Higgs potential remains IR dominated in that case. This motivates us to focus on the case where

$$y_{Li} \equiv y_L, \quad y_{Ri} \equiv y_R, \quad (3.1)$$

for all i , as a way to reduce the number of independent parameters. Small deviations from this limit mean that one can expect additional UV dependent contributions to the Higgs potential. Such contributions can affect the region of parameter space that leads to EWSB and to a Higgs mass $m_h = 125$ GeV. Thus, we take the point of view that imposing that the Higgs mass be reproduced by strictly adhering to the case of a calculable Higgs potential is overly restrictive in the context of our collider study. For this reason we will

⁶It is also worth noting that not imposing CP conservation leads to severe constraints. These (as well as the flavor structure of the models) are beyond the scope of our analysis, and we refer the reader to [43] for an example of a composite Higgs model addressing these issues.

⁷This can be seen from the trace of $\mathcal{M}_{2/3}^\dagger \mathcal{M}_{2/3}$, which becomes independent of the Higgs in this limit, signifying the cancellation of quadratic divergences to the potential.

simply fix the mass of the Higgs, and leave the study of points that reproduce the Higgs mass in the strictly calculable limit to future work.

In conclusion, we are left with the following set of parameters:

- MCHM₅: f , $|M_1|$, $|M_4|$, $\text{sign}(M_1)$, y_L and y_R .
- MCHM₁₄: f , $|M_1|$, $|M_4|$, $|M_9|$, $\text{sign}(M_1)$, $\text{sign}(M_4)$, y_L and y_R .

One of these parameters can be further fixed by requiring that the top mass be reproduced. We choose to fix y_R in this way. Our procedure is to require that

$$\text{Det}(\mathcal{M}_{2/3}\mathcal{M}_{2/3}^T - \bar{m}_t^2\mathbb{1}) = 0 , \quad (3.2)$$

which we solve numerically for y_R for each choice of the parameters other than y_R . When there are no real solutions to this equation, we discard the parameter point. For example, in the $SO(5)$ symmetric limit ($M_1 = M_4$ for the MCHM₅ and $M_1 = M_4 = M_9$ for the MCHM₁₄, and equal couplings as we are assuming), one can easily check that the mass matrices given in Subsections 2.1 and 2.2 have vanishing determinant: the top mass is only induced in the presence of $SO(5) \rightarrow SO(4)$ breaking in the composite sector. Thus, for parameters close to this symmetry enhanced point it can become difficult to accommodate the observed top mass.

For \bar{m}_t in Eq. (3.2), we take $\bar{m}_t = 150$ GeV, the running top mass at the scale of the resonances, which will be typically around 2 – 3 TeV⁸. On the other hand, in the $t\bar{t}h$ and $t\bar{t}hh$ production the relevant scales are of the order of a couple hundred GeV. We therefore distinguish between the high-scale running top mass (relevant for the diagonalization of the mass matrix), and a low scale running top mass, relevant to the physical processes of interest. We take for the latter the pole top mass of $m_t = 173$ GeV, which also enters in kinematical quantities. To first approximation, this takes into account the running between the two scales.

Our strategy to extract the physical quantities is straightforward: given values for the M_i and for y_L , we find y_R from Eq. (3.2). We then diagonalize numerically the fermion mass matrix to obtain the spectrum, and the unitary transformations U_L and U_R such that

$$U_L\mathcal{M}_{2/3}U_R^\dagger = \text{diag}(m_t, M_{T(1)}, M_{T(2)}, \dots) , \quad (3.3)$$

with all the physical masses real and positive. This is done with Mathematica [44]. We also treat the charge $-1/3$ sector in the MCHM₁₄ numerically.⁹ The physical spectrum and the rotation matrices are the main input to the rest of the numerical analysis.

⁸Later, in section 5, we will consider resonances with masses up to tens of TeV, such that strictly speaking, a different running top mass should be picked depending on the energy reached in each parameter space point. However, we find that the effect of the choice of top mass at this scale is negligible and would be masked in comparison with the spread in physical parameters obtained from the numerical scan, so we simply fix $\bar{m}_t = 150$ GeV.

⁹The bottom mass in Eq. (2.22) vanishes. Although one can easily incorporate a finite bottom mass, its effect in the diagonalization is negligible. The correct couplings between the Higgs boson and the bottom quark are taken into account as described in Section 2.4.

For example, we can obtain other quantities of interest, such as the Yukawa matrix in the mass eigenbasis

$$Y_{2/3}^{\text{mass}} = U_L Y_{2/3}^{\text{gauge}} U_R^\dagger, \quad (3.4)$$

where

$$Y_{2/3}^{\text{gauge}} = \frac{d}{dh_0} \mathcal{M}_{2/3} \quad (3.5)$$

is the Yukawa matrix in the gauge eigenbasis. The most relevant quantity will be the $(1, 1)$ entry in $Y_{2/3}^{\text{mass}}$, which corresponds to the top Yukawa coupling. It includes exactly all tree-level effects arising from the Higgs compositeness (the dependence through $\sqrt{\xi} = \sin \frac{h_0}{f}$), as well as the mixing with the vector-like resonances.

The non-linear dependence on h in composite Higgs models leads to interactions between top pairs and a number of Higgs bosons. The $t\bar{t}h$ vertex, whose Feynman rule is given by i times the $(1, 1)$ entry of $\frac{1}{2} d^2 \mathcal{M}_{2/3} / dh_0^2$, after rotating to the mass eigenbasis, also enters in our analysis.

3.2 MCHM Scales, low versus high

The parameter space of MCHM₅ and MCHM₁₄ is explored here in two steps. The first step considers the parameter space relevant for the reach of the LHC machine. This step includes two running operation stages of the LHC, i.e from now until 2023-2024 with about 400 fb^{-1} total integrated luminosity at 13 and 14 TeV, and from 2026 to about 2038, with 10 times more luminosity and 14 TeV CM energy (may be slightly more) with the HL-LHC. The region of the parameter space corresponding to the overall LHC machine operation (from now until the end of the HL-LHC) is labelled as the ‘‘Low Scale MCHM’’, as the dimensionful parameters will take values of a few TeV. This will be the focus for the remainder of this section and section 4.

The second step of this analysis is extended to the ‘‘High Scale MCHM’’. This relates to the future hadron colliders in project, expected to run at CM energies around 100 TeV or even higher [11–13]. For the MCHM high scale regime, the starting hypotheses are either:

1. No new physics is discovered at the HL-LHC, i.e. within the possible reach in mass and/or precision of this collider, or
2. Some evidence (3σ effect) is found such as new high mass resonance(s) or a deviation from the SM for $\mu(t\bar{t}h)$, i.e., the top Yukawa, or
3. A deviation on the $\mu(t\bar{t}h)$ is present at 5σ and $\mu(t\bar{t}hh)$ is observed, but with sizeable uncertainty. Thus a higher energy pp collider would allow higher precision measurements and looking for further effects.

This is the subject of section 5. But it is worth stressing already here, and when looking to the results in section 4, that the points generated in the MCHM low scale parameter

space, are generated both at 14 and at 100 TeV. This is simply because of the reasons listed above.

Here below are specified the ranges considered in each case and the reasoning behind them.

3.2.1 Definition of the ranges for the Low Scale parameters

For the MCHM₅, we consider the following ranges for the parameters:

$$\begin{aligned} |M_1| &\in [0.8, 3.0] \text{ TeV}, & M_4 &\in [1.2, 3.0] \text{ TeV}, \\ f &\in [0.8, 2.0] \text{ TeV}, & y_L &\in [0.5, 3.0]. \end{aligned}$$

For the MCHM₁₄, we use:

$$\begin{aligned} |M_1| &\in [0.8, 3.0] \text{ TeV}, & |M_4| &\in [1.2, 3.0] \text{ TeV}, & M_9 &\in [1.3, 4.0] \text{ TeV}, \\ f &\in [0.8, 2.0] \text{ TeV}, & y_L &\in [0.5, 3.0]. \end{aligned}$$

In order to remain in a perturbative regime, justifying the present tree-level analysis, we will take $y_L < 3$. For the same reason, we also check that y_R , as determined by the top mass, is below 4. The distribution of points within those ranges was not uniform, due to computing constraints, but we strive to cover most of the parameter space.

3.2.2 Definition of the ranges for the High Scale parameters

The range to be covered by the parameters for the High scale case is defined, for each considered MCHM scenario, by the possible reach of a high energy hadron collider order 100 TeV in CM and at least 20 ab^{-1} total luminosity, taking also into account previous studies [45]. Moreover this parameter space range must be linked continuously to the one defined for the Low Scale, which will already be mainly tackled by the HL-LHC; indeed, some showcase scenarios in the Low scale will remain of interest in the High scale as pointed out in the next two sections.

Given the above, for the MCHM₅ we consider:

$$\begin{aligned} |M_1| &\in [2, 30] \text{ TeV}, & M_4 &\in [2, 30] \text{ TeV}, \\ f &\in [0.8, 8.0] \text{ TeV}, & y_L &\in [0.5, 3.0], \end{aligned}$$

and for the MCHM₁₄, we use:

$$\begin{aligned} |M_1| &\in [2, 30] \text{ TeV}, & |M_4| &\in [2, 30] \text{ TeV}, & M_9 &\in [2, 30] \text{ TeV}, \\ f &\in [0.8, 8.0] \text{ TeV}, & y_L &\in [0.5, 3.0]. \end{aligned}$$

3.3 Simple Physical Observables

The diagonalization of the $Q = 2/3$ mass matrix leads to several physical quantities of interest. There is a rich spectrum of vectorlike states. Up to small EW symmetry breaking effects, these vector-like masses are approximately given by:

- MCHM₅:

$$M_4, \quad \sqrt{M_4^2 + y_L^2 f^2}, \quad \sqrt{M_1^2 + y_R^2 f^2},$$

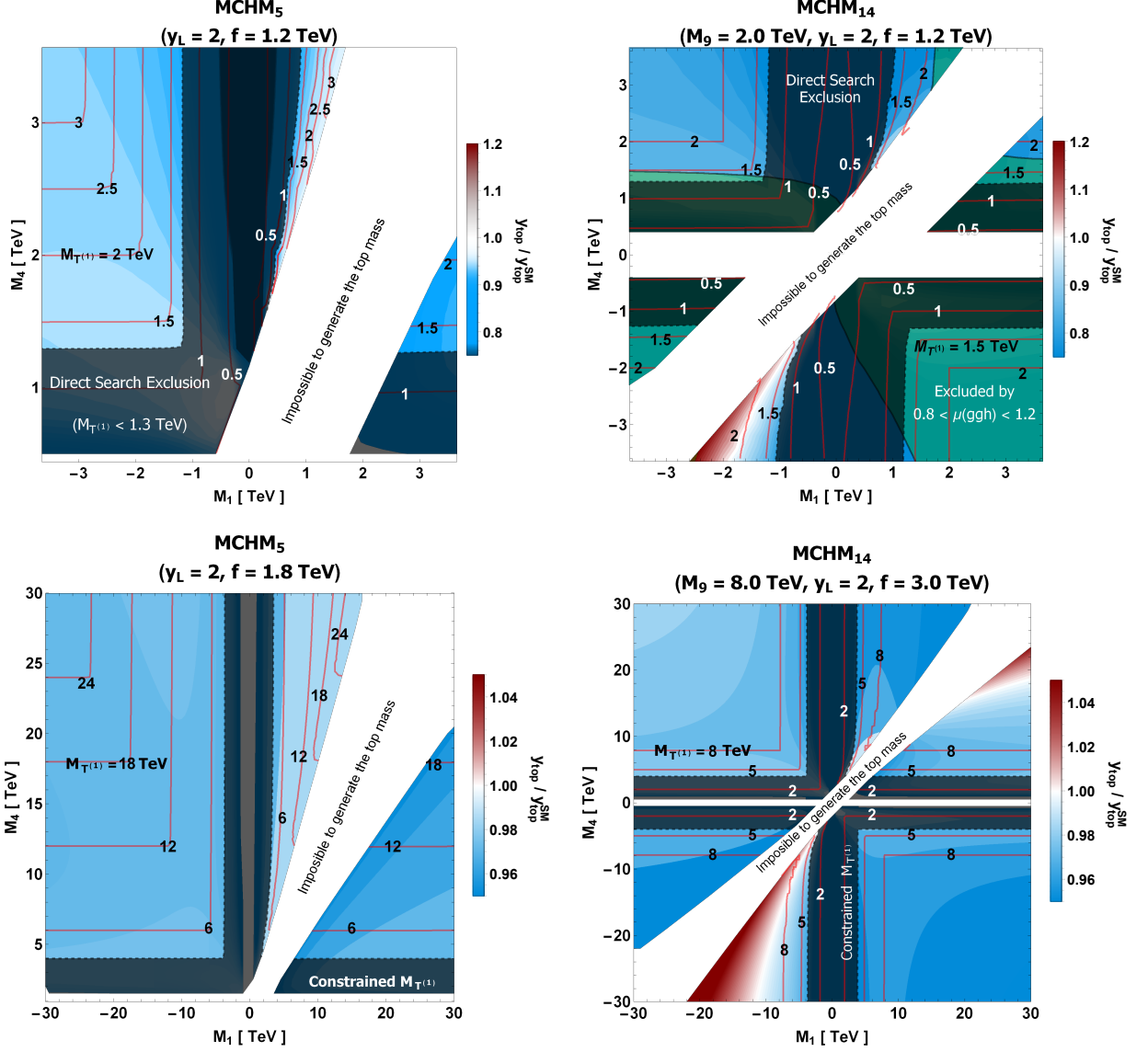


Figure 2. Normalized value of the Yukawa coupling of the top, $y_{\text{top}}/y_{\text{top}}^{\text{SM}}$ in the M_1 - M_4 plane for the MCHM₅ (left) and MCHM₁₄ (right). Top figures focus on $\mathcal{O}(1)$ TeV scale, bottom ones expand it to higher mass scales. Also shown are contours of constant mass of the lightest top partner, $M_{T^{(1)}}$. Overlaid regions indicate constraints: the dark one is given by direct exclusion of top partners in the top plots, and by expected constraints in the HL-LHC in the bottom ones ($M_{T^{(1)}} < 4$ TeV); the green region is constrained by $\mu(\text{ggh})$ measurements. In the white region, the top mass cannot be reached without violating perturbativity.

- MCHM₁₄:

$$M_4, \quad \sqrt{M_4^2 + y_L^2 f^2}, \quad \sqrt{M_1^2 + y_R^2 f^2}, \quad M_9 \quad (\text{degeneracy} = 3).$$

We use the mass of the lightest state, which we call $T^{(1)}$, as a proxy for the scale of the new physics. There are important lower bounds from direct searches for such resonances

by both the ATLAS [9] and CMS [10] collaborations. These searches consider vectorlike top partner resonances decaying exclusively in the bW , tZ and th channels. These bounds depend mildly on the decay branching fractions of the heavy state and are roughly around 1.3 TeV. However in the models under consideration here, one finds sometimes additional decay channels, as we will show in section 4, so these bounds must be taken with care.

We also consider the deviations from the SM of the top quark decay width. However, the previous direct bounds imply that such deviations are well within the experimental uncertainties, and therefore do not impose additional bounds on the models.

As mentioned earlier, a quantity of direct interest in our study is the top Yukawa coupling. Figure 2 displays in the M_1 - M_4 plane the top Yukawa normalized to its SM value, $y_{\text{top}}/y_{\text{top}}^{\text{SM}}$, for MCHM₅ (left) and MCHM₁₄ (right). We consider two different slices in parameter space. For the figures at the top, we take $f = 1200$ GeV, $y_L = 2$ and $M_9 = 2$ TeV, and scan over $M_{1,4} \leq 3.5$ TeV, while for the bottom figures, we fix $y_L = 2$ and $f = 1.8$ TeV for the MCHM₅ and $y_L = 2$, $f = 3$ and $M_9 = 8$ TeV for the MCHM₁₄, and scan over the larger range $M_{1,4} \leq 30$ TeV. The more restricted scan is relevant for the low energy survey as defined in Sec. 3.2.1, while the zoomed out scan refers to the high energy parameter ranges defined in Sec. 3.2.2. While in the MCHM₅ the top Yukawa is approximately determined by the $F_1(\xi)$ in Eq. (2.34), and is always suppressed compared to the SM, in the MCHM₁₄ it displays richer behavior, with the possibility of an enhancement in certain parameter space regions, as emphasized by [19]. Specifically, for the smaller range, only Region III allows an enhancement, while, for the larger scan range, the top Yukawa can also be enhanced in Region I. We also show red contours of constant mass of the lightest top partner resonance $M_{T(1)}$. In the dark overlaid regions, the lightest top partner is approximately excluded by direct searches, assuming it decays only in the bW , tZ and th channels [9, 10], while the green overlay shows the region in which $\mu(ggh)$ differs from unity by 20% or more, which is in tension with current Higgs coupling measurements [40]. In the white area, the top mass cannot be reproduced by values of y_R within our considered perturbative range.

3.4 Strategy to select example points and benchmark points

We select two classes of points to study the physics, in each of the two MCHM scenarios, for both the MCHM at low and at high scale. These are respectively labeled the “example points” and the “benchmark points”.

The selected example points are chosen based on striking features or on how accessible they are in the near future (at the start of the HL-LHC) or towards the end of the HL-LHC or in the much longer term with a 100 TeV pp collider. The striking features are defined with the present results from the LHC experiments on the Top-Higgs sector or the prospect studies achieved for the HL-HE/LHC scenarios or the FCC-hh project. However they do not necessarily represent what is the typical behaviour of the parameter space we explored. They are picked according to our criteria of what is interesting and thus carry a bias. While that is very useful to see what kind of phenomenology can be produced by the model, and give insight on what is happening or could happen in the future, it is not the most comprehensive and extensive way of looking into the possibilities of the models.

On the other side, looking individually on all kinematic distributions for hundreds of points in parameter space is just unfeasible. An interesting compromise can be reached using the approach proposed in [46]: one can use a statistical test to group points of the parameter space into “clusters” based on the similarity between the kinematic distributions of the final or intermediary states produced by them. This is called the “*clustering strategy*”.

Following this strategy, one can then use the same test statistic to choose one point from each cluster as a typical representative of that behaviour, a benchmark point. Analysis designed to search for those benchmark points will be guaranteed to cover all possible phenomena in the region of parameter space considered. We outline the main steps of this algorithm below and refer the reader to [46] for further details and discussion.

The first task is, given two different points in parameter space and one or more kinematic distributions generated by these points (the p_T of the Higgs or top quark, invariant masses, etc.), to decide how similar the distributions are. We organize each of these sets of distributions in samples S_a , where a identifies the point in parameter space, so that running over the bins of the sample is the same as running over all bins of all distributions included in the analysis. In order to decide on similarity between the samples we will use the following log-likelihood ratio:

$$TS_{ab} = -2 \sum_{i=1}^{N_{bins}} \left[\log(n_{(i,a)}) + \log(n_{(i,b)}) - 2 \log \left(\frac{n_{(i,a)} + n_{(i,b)}}{2} \right) \right], \quad (3.6)$$

where $n_{(i,a)}$ is the number of event counts in the i -th bin of sample S_a , $n_{(i,b)}$ is the same for sample S_b and N_{bins} is the number of bins in the sample. TS_{ab} is zero for identical samples and increasingly more negative for increasingly different distributions, so if $TS_{ab} > TS_{cd}$ it means S_a and S_b are more mutually similar than S_c and S_d are.

Now, starting from a number of samples N_{sample} , we follow the steps below to organize them into clusters:

1. We start with a number of clusters that is equal to the number of samples, thus with $N_{cluster} = N_{sample}$, each cluster containing exactly one sample.
2. We obtain the cluster-to-cluster similarity between two clusters, defined as the minimum TS_{ab} between members of those clusters: $TS^{min} = \min_{ab}(\{TS_{ab}\})$ (a runs over all samples in the first cluster and b does the same for the second cluster).
3. We calculate TS^{min} between all possible pair of clusters, and find the two clusters with the highest TS^{min} . Merge these two clusters into one. The number of clusters $N_{cluster}$ diminishes by one.
4. We repeat step 3 until the desired $N_{cluster}$ is obtained.

For each step in the clustering algorithm we can also choose one special sample within each cluster that is the best representative of its behaviour. We do that by calculating $TS_a^{min} = \min_b(\{TS_{ab}\})$ for each sample S_a in the cluster, where b runs over every element

in the cluster except a . The sample with the highest TS_a^{min} is the benchmark sample and the equivalent point in parameter space will be called a benchmark point.

The appropriate final number of clusters is a compromise between a very fine grained view, with a unwieldy number of very homogeneous clusters (in the limit we go back to $N_{cluster} = N_{sample}$), and the opposite extreme, with just a few clusters that contain a huge number of samples that are very heterogeneous in behaviour (thus with a benchmark sample that will not be a very good representative of the whole group). What can be done is to run this algorithm all the way down to $N_{cluster} = 2$ clusters, keeping record of each step. That way one can examine each of the different realizations and decide on the ideal number. The same can be said about which kinematic distributions to include in the samples used for the clustering: we find the most interesting ones by experimentation.

3.5 Implementation of both MCHM models into the Event Generator

We have implemented both models in FeynRules (v2.3) [47] and produced an associated UFO file for each model, that can be interfaced with MadGraph 5 (v2.6.2) [48]. The numerical input from the diagonalization of the mass matrices is then fed via a custom-written Python script into the param_card.dat for processing within MG5. We simulate the $t\bar{t}h$ and $t\bar{t}hh$ processes in MG5. We have also checked that the deviations from the SM in the top quark properties are negligible, since the new physics is rather heavy.

It is important to stress here that the generation framework we fully developed at the parton and LO level can be connected directly to detector simulations such as DELPHES (fast simulation) or detailed experiment full simulations such as the ones of ATLAS or CMS.

3.6 The $t\bar{t}h$ Process

We start by considering the $t\bar{t}h$ process in the MCHM scenarios. This is related in a very simple way to the same process in the SM. The Feynman diagrams (at tree level) are identical in all the models, involving top/anti-top pair production, with a Higgs boson radiated from the top lines. Radiation of the Higgs boson from initial state $q\bar{q}$ lines can be neglected due to the small Yukawa couplings (and PDF suppressions for the heavier flavors). As a result the amplitude is simply proportional to the top Yukawa coupling. The cross section in the MCHM scenarios can then be simply expressed in terms of the SM cross section as

$$\sigma_{\text{MCHM}}(t\bar{t}h) = \left(\frac{y_t}{y_t^{\text{SM}}} \right)^2 \sigma_{\text{SM}}(t\bar{t}h) . \quad (3.7)$$

All the modifications due to Higgs compositeness, or mixing with vector-like fermions, enter only through the top Yukawa coupling. Therefore, as in other BSM cases, a modification in the total rate w.r.t. the SM is expected, but not in kinematic distributions. Besides as we will see in some example cases this deviation can be very small, and still compatible with MCHM. This means that a high precision (order 1% or less) measurement of $\mu(t\bar{t}h)$ might be required (see sections 4 and 5)

3.7 The $t\bar{t}hh$ Process

Next, we consider the $t\bar{t}hh$ process. The additional radiated Higgs boson allows for a richer dependence on the new physics than in $t\bar{t}h$. There are two qualitatively different contributions:

1. Resonant processes, in which vectorlike charge $2/3$ resonances are produced, and subsequently decay in the th channel. The resonances can appear either in pairs (QCD pair production) or singly (as an intermediate state in a fermion line, involving a flavor-changing Yukawa interaction). The process is, however, largely dominated by QCD pair production.
2. Non-resonant processes, in which only the diagrams without intermediate top partners are included, see Fig. 3.

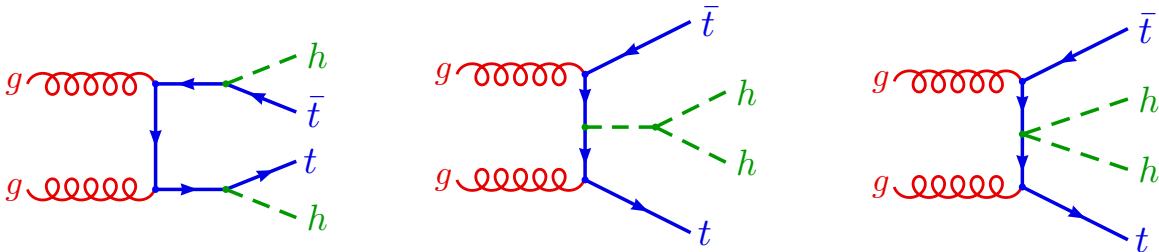


Figure 3. Representative diagrams for the non-resonant $t\bar{t}hh$ process, illustrating the three distinct physical subprocesses: the Yukawa vertex, the Higgs trilinear self-coupling and the “double Higgs” Yukawa vertex arising in composite Higgs scenarios.

The presence of resonant processes can lead to important enhancements in the $t\bar{t}hh$ cross section w.r.t. the SM, depending on their mass. The non-resonant process carries information that is distinct from the resonant part, as discussed below. It is therefore useful to define a “non-resonant cross section” as obtained from this subset of diagrams, which we label as “NR- $t\bar{t}hh$ ”. One can similarly define a resonant cross section in terms of the diagrams involving QCD vector-like pair production. We find that, to an excellent approximation, the total $t\bar{t}hh$ cross section is given by the sum of these two cross sections. The dependence of these two subprocesses with kinematic variables (such as the th invariant mass) is different, so in principle they can be separated experimentally.

We show in Fig. 4 the invariant mass distribution of th for a point in our scan of the MCHM₅, where we display both the resonant and non-resonant contributions to the $t\bar{t}hh$ cross section, as well as the corresponding SM process for comparison. We notice that the NR- $t\bar{t}hh$ follows the SM cross section but displays a suppression and the relative importance of the resonant process w.r.t. the non-resonant one increases with larger CM energies. The cross section for both processes also increases significantly with the CM energy increase from 14 to 100 TeV. Likewise $\mu(t\bar{t}hh)$ increases by a factor of 4 for the same increase in CM energy, while $\mu(\text{NR-}t\bar{t}hh)$ does not change with energy.

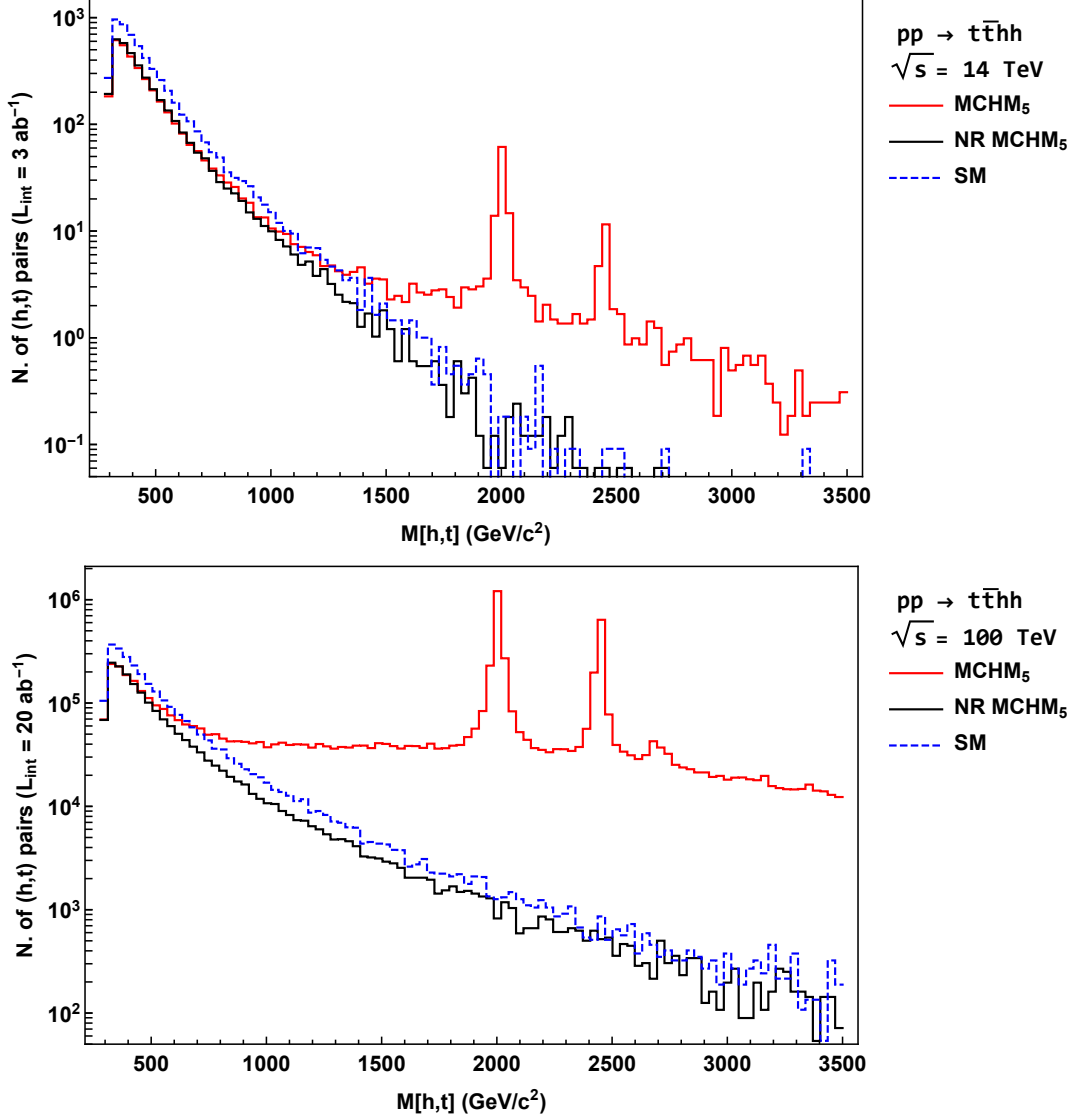


Figure 4. Distribution of the invariant mass of the top quark and a Higgs boson in the MCHM₅ ($M_1 = -2.5$ TeV, $M_4 = 2.0$ TeV, $f = 1.0$ TeV, $y_L = 1.5$). The red continuous line shows the distribution of the full $t\bar{t}hh$ process in the MCHM₅, while the NR- $t\bar{t}hh$ cross section is shown in black. For comparison, we also show in dashed blue the SM $t\bar{t}hh$ distribution. The upper (lower) plot corresponds to 14 TeV (100 TeV) CM energy. Histograms generated with MadAnalysis 5 [49].

3.7.1 The Non-Resonant $t\bar{t}hh$ Process

The p_T distributions for the NR- $t\bar{t}hh$ process show that the typical scales involved are around 100 GeV. As explained before, the top Yukawa coupling should be evaluated at around that scale for the Yukawa vertices appearing in the NR- $t\bar{t}hh$ cross section. For simplicity, we use the top quark pole mass, which also appears in kinematic quantities.

Depending on the vertices they contain, we may divide the diagrams in the MCHM scenarios into three categories, as illustrated in Fig. 3:

1. Diagrams involving only the $t\bar{t}h$ vertex.
2. Diagrams involving both the $t\bar{t}h$ vertex and the trilinear Higgs self-interaction:

$$\lambda = \left[(1 - 2\xi) / \sqrt{1 - \xi} \right] \lambda_{\text{SM}}.$$
3. Diagrams involving the $t\bar{t}hh$ vertex (“double Higgs” Yukawa vertex).

While the first two categories are composed of the same diagrams which appear in the corresponding SM process, the third category is particularly interesting, since the contact $t\bar{t}hh$ vertex has no counterpart in the SM, and is a direct consequence of the non-linear realization of the Higgs sector in composite models [50]. For this reason, it would be extremely interesting if one could get experimental evidence on this coupling.

In order to get a sense for the relative importance of the different physical sub-processes, we have simulated the NR- $t\bar{t}hh$ cross section turning off, in turn, the double Yukawa coupling and the trilinear coupling. Results of this study are shown in subsection 4.2.3.

3.8 Operators Analysis

We move on to studying the effects of the high dimension operators in eqs. 2.11 (controlled by the couplings c_L and c_R) and 2.19 (controlled by c_4 , c_9 and c_{T9}) on the two processes under consideration.

3.8.1 Effect on the $t\bar{t}h$ Process

As mentioned in section 2.1 the derivative operators of eqs. 2.11 and 2.19 do not modify the $t\bar{t}h$ vertex at tree level, appearing only in vertexes involving the Higgs and one or more of the new fermionic resonances. Since the leading diagrams in this process do not involve these resonances the changes in their decay widths do not affect it. Therefore, the cross section of the $t\bar{t}h$ process is not modified by the new operators at tree level.

3.8.2 Effect on the $t\bar{t}hh$ Process

The $t\bar{t}hh$ process cross section is affected in two ways. First, the leading diagrams in this process contain resonances as intermediate states. The change in their decay widths will therefore have an effect on the total cross section. The other source of modification arises from the Yukawa type vertex between the Higgs and two different flavour states which enters directly into the main diagrams.

In order to have a better comprehension of the implications of the operators in the $t\bar{t}hh$ total cross section, we took some example points in the parameter space and did a scan in the region of the (c_L, c_R) plane compatible with perturbativity ($c_L, c_R \in [-3, 3]$). In Fig. 5 we show the scan for one of the points. There, we see that there is a modification of the $t\bar{t}hh$ cross section by a factor that lies in the range $[0.3, 2]$. This modification is dominated by the change in the branching ratio of the decay channel $T^{(1)} \rightarrow th$, which is compatible with the fact that in most of the region $T^{(1)}$ is narrow. We can also see that the derivative operators can be tuned to strongly suppress the branching ratio of $T^{(1)}$ into th , setting it to essentially zero in a small region (in red on Fig. 5). It is also worth

noting that the $t\bar{t}hh$ cross section does not go to zero in that tuned region, because even if we suppress the resonant production, there is still the NR- $t\bar{t}hh$ contribution, thus the absence of a red region in the left plot of Fig. 5.

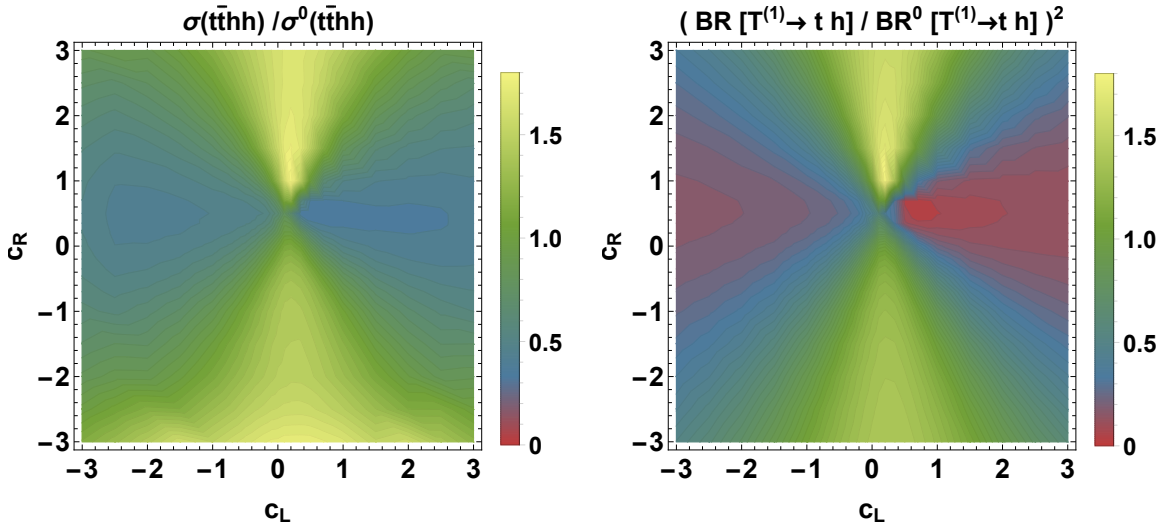


Figure 5. Variation with c_L and c_R of the $t\bar{t}hh$ cross section, normalized to the cross section $\sigma^0(c_R = 0, c_L = 0)$, in the MCHM₅ ($M_1 = -0.96$ TeV, $M_4 = 1.4$ TeV, $f = 1.2$ TeV, $y_L = 0.88$).

Figure 6 shows the p_t distribution of the most energetic Higgs and the top particle keeping the same MCHM₅ parameters used in Fig. 5 for 4 combinations of (c_L, c_R) , as well as the SM distributions for comparison. One notices that the different combinations of (c_L, c_R) produce similar kinematic distributions, except for the one with $(c_L = 0.5, c_R = 0.5)$ which is close to the fine tuned combination which suppresses $T^{(1)} \rightarrow th$. An identical situation is seen in other kinematic distributions and other points of the MCHM₅ parameter space, with the fine tuned combination of (c_L, c_R) that suppresses the width being different for every MCHM₅ point.

The conclusion is that we have two qualitatively different situations:

1. For most values of (c_L, c_R) the shapes of the distributions do not change and there is a change in the total cross section of a factor between 0.5 to 6 for 14 TeV and up to 8 for 100 TeV. This is equivalent to a k-factor and there is no advantage in including two extra parameters to that effect, since we are working at LO and a rescaling of cross sections is needed for comparison with experiment anyway.
2. For a small region around a particular value of (c_L, c_R) , which is different for every point in the MCHM₅ parameter space, the branching ratio $\text{BR}[T^{(1)} \rightarrow th]$ becomes very small (sometimes even zero), and the distributions rapidly change into those of the non-resonant $t\bar{t}hh$ production. It would be interesting to explore what happens to other decay channels near these points, but that is beyond the scope of this paper. We intend to return to this point in a future work focusing on the search for top-partners.

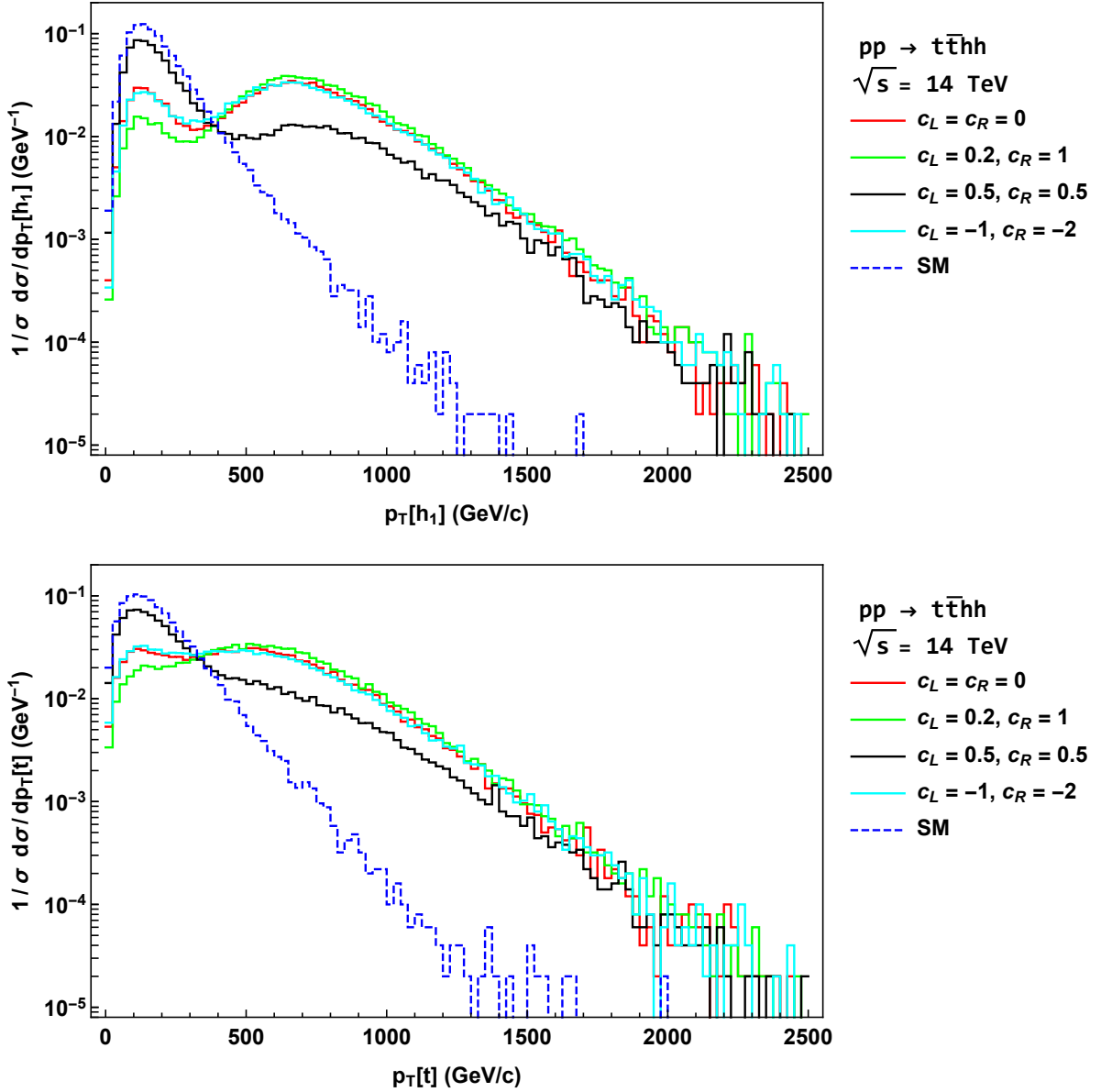


Figure 6. p_t distribution of the most energetic Higgs (h_1) and the top particle for 4 combinations of (c_L, c_R) in the MCHM $_5$ ($M_1 = -0.96$ TeV, $M_4 = 1.4$ TeV, $f = 1.2$ TeV, $y_L = 0.88$). The SM is shown for comparison and all curves are normalized to unity area. Histograms generated with MadAnalysis 5 [49].

For the reasons given above, we will take $c_L = c_R = 0$, and ignore the effects of the derivative operators for the rest of our analysis. We have verified that the situation is qualitatively the same in the MCHM $_{14}$.

4 MCHM at Low Scale

We now proceed to the scan of the parameter space for the MCHM. As mentioned before, we start by looking at the “Low Scale” region, which was characterized in section 3.2.1. We repeat the ranges here for convenience. For the MCHM₅, we scanned over:

$$\begin{aligned} |M_1| &\in [0.8, 3.0] \text{ TeV}, & M_4 &\in [1.2, 3.0] \text{ TeV}, \\ f &\in [0.8, 2.0] \text{ TeV}, & y_L &\in [0.5, 3.0]. \end{aligned}$$

For the MCHM₁₄, we used:

$$\begin{aligned} |M_1| &\in [0.8, 3.0] \text{ TeV}, & |M_4| &\in [1.2, 3.0] \text{ TeV}, & M_9 &\in [1.3, 4.0] \text{ TeV}, \\ f &\in [0.8, 2.0] \text{ TeV}, & y_L &\in [0.5, 3.0]. \end{aligned}$$

The results of the analysis of the scan over the parameters are presented in two ways, namely, the plots of a number of selected observables (Sec. 4.1), completed by the selection of a number of example-points including some of their relevant physics characteristics (Sec. 4.2) and a broader survey of the parameter space and its benchmark points, made in Sec. 4.3.

4.1 Scanning Over Parameter Space

We show in this section a number of selected observables that highlight the behaviour of the MCHM in the scanned regions of the parameter space. For completing the results of this scanning over parameters analysis, these plots include the selected example-points, discussed in details in the next subsection, with their labeling as defined in Tables 1 and 2 (Sec. 4.2). We will conveniently use the $M_1 - M_4$ space displayed in Fig. 2 to define regions in the parameter space for both scenarios under consideration. For the MCHM₅ we will define the following two regions¹⁰:

Region I: $M_1, M_4 > 0$

Region II: $M_1 < 0, M_4 > 0$

and for the MCHM₁₄ we will define the following four regions:

Region I: $M_1, M_4 > 0$

Region II: $M_1 < 0, M_4 > 0$

Region III: $M_1, M_4 < 0$

Region IV: $M_1 > 0, M_4 < 0$

¹⁰We remind the reader that only the sign of M_1 is a free parameter in the MCHM₅, while the signs of both masses are free in the MCHM₁₄. See section 3.1

Each region is populated with about 200 points chosen at random, with points violating our conditions (see Sec. 3.1) being disregarded. Each point in the MCHM₅ is given by a choice of $(f, |M_1|, |M_4|, \text{sign}(M_1), y_L)$ and a point in MCHM₁₄ by a choice of $(f, |M_1|, |M_4|, |M_9|, \text{sign}(M_1), \text{sign}(M_4), y_L)$. Each point is then passed to our implementation of the model in MadGraph, which gives us cross sections and distributions.

As shown in Eq. (3.7), the $t\bar{t}h$ cross section is simply related to the SM one by a rescaling of the top Yukawa coupling. The deviations in the top Yukawa coupling from the SM limit have two distinct origins:

- Deviations due to the compositeness nature of the Higgs boson, which arise from the dependence on the Higgs through trigonometric functions. This depends only on ξ , but is model-dependent and can in principle be used to distinguish the MCHM₅ from the MCHM₁₄.
- Deviations arising from the mixing of the top quark with the new $Q = 2/3$ resonances. This effect depends on all the microscopic parameters of the model in a complicated manner through the diagonalization of the mass matrix. However, due to the fact that the resonances must be much heavier than the top quark, the deviations arising from the mixing are typically subdominant to the ones arising from Higgs compositeness.

One concludes that the $t\bar{t}h$ cross section in the MCHM scenarios is largely controlled by a single parameter, which we can take to be the scale of global symmetry breaking, f . This is illustrated in Fig. 7. The signal strength $\mu(t\bar{t}h)$ of the production cross section is shown for $\sqrt{s} = 14$ TeV but it does not depend on the CM energy at tree level, so the same results apply to $\sqrt{s} = 100$ TeV. The CMS and ATLAS collaborations have presented results on the experimental measurements of $\mu(t\bar{t}h)$. Their reported best fits are: $\mu(t\bar{t}h) = 1.14^{+0.31}_{-0.27}$ for the combined 13 TeV result at an integrated luminosity of 35.9 fb⁻¹ given by CMS [6] and $\mu(t\bar{t}h) = 1.32^{+0.28}_{-0.26}$ for the combined 13 TeV result at an integrated luminosity of up to 79.8 fb⁻¹ given by ATLAS [5]. In Fig. 7 we show the 1 σ and 2 σ limits from CMS (as ATLAS has not reported on their 2 σ limits).

In Fig. 7, one can see that, in Region I of the MCHM₅, the points follow two distinct behaviours. The lower curve has most of its points (blue dots) corresponding to rather low $M_{T(1)}$ masses (below 1.5 or 1.6 TeV) and $\mu(t\bar{t}h)$ below 0.8, thus, in larger tension with the observed value while still within 2 σ of it. Points with higher $M_{T(1)}$ (brown dots) are spread around a second curve with $\mu(t\bar{t}h)$ larger than 0.8 and with $M_{T(1)}$ greater than 2 TeV.

In contrast, in Region II of the MCHM₅, there is only one smooth curve with points with a relatively small dispersion and equally distributed over the whole scanned range in $M_{T(1)}$. The selected example points in the MCHM₅ are indicated in both Regions (P_1 , P_3 and P_4 in Region I and P_2 and P_5 in Region II). The important result is that in the MCHM₅ there is always a deficit in the $t\bar{t}h$ production cross section as compared to the SM. This is, indeed, a main feature of the MCHM₅.

For the MCHM₁₄, three different cases are identified concerning the evolution of this variable versus f and $M_{T(1)}$. Region I has some similarity with the corresponding Region I of the MCHM₅. The main difference is that, in the MCHM₁₄, $\mu(t\bar{t}h)$ can reach much

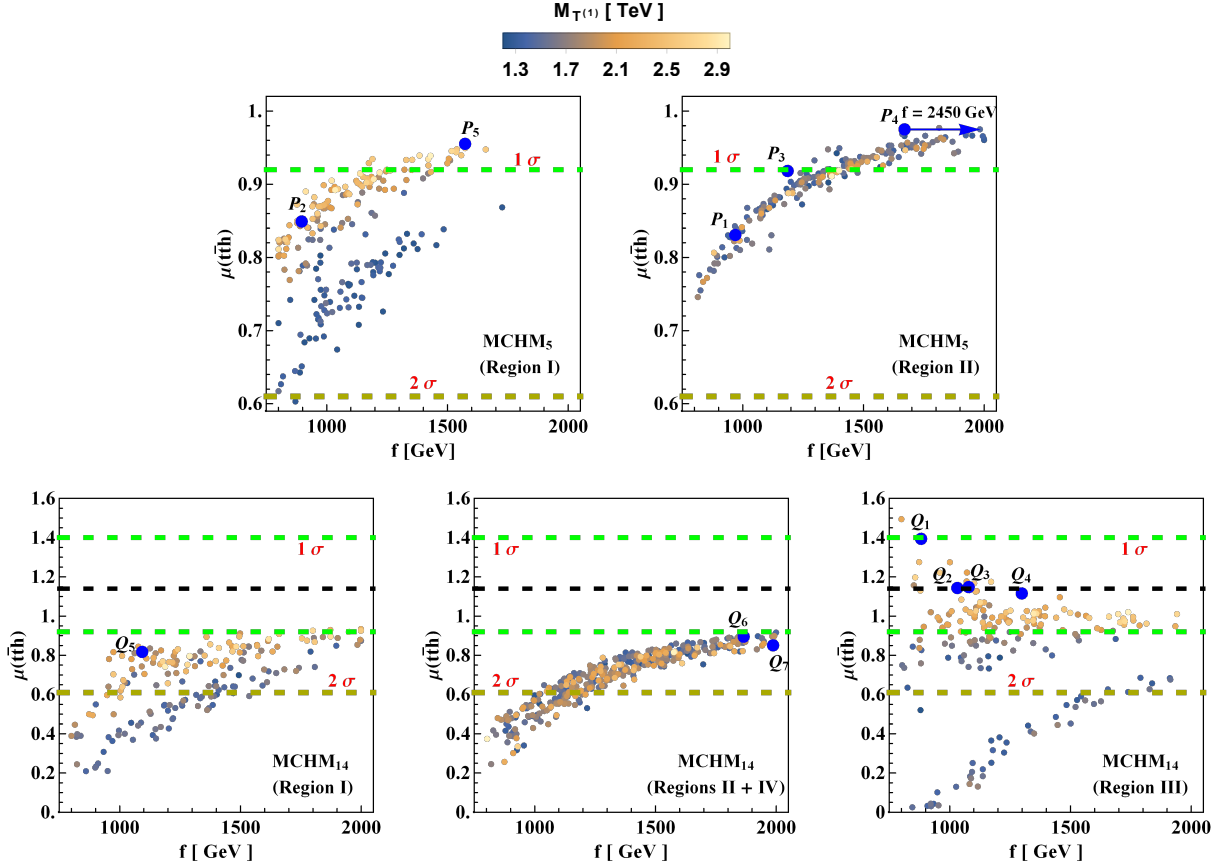


Figure 7. Normalized $t\bar{t}h$ cross section as a function of f for 14 TeV CM energies. We also color code the lightest vector-like mass. The upper left (right) plot corresponds to the Region I (II) of the MCHM_5 . The lower left, central and right plots correspond to the Regions I, II + IV and III of the MCHM_{14} , respectively. The blue arrow in the upper right plot indicates that the example point P_4 is outside the horizontal range of the plot with $f = 2450$ GeV. The green (brown) dashed line shows the 1σ (2σ) limits given by the CMS $\mu(t\bar{t}h)$ measurements while the black dashed line represents the central value [6].

smaller values (down to 0.2 if $M_{T(1)}$ is smaller than ~ 1.6 TeV (blue dots), and down to 0.4 even for higher $M_{T(1)}$ masses). Thus, a fair fraction of all these scanned points have more than 2σ tension with the observed data. This case is represented by the example point Q_5 (see Table 2 in Sec. 4.2).

Regions II and IV of the MCHM_{14} are very similar to each other, and also to Region II of the MCHM_5 , and are thus included in the same plot of Fig. 7. The main difference with the MCHM_5 case lies in a larger dispersion of the points and again the larger range in $\mu(t\bar{t}h)$ they cover (down to 0.2). Two example points, Q_6 and Q_7 , have been selected and they are shown in this Figure (see Table 2 in Sec. 4.2)

The last MCHM_{14} scenario for this observable refers to Region III, which deserves special attention. Fig. 2 shows an increase of $t\bar{t}h$ production cross section as compared to the SM in a fraction of Region III. This is a main feature of the MCHM_{14} as compared to the MCHM_5 or the MCHM_{10} . This feature is clearly visible in Fig. 7, where Region

III of MCHM_{14} is the only one containing points with $\mu(t\bar{t}h) > 1$.

To further explore Region III, a special scan with 100 additional points was performed, extending $M_{T(1)}$ down to 1.3 TeV. All of them are gathered in the lower right plot in Fig. 7. There are two curves. One curve gathers a major part of the low $M_{T(1)}$ cases (blue dots). Some correspond to a dramatic deficit in $t\bar{t}h$ production cross section getting near to zero. Most of the points corresponding to $\mu(t\bar{t}h)$ larger or close to 1 correspond to larger $M_{T(1)}$ masses i.e. masses larger than 1.8 - 2 TeV (brown points). However some rare blue points (lower $M_{T(1)}$ masses) can also correspond to $\mu(t\bar{t}h)$ greater than 1. The highest $\mu(t\bar{t}h)$, above 1, are at relatively small f value, as expected. The selected Q_1, Q_2, Q_3, Q_4 example points correspond to those cases but with a $\mu(t\bar{t}h)$ still within 1σ of the current LHC results.

The observable $\mu(t\bar{t}h)$ is thus a basic and key observable, not only to indicate that there is some BSM effect, but also to reject the MCHM_5 while keeping the MCHM_{14} as still possible, if an enhancement w.r.t the SM is confirmed. If a deficit is instead observed, both MCHM scenarios will be possible, but the distinction between them is tricky and will depend on detailed phenomenology. More details are presented in Subsection 4.2 with the selected example points.

Turning now to the $t\bar{t}hh$ process, we show in Fig. 8 how the signal strength $\mu(t\bar{t}hh)$ depends on the mass of the lightest $Q = 2/3$ resonance, for both MCHM scenarios and for different CM energies. There is a larger dispersion in the points of the MCHM_{14} . However it must be noted that all the points in the four MCHM_{14} regions (about 1000 scanned points) are included in a single plot whereas only 400 (2 regions) are gathered in the MCHM_5 case. These plots show the expected result that for lighter resonances the resonant production can result in a significant enhancement of the total $t\bar{t}hh$ cross section. This effect becomes more prominent for larger CM energies.

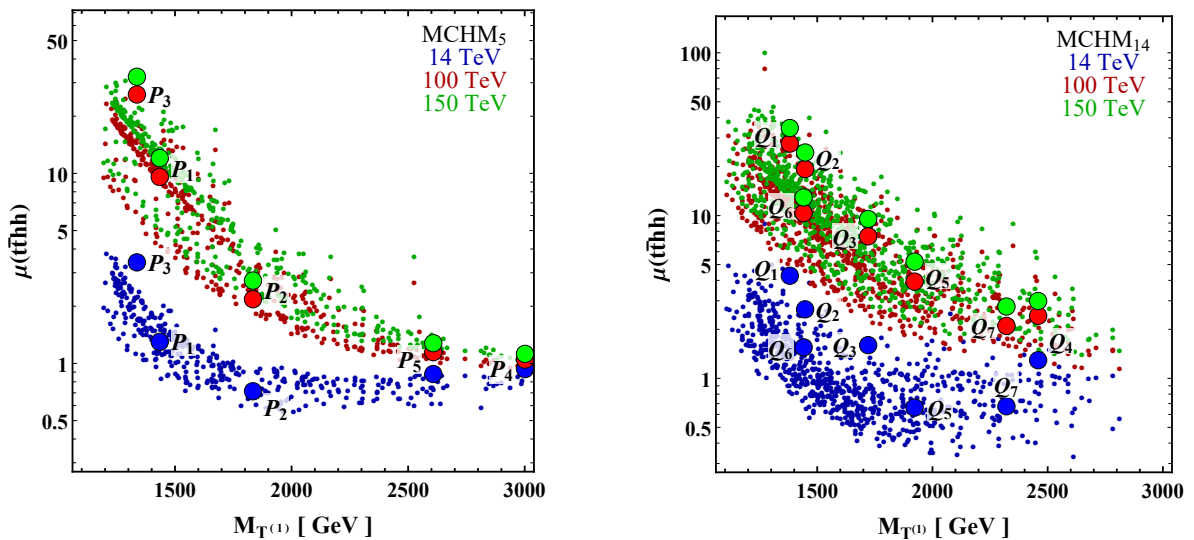


Figure 8. Normalized $t\bar{t}hh$ cross section as a function of the lightest $Q = 2/3$ vector-like mass, for 14, 100 and 150 TeV CM energies. The upper (lower) plots correspond to the MCHM_5 (MCHM_{14}).

These effects are highlighted by the example points. For instance, P_1 and P_3 (in the MCHM₅ case) are showing a large enhancement in $\mu(t\bar{t}hh)$ when increasing the CM energy whereas P_2 , P_4 and P_5 are not showing such an effect.

To complete the results shown in Fig. 8, Fig. 9 presents the ratio between the non-resonant contribution and the total cross section as a function of $M_{T(1)}$ merging the points of all the corresponding regions for each of the MCHM cases. The trends are quite similar between each MCHM scenario with a larger dispersion of the points in the MCHM₁₄ (with again the caveat of 1000 scanned points for MCHM₁₄, versus 400 points for MCHM₅).

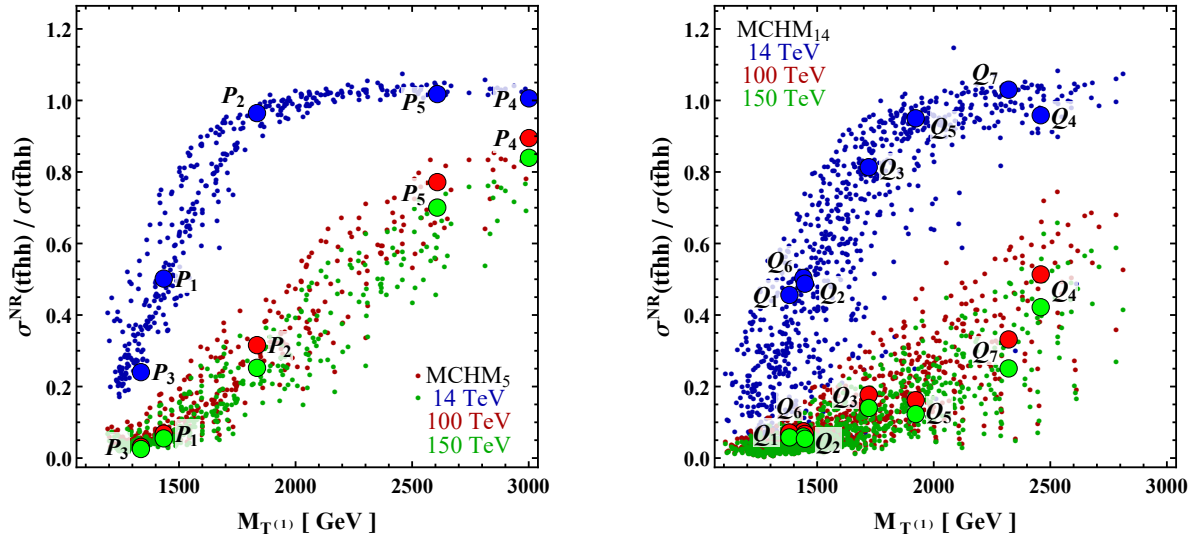


Figure 9. Ratio between the non-resonant $t\bar{t}hh$ cross section and the total $t\bar{t}hh$ cross section as a function of the lightest $Q = 2/3$ vector-like mass, for 14, 100 and 150 TeV CM energies. The left (right) plots correspond to the MCHM₅ (MCHM₁₄).

For heavier masses, the resonant production decreases and the total cross section can be dominated by the non-resonant contribution. Thus one expects deviations from the SM even when the resonances are rather heavy (say 3 TeV).

It is important to stress here that, except for cases with resonances close to the current direct search limit, we see that the non-resonant cross section accounts for a significant fraction of the total cross section. It is therefore of interest to search for deviations from the SM in this quantity, in addition to the dedicated resonant searches.

Finally, we show in Fig. 10 the NR- $t\bar{t}hh$ cross section (normalized to the SM $t\bar{t}hh$ cross section) as a function of the normalized $t\bar{t}h$ cross section. There is a clear correlation, which reflects the fact that both are mainly controlled by the top Yukawa coupling, as explained above. One can note that the dispersion about the general trend is larger for MCHM₁₄ than for MCHM₅.

4.2 Selection of some example points for each MCHM scenario

In order to illustrate the physics of the MCHM scenarios we chose a number of example-points. The selection criteria in the M_1 - M_4 plane (Fig. 2), takes into account the present experimental results including the LHC measurement of the $t\bar{t}h$ production

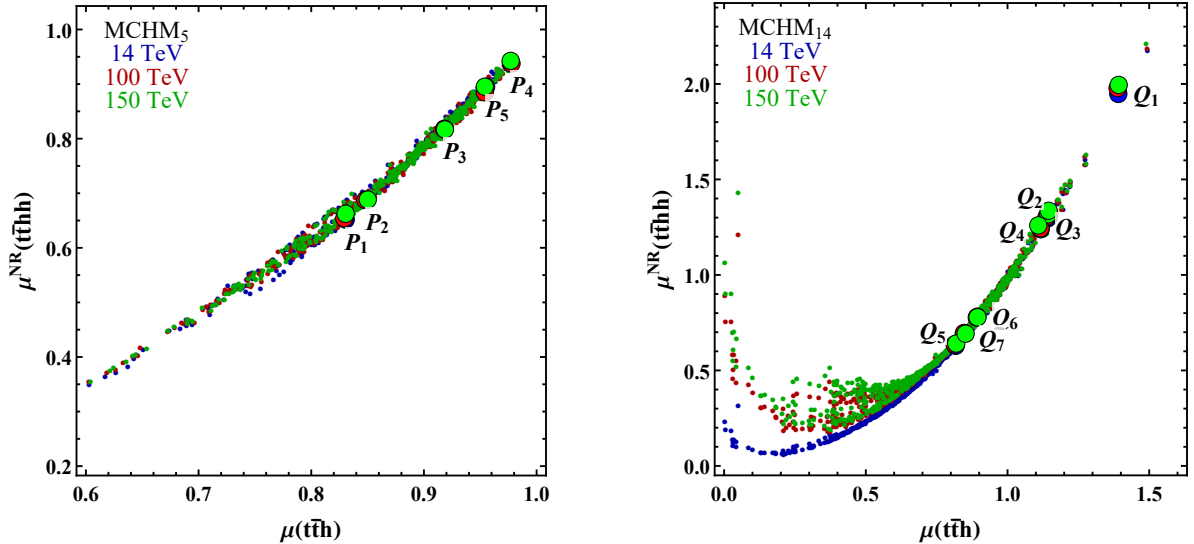


Figure 10. Correlation between the normalized $t\bar{t}h$ and non-resonant $t\bar{t}hh$ cross sections, for 14 and 100 TeV CM energies. The left (right) plots correspond to the MCHM₅ (MCHM₁₄)

process [5, 6], its prospects at the start of the HL-LHC, after the end of Run 3 with 300 fb^{-1} [51], and the exclusion limits on the pair production of heavy vector-like top partners currently obtained by ATLAS and CMS [8–10]. The plots resulting from the parameter scans in section 4.1 add an important input to this selection.

The MCHM parameters characterizing each of the example points and the main observable quantities are summarized in Table 1 and Table 2, where we list the signal strengths for relevant energies, the spectra of vector-like fermionic resonances and the branching ratios of the lightest top partner.

4.2.1 Selected example points and their main features for the MCHM₅

Table 1 lists five selected points belonging either to Region I or Region II of the MCHM₅, with the f scale ranging from about 900 GeV (“strong” compositeness) up to 2.45 TeV (“loose” compositeness) and with different values of y_L . Note that similar scenarios can be found in either region. The chosen points are thus selected independently in one or the other case as reflected in Table 1.

The first point in Table 1 (P_1) shows a non-resonant contribution accounting for almost half the total cross section with a strong compositeness. The deficit in $\mu(t\bar{t}h)$ is relatively large and a bit borderline in regards to the estimated 1σ uncertainty on this measurement by the end of Run 3 (with at least 300 fb^{-1}) [52, 53], and to the rather low masses of the two lightest heavy top partner and the charge 5/3 resonance. This P_1 -scenario will be fully scanned (also including its overall resonances spectrum) at the HL-LHC where a 1σ uncertainty of 4.3% is expected on $\mu(t\bar{t}h)$ [54]. On the contrary, the relatively slight increase of the $t\bar{t}hh$ production cross section with respect to the SM at 14 TeV, might not be reachable even at high luminosity and may even be visible only when the discrepancy with the SM further increases at higher CM energies. This makes this

		P ₁	P ₂	P ₃	P ₄	P ₅
parameters	M ₁ (GeV)	-1317	800	-960	-3550	914
	M ₄ (GeV)	1580	2311	1400	3000	2632
	f(GeV)	969	896	1186	2450	1573
	y _L	1.66	1.80	0.88	1.00	2.36
	y _R	0.62	1.95	0.87	0.85	2.41
$\mu(t\bar{t}h)$ (All Energies)		0.83	0.85	0.92	0.98	0.96
$\mu(t\bar{t}hh)$ (14 TeV)		1.30	0.71	3.40	0.93	0.88
$\mu(t\bar{t}hh)$ (100 TeV)		9.58	2.18	26.01	1.05	1.15
NR- $t\bar{t}hh/t\bar{t}hh$ (14 TeV)		0.50	0.97	0.24	1.01	1.02
NR- $t\bar{t}hh/t\bar{t}hh$ (100 TeV)		0.07	0.32	0.03	0.90	0.77
$M_{T^{(1)}}$ (TeV)		1.44	1.83	1.34	3.00	2.61
$M_{T^{(2)}}$ (TeV)		1.59	2.37	1.45	3.82	3.91
$M_{T^{(3)}}$ (TeV)		2.25	2.83	1.76	3.99	4.56
$M_{B^{(1)}}$ (TeV)		2.25	2.82	1.75	3.87	4.56
$M_{X_{5/3}}$ (TeV)		1.58	2.31	1.40	3.06	2.63
$\Gamma_{T^{(1)}}(\text{GeV})$		24.7	95.2	4.1	26.7	16.5
BR($T^{(1)} \rightarrow th$)		0.33	0.30	0.61	0.31	0.33
BR($T^{(1)} \rightarrow W^+b$)		0.46	0.46	0.06	0	0.16
BR($T^{(1)} \rightarrow tZ$)		0.22	0.20	0.26	0.30	0.26
BR($T^{(1)} \rightarrow W^+W^-t$)		0	0.04	0.07	0.39	0.25

Table 1. Properties of selected example points in the low scale MCHM₅. Red and blue column headings indicate points belonging to Region I and II respectively.

eventual scenario interesting to look at, even if possibly quickly disregarded at a certain stage of the HL-LHC run.

Contrary to point P_1 , point P_2 shows a high NR- $t\bar{t}hh$ and a clear deficit in $\mu(t\bar{t}hh)$; both effects are also visible for points P_4 and P_5 . However, P_2 , as it happens with P_1 , presents a deficit in $\mu(t\bar{t}h)$ because both have a rather low f value (strong compositeness). Points P_4 and P_5 , instead, have a high f value which translates into a $\mu(t\bar{t}hh)$ very close to 1.

Point P_3 has still a rather low f value with, as striking features, the strong increase in $\mu(t\bar{t}hh)$ at the expense of the low NR- $t\bar{t}hh$ contribution (see dominant decay of the lightest resonance into th) and $\mu(t\bar{t}h)$ getting close to 1. All the expected resonances, in this case, have relatively low mass well reachable at the HL-LHC (and even may be before, i.e. by end of the forthcoming Run 3). The HL-LHC increased luminosity will allow to measure the branching decay especially into th , predicted to be dominant with respect to tZ . Besides, the full HL-LHC dataset could indicate a possible excess in $\mu(t\bar{t}hh)$.

Points P_4 and P_5 are rather similar in terms of all the measurable quantities listed in this Table. The NR- $t\bar{t}hh$ contribution is 100% for both cases and will remain dominant even at higher energy accelerators. Moreover, while $\mu(t\bar{t}h)$ stays very close to 1 (due to a high f value, especially for the point P_4), the deficit in $\mu(t\bar{t}hh)$ could already be evidenced with the HL-LHC. Therefore, even if the points P_4 and P_5 look more like scenarios for the higher CM hadron colliders, a first breakthrough on such scenarios, especially for P_5 could be achieved by the end of the HL-LHC. Finally, note that the lightest resonance in both cases has a low branching ratio into Wb (especially P_4), whereas a more important 3-body decay. This enhanced W^+W^-t channel occurs when $T^{(1)}$ comes from the fourplet and is thus almost degenerate with $X_{5/3}$ (both are controlled by M_4) as can be seen in the table. This effect will be specially important at higher energies, as we will discuss in detail in Sec. 5.

It is interesting to note that, as expected in these models (see Subsections 2.2 and 3.3), in all cases, the resonances show a mass degeneracy between two or three of them (MCHM₅) or even more (MCHM₁₄), in many cases due to EWSB. The separation in mass between those states can be of a few tens of GeV down to even a few hundreds of MeV.

The different scenarios described as example points for the MCHM₅, present interesting features that allow distinguishing them from each other. They represent a variety of cases, covering different locations of the MCHM₅ parameter space; thus, they are interesting for exploring this Minimal Composite Higgs Model.

4.2.2 Selected example points and their main features for the MCHM₁₄

The MCHM₁₄ parameter space involves four different cases in the M_1 - M_4 plane (Fig. 2). A special attention is given to the Region III, as it contains the area with $\mu(t\bar{t}h)$ larger than 1. In this region, the M_9 value ranges from 1.3 up to 4 TeV, whereas in the other ones the lowest M_9 value is 2 TeV. The first four points (Q_1 to Q_4) in Table 2 are the selected example points for this region.

		Q ₁	Q ₂	Q ₃	Q ₄	Q ₅	Q ₆	Q ₇
parameters	M ₁ (GeV)	-1173	-1054	-1084	-1579	976	-1387	2998
	M ₄ (GeV)	-1823	-1826	-1767	-2512	1991	1443	-2318
	M ₉ (GeV)	1382	1448	2036	2714	3096	3115	2875
	f(GeV)	882	1032	1078	1298	1093	1865	1987
	y _L	1.98	1.93	2.95	2.71	1.49	1.52	0.94
	y _R	3.90	2.78	2.67	2.46	3.04	0.34	0.54
$\mu(t\bar{t}h)$ (All Energies)		1.40	1.14	1.15	1.11	0.82	0.89	0.85
$\mu(t\bar{t}hh)$ (14 TeV)		4.27	2.66	1.60	1.29	0.66	1.55	0.67
$\mu(t\bar{t}hh)$ (100 TeV)		27.70	19.32	7.46	2.42	3.93	10.36	2.09
NR- $t\bar{t}hh/t\bar{t}hh$ (14 TeV)		0.46	0.49	0.81	0.96	0.95	0.50	1.03
NR- $t\bar{t}hh/t\bar{t}hh$ (100 TeV)		0.07	0.07	0.18	0.51	0.16	0.07	0.33
$M_{T^{(1)}}$ (TeV)		1.38	1.45	1.72	2.46	1.92	1.44	2.32
$M_{T^{(2)}}$ (TeV)		1.38	1.45	2.01	2.70	2.47	1.52	2.82
$M_{T^{(3)}}$ (TeV)		1.41	1.46	2.04	2.71	3.09	2.96	2.87
$M_{B^{(1)}}$ (TeV)		1.38	1.45	2.02	2.70	2.53	2.98	2.84
$M_{X_{5/3}^{(1)}}$ (TeV)		1.38	1.45	1.77	2.51	1.99	1.44	2.32
$\Gamma_{T^{(1)}}(\text{GeV})$		12.2	7.8	55.2	121.1	54.9	9.5	24.2
BR(T ⁽¹⁾ → t \bar{t} h)		0.39	0.28	0.44	0.38	0.50	0.42	0.37
BR(T ⁽¹⁾ → W ⁺ b)		0.35	0.48	0.14	0.13	0.12	0.15	0.02
BR(T ⁽¹⁾ → tZ)		0.16	0.13	0.30	0.27	0.23	0.34	0.35
BR(T ⁽¹⁾ → W ⁺ W ⁻ t)		0.09	0.09	0.12	0.22	0.14	0.08	0.27

Table 2. Properties of selected example points in the low scale MCHM₁₄. Column headings indicate region, with red and orange meaning respectively Regions I and III (with same sign M_1 and M_4) and blue and cyan respectively for regions II and IV (with opposite sign M_1 and M_4).

The selection of the MCHM₁₄ points in the Region III requests, in addition to the criteria listed at the beginning of Subsection 4.2, $\mu(t\bar{t}h)$ to be larger than 1, this is the main difference between the two MCHM scenarios and also an important observable for the exclusion of the MCHM₅. Note that all these points correspond to a relatively low f value, i.e., high compositeness.

The two first points are rather similar; they both correspond to low f and M_9 values. Q_1 is close to the 1σ experimental limits w.r.t the $\mu(t\bar{t}h)$ value. The three

lightest associated resonances are already almost within the limits published by ATLAS and CMS. However, this point is a good example of a high increase in $\mu(t\bar{t}hh)$ (like also observed in some examples of the MCHM₅) and it includes 50% of non-resonant contribution at 14 TeV. If one disregards the resonant contributions, it primarily differs from an equivalent MCHM₅ scenario by the increase in $\mu(t\bar{t}h)$, as compared to the SM.

The model parameters of point Q_2 have values very close to the ones of Q_1 but a slightly higher f value (lower compositeness); it thus translates into a smaller $\mu(t\bar{t}h)$ value. Moreover, $\mu(t\bar{t}hh)$ decreases compared to Q_1 , although it still stays relatively high.

Points Q_3 and Q_4 , have both a relatively low f value but higher M_9 values with about 2 TeV (for Q_3) and 2.7 TeV (for Q_4). Both have $\mu(t\bar{t}h)$ greater than 1 but well within the current experimental limits. Their selection is also based on the request for a high non-resonant contribution.

For completeness, the remaining three regions of the M_1 - M_4 parameter space were considered. In each of them, a representative point is selected as summarized in Table 2: The point Q_5 in Region I, Q_6 in Region II and Q_7 in Region IV.

In the overall covered space these 3 regions provide quite similar cases. Moreover, as shown in Fig. 2, a subregion of Region IV is excluded because of the constraint on the ggh coupling ($0.8 < ggh/SM < 1.2$). The three example points have different f values (around 1 TeV for Q_5 and around 2 TeV for Q_6 and Q_7). They all have a relatively large M_9 (3 TeV). The example points in these three regions show a $\mu(t\bar{t}h)$ value smaller than one and no strong increase in $\mu(t\bar{t}hh)$. The selected points Q_5 and Q_7 have large NR- $t\bar{t}hh$ contributions. Point Q_6 has only 50% NR- $t\bar{t}hh$ contribution. All the NR- $t\bar{t}hh$ relative contributions decrease sharply at higher CM energies, as more phase space becomes available for the production of resonances.

The use of these preliminary observables shows that it will be difficult to disentangle between both MCHM scenarios if a deficit in $\mu(t\bar{t}h)$ is measured. A much more detailed analysis will be required. In some cases, the HL-LHC will perhaps provide a first indication, but a potential discovery will likely need higher energy together with higher luminosity.

4.2.3 NR- $t\bar{t}hh$ contributions in the MCHM₅ and the MCHM₁₄

In order to clarify the different contributions to the non resonant $t\bar{t}hh$ production, we simulated these contributions separately and summarized the results in Tables 3 and 4. The ratios in those tables are obtained by turning off one or more couplings in the model in order to disregard particular classes of diagrams, which are indicated in the table.

The $\sigma_{\mathcal{M}}/\sigma_{\text{NR}}$ ratios show that the effects of the double Higgs Yukawa coupling are typically at the couple to few percent level in the MCHM₅ and the MCHM₁₄ and hardly show any variation with CM energy increase. We also find, by examining the $\sigma_{\text{Yuk}}/\sigma_{\text{NR}}$ ratios, that the effect of the trilinear Higgs self-interaction can be around 15% in both MCHM₅ and MCHM₁₄. For comparison, the effect of the trilinear Higgs self-interaction in the SM $t\bar{t}hh$ cross section is about 20%, with a very mild CM energy dependence. Thus, it is largely the top Yukawa that governs the NR- $t\bar{t}hh$ (just as in the SM), which, to a first approximation, then scales as $(y_t/y_t^{\text{SM}})^4$. This correlation explains the behavior

	P ₁	P ₂	P ₃	P ₄	P ₅	Disregarded diagrams
$\sigma_{\cancel{h}}/\sigma_{\text{NR}}^{t\bar{t}hh}$ (14 TeV)	1.05	1.04	1.03	1.01	1.01	
$\sigma_{\cancel{h}}/\sigma_{\text{NR}}^{t\bar{t}hh}$ (100 TeV)	1.05	1.03	1.03	1.01	1.01	
$\sigma_{\text{Yuk}}/\sigma_{\text{NR}}^{t\bar{t}hh}$ (14 TeV)	0.86	0.85	0.84	0.82	0.82	
$\sigma_{\text{Yuk}}/\sigma_{\text{NR}}^{t\bar{t}hh}$ (100 TeV)	0.87	0.87	0.87	0.85	0.85	
$\sigma_{\text{NR}}^{t\bar{t}hh}/\sigma_{\text{SM}}^{t\bar{t}hh}$ (14 TeV)	0.65	0.69	0.82	0.94	0.90	
$\sigma_{\text{NR}}^{t\bar{t}hh}/\sigma_{\text{SM}}^{t\bar{t}hh}$ (100 TeV)	0.65	0.69	0.82	0.93	0.89	
$(y_t/y_t^{\text{SM}})^4$	0.69	0.72	0.85	0.95	0.91	

Table 3. Study of NR- $t\bar{t}hh$ for the MCHM₅ points in Table 1. The cross sections $\sigma_{\cancel{h}}$ and σ_{Yuk} are obtained by disregarding the classes of diagrams on the last column and σ_{NR} is the total NR- $t\bar{t}hh$. The LO SM $t\bar{t}hh$ production is indicated by σ^{SM} and $\sigma_{\text{Yuk}}^{\text{SM}}$ means we disregarded the SM trilinear Higgs coupling. The top Yukawa couplings are indicated by y_t and y_t^{SM} in the MCHM and SM respectively.

	Q ₁	Q ₂	Q ₃	Q ₄	Q ₅	Q ₆	Q ₇
$\sigma_{\cancel{h}}/\sigma_{\text{NR}}^{t\bar{t}hh}$ (14 TeV)	0.95	0.97	0.96	0.98	1.06	1.03	1.05
$\sigma_{\cancel{h}}/\sigma_{\text{NR}}^{t\bar{t}hh}$ (100 TeV)	0.93	0.96	0.95	0.96	1.05	1.03	1.05
$\sigma_{\text{Yuk}}/\sigma_{\text{NR}}^{t\bar{t}hh}$ (14 TeV)	0.81	0.82	0.81	0.81	0.86	0.84	0.85
$\sigma_{\text{Yuk}}/\sigma_{\text{NR}}^{t\bar{t}hh}$ (100 TeV)	0.82	0.83	0.83	0.83	0.87	0.86	0.87
$\sigma_{\text{NR}}^{t\bar{t}hh}/\sigma_{\text{SM}}^{t\bar{t}hh}$ (14 TeV)	1.94	1.29	1.31	1.25	0.63	0.78	0.69
$\sigma_{\text{NR}}^{t\bar{t}hh}/\sigma_{\text{SM}}^{t\bar{t}hh}$ (100 TeV)	1.98	1.30	1.32	1.25	0.64	0.78	0.69
$(y_t/y_t^{\text{SM}})^4$	1.94	1.30	1.31	1.24	0.67	0.80	0.72

Table 4. Study of NR- $t\bar{t}hh$ for the MCHM₁₄ points in Table 2. The cross sections $\sigma_{\cancel{h}}$ and σ_{Yuk} are obtained by disregarding the classes of diagrams shown on Table 3 and σ_{NR} is the total NR- $t\bar{t}hh$. The LO SM $t\bar{t}hh$ production is indicated by σ^{SM} and $\sigma_{\text{Yuk}}^{\text{SM}}$ means we disregarded the SM trilinear Higgs coupling. The top Yukawa couplings are indicated by y_t and y_t^{SM} in the MCHM and SM respectively.

in Fig. 4 and is evident in the last three lines of Tables 3 and 4, where the enhancement or suppression in the cross section directly arises from the change in the top Yukawa.

The low contributions of the trilinear Higgs and the double Higgs Yukawa couplings present challenges. It makes the measurement of these two couplings harder, and both are important to characterize the compositeness of the Higgs (as opposed to the spectra of fermionic resonances) and are even harder to probe on the resonant production. Further-

more the shape of all kinematic distributions of the NR- $t\bar{t}hh$ final states will be almost identical in shape to the SM one, changing only on the magnitude of the integrated cross section. The top Yukawa can be more directly accessed in the $t\bar{t}h$ channel, but it will be necessary to develop combined analyses between the $t\bar{t}h$ and the NR- $t\bar{t}hh$ to isolate the non-resonant contribution and extract information about these couplings.

Let's stress here a key-role of $t\bar{t}hh$ production process in the study of the self Higgs coupling and the important interplay between the measurement of the κ_λ , the tri-linear Higgs coupling normalized to the SM value, through the hh process (both gluon fusion and Vector Boson Fusion) and of the $t\bar{t}hh$ process. Even if the trilinear Higgs contribution to the $t\bar{t}hh$ process represents only about 15% (slightly lower than in the SM case) of the total cross-section in the MCHM considered scenarios, it is not as difficult to access as the double Higgs Yukawa contribution at the percent level, and indeed it is worth it. The measurement of the κ_λ parameter of the Higgs sector via several processes is becoming of increasing importance as it remains the experimentally least constrained Higgs parameter. This is due to the fact that the “traditional” way to access it at LHC, via the hh production, is currently challenging, because of the still relatively low cross-sections and signature efficiency. In the years to come and over the whole HL-LHC era this will be indeed an essential experimental goal. In order to increase the experimental sensitivity reach, ATLAS and CMS experiments are already now searching, in addition to the hh production through the gluon fusion process [55, 56], for the production process through the Vector Boson Fusion, VBF(hh) [57] and [58]. Recently the need to look for the complementary contribution of $t\bar{t}hh$ on this specific topic is outlined both in view of the HL-LHC and even more of the FCC-hh at 100 TeV [59, 60]. It is worth noting that the SM cross-section of the VBF(hh) and of $t\bar{t}hh$ processes are of the same order, i.e. at the fb level at 14 TeV. Besides, while both ATLAS and CMS are conducting searches for the VBF (hh), a search for the $t\bar{t}hh$ production has been carried on, for the first time, at CMS [7], stressing the growing interest on the experimental side.

To conclude, from the phenomenological viewpoint the $t\bar{t}hh$ channel does not include destructive interference among diagrams unlike in the hh case (see e.g. [61]), and if $\lambda > \lambda_{SM}$, it provides the leading channel where to observe an excess over the SM expectation. From the experimental viewpoint, the two tops in addition to the Higgs pair strengthen the signal efficiency with respect to the hh and $hhjj$ signatures, making it accessible already now at LHC and furthermore at HL-LHC. Besides, the large increase with energy of its cross-section in the SM and even more in the MCHM case makes it an essential channel to study at FCC-hh for high precision and BSM measurements of the Higgs sector.

As a final remark, we wish to point out that the reader should be careful when looking for the separation between the resonant and the non-resonant production in Fig. 4. The separation looks clear for $\sqrt{s} = 14$ TeV and difficult for $\sqrt{s} = 100$ TeV, giving the wrong impression that there is little hope for exploring the NR- $t\bar{t}hh$ at future accelerators. That only happens because the same point in parameter space was used for both plots, and that is a point with low lying fermionic resonances which are produced abundantly at higher energies and dominate over everything else. We explored also the hypothetical situation where no resonance was found at the end of the HL-LHC run, forcing us into

regions of the parameter space where the top partners are heavier and the non-resonant production is more pronounced, as we shall see in Section 5.

4.3 Cluster Analysis applied to the MCHM at low scale

In the next two subsections we apply the clustering idea to the MCHM₅ and the MCHM₁₄, using the parton level kinematic distributions of the $t\bar{t}hh$ process to do the cluster analysis described in Section 3.4.

4.3.1 Clustering of the MCHM₅

In the case of the MCHM₅ we start with the points generated by the scan of Sec. 4.1: 400 points divided between Regions I and II. We then apply the following “cuts” to remove points that are already constrained at a 3σ level¹¹

$$0.33 \leq \mu(t\bar{t}h) \leq 2.07, \quad (4.1)$$

$$M_{T(1)} \geq 1.3 \text{ TeV}. \quad (4.2)$$

We also check if the points in the scan are excluded or not by the experimental measurements of the $t\bar{t}Z$ and $t\bar{t}W$ production cross sections. The latest measurement of the $t\bar{t}Z$ production, performed by the CMS collaboration, corresponding to an integrated luminosity of 77.5 fb^{-1} and at 1σ level is $\sigma(t\bar{t}Z) = 0.95 \pm 0.08 \text{ pb}$ [62]. The $t\bar{t}Z$ signal strength was calculated dividing the measured cross section by the SM prediction $\sigma^{\text{SM}} = 0.84 \pm 0.10 \text{ pb}$, obtaining $\mu(t\bar{t}Z) = 1.13 \pm 0.16$. The latest measurement of the signal strength of the $t\bar{t}W$ production, performed by the ATLAS collaboration, corresponding to an integrated luminosity of 36.1 fb^{-1} is $\mu(t\bar{t}W) = 1.44 \pm 0.32$ at 1σ level [63]. All the scanned points survived these constraints at 3σ level¹².

That leaves us with 348 points at the start of the clustering algorithm. Each one of these points was implemented in MadGraph 5 and events were generated for the production of $t\bar{t}hh$ at a fixed luminosity of 3000 fb^{-1} . At parton level we have only three different particles present: the top, the anti-top and two Higgs bosons (we focused on the most energetic one). Using MadAnalysis we obtained histograms for the following kinematic distributions:

- invariant mass of the top/Higgs pair: $M[t, h_1]$;
- transverse momenta: $p_T[t]$ and $p_T[h_1]$;
- angular distances in the transverse plane: $\Delta_R[t, h_1]$ and $\Delta_R[t, \bar{t}]$
- angular distance to the beam axis: $\theta[t]$ and $\theta[h_1]$.

¹¹Neither CMS nor ATLAS report the 3σ error directly, so the best we can do here is to assume a Gaussian error and estimate the 3σ threshold simply by multiplying their 1σ intervals by 3, using the ATLAS/CMS combined value when available and the smallest one otherwise.

¹²Once again 3σ is roughly estimated as three times the 1σ intervals.

We then constructed samples from these distributions using single distributions or combinations containing two or three distributions. Since the main contribution to the total $t\bar{t}hh$ cross section is coming from the decays of top partners, all these kinematic variables are strongly correlated and that means that most combinations led to very similar clusters.

Initially one is led to consider only the invariant mass, as this is the one variable that makes the resonant structure evident, but we find that using only $M[t, h_1]$ for the clustering puts too much weight on the exact position of the peaks produced by the resonances, instead of more general behaviours like the two peak structure that shows up in the p_T distribution of the Higgs. The result would be to have many benchmark points in the region with lighter and narrower resonances, and just one or two in the rest of the parameter space. Including at least one of the angular variables brings extra physical information and takes away that emphasis, resulting in benchmark samples that are more evenly spread. There is very little difference in regards to what angular distribution we choose, but the results with $\theta[t]$ resulted in samples being more evenly distributed among clusters.

We also experimented with the number of clusters and found out that with a small number of clusters ($N_{cluster} < 10$) we obtain one highly populated cluster that contains all the samples characterized by heavier ($M_{T(1)} \gtrsim 1.5$ TeV) and broader resonances. This cluster results from the merger of two large clusters when we go from 11 to 10 clusters, but these two are already generated early on the clustering process, which means that stopping with $N_{cluster}$ much bigger than 11 only changes the low population clusters, that are already very homogeneous, so there is not much gain in increasing $N_{cluster}$.

We finally decided to stick with $N_{cluster} = 11$ and on using $M[t, h_1]$ and $\theta[t]$ for the cluster analysis of the MCHM₅, the resulting clusters are shown on Figs. 11 and 12, where we also included $p_T[h_1]$ distributions to show their typical behaviour. We first note that most of the clusters are very homogeneous in distributions, in the sense that all curves in each plot are very similar. The benchmark points (black lines in the plots) will then be very good representatives of the behaviour of each cluster. This is true even for the $p_T[h_1]$ distributions, which were not used as a criteria for clustering, and also for all the distributions we have checked (listed above). The only striking exception is cluster 3 (in Fig. 11), which contains all samples with heavy fermionic resonances, with $M_{T(1)} \gtrsim 1.65$ TeV, or no resonances at all decaying to $t\bar{t}hh$. That is a consequence of the comparatively low count of events in the resonant region, when compared to the non-resonant part of the distribution, which is very similar to them all. This could probably be fixed by doing a dedicated scan for points in that region and a separate clusterization, producing more clusters and benchmark points. We decided against it because we already covered that region with example points P_2 , P_4 and P_5 of table 1, which were in fact grouped in cluster 3 and are shown as green curves in Fig. 11.

Figures 11 and 12 also allow us to survey the main features of the whole parameter space of the model. In particular one can see that points in Region I (colored in red) got separated from those of Region II (in blue). Region I is concentrated in clusters 3 to 7, while Region II dominates the rest of the clusters. One can also verify that the fermionic resonances produced in Region I are generally wider than resonances in Region

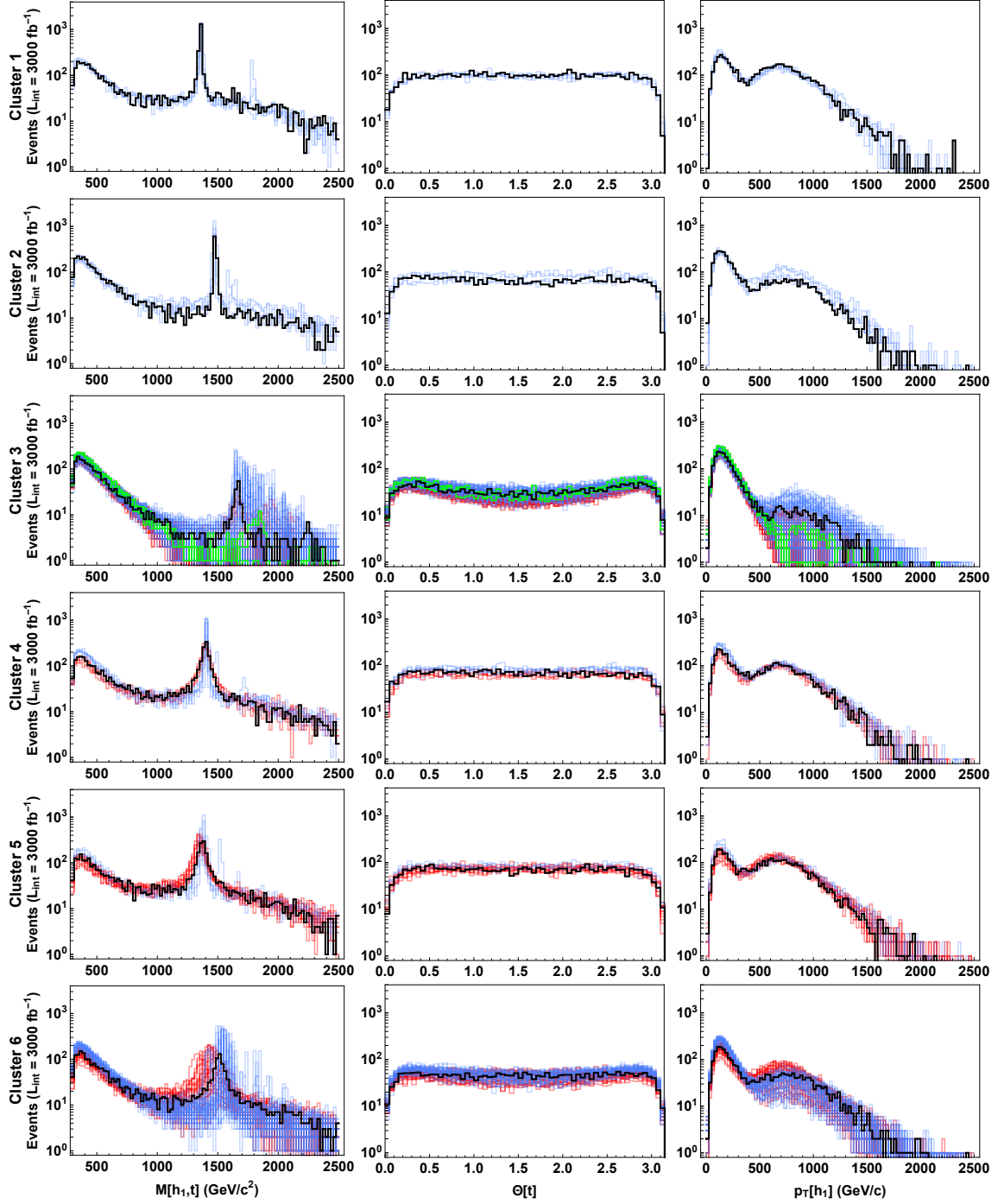


Figure 11. Distributions at $\sqrt{s} = 14$ TeV for the invariant mass of the pair composed by top and most energetic Higgs (first column), angular distribution of the top (second column) and transverse momenta of the most energetic Higgs, organized in clusters by similarity (clusters 1 through 6). Red and blue curves indicate respectively points in Regions I and II of the MCHM₅, the benchmark point for each cluster is shown in black and the example points of table 1 are shown in green (cluster 3 contains P_2 , P_4 and P_5).

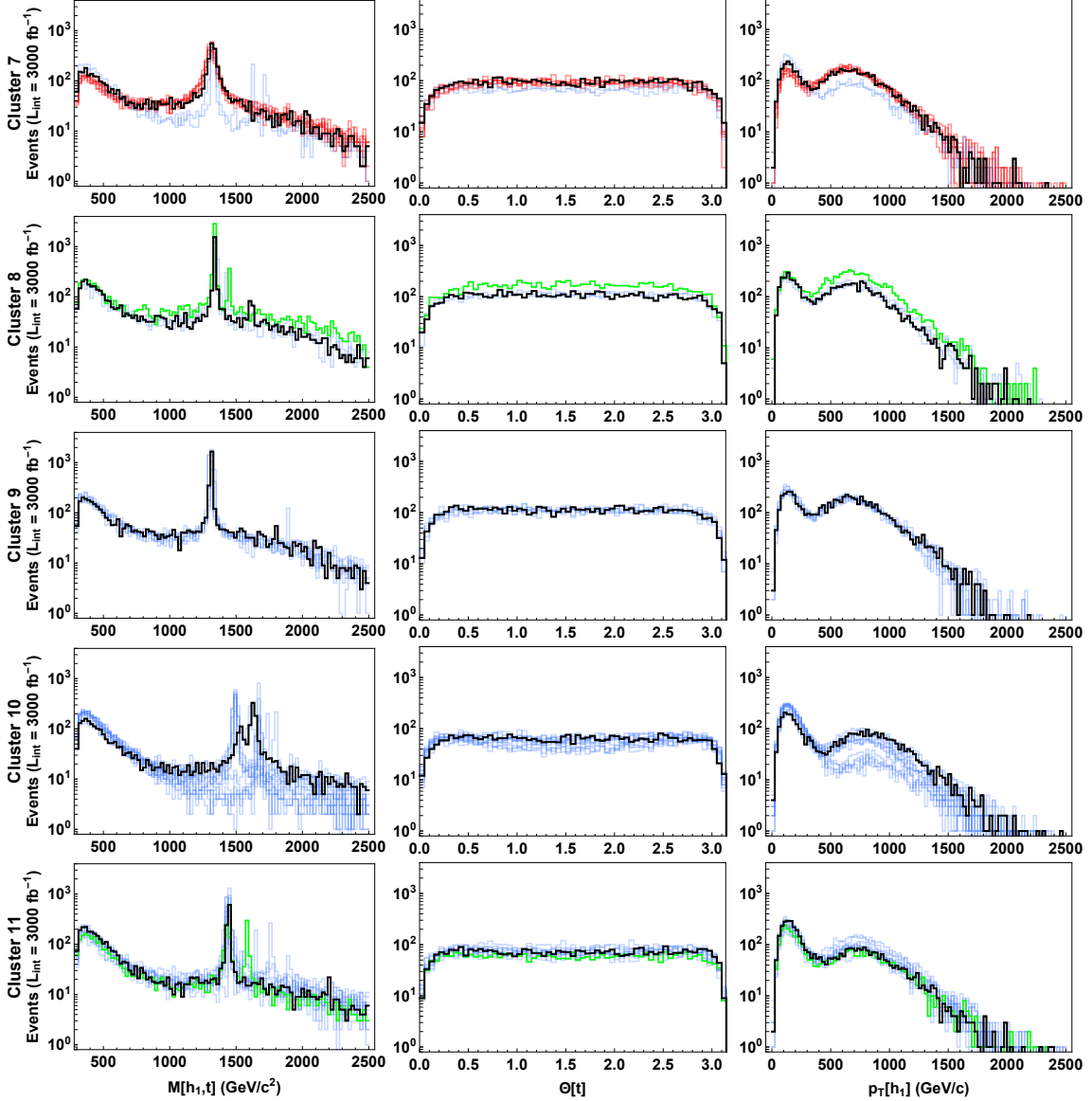


Figure 12. Distributions at $\sqrt{s} = 14$ TeV for the invariant mass of the pair composed by top and most energetic Higgs (first column), angular distribution of the top (second column) and transverse momenta of the most energetic Higgs, organized in clusters by similarity (clusters 7 through 11). Red and blue curves indicate respectively points in Regions I and II of the MCHM₅, the benchmark point for each cluster is shown in black and the example points of Table 1 are shown in green (P_3 is in cluster 8 and P_1 is in cluster 11).

II, this can be more clearly seen in clusters 4, 5 and 7 where resonances from both regions overlap. In order to understand this, it is useful to look at an approximate expression for the top mass, given in Eq. (2.25). This mass is generated in the MCHM₅ by mixing of the elementary fermion fields with the fourplet and singlet resonances. Looking at the first two diagrams in Fig. 1, as well as the Lagrangian of Eq. (2.10), we see this mixing leads to an insertion of y_L times y_R , times a mass insertion of M_1 or M_4 for chirality.

These diagrams must interfere destructively, since the pNGB Higgs vacuum misalignment is generated by $SO(5)$ breaking and hence must vanish in the $SO(5)$ symmetric $M_4 = M_1$ limit. This leads to a dependence $m_t \sim y_L y_R |M_4 - M_1|$, as shown explicitly in Eq. (2.25). In Region I, there is a cancellation between same sign M_1 and M_4 , such that larger values of $y_{L,R}$ are typically needed to generate the top mass¹³. This enhanced mixing also leads, upon mass diagonalization, to a greater value for the $t T^{(1)} h$ vertex, and hence, to wider resonances.

Another interesting general feature is the presence in many cases of more than one peak in the $M[h_1, t]$ distribution. While cluster 9 represents well the usual simplifying assumption used in top partner searches, namely the presence of only one resonance decaying to the th , tZ or bW channels, many of the other clusters contain a sizeable presence of more complicated peak structures, coming specially from Region II. Cluster 10 is the perfect example of this, as its benchmark point has a double peak structure with the second resonance giving a stronger contribution than the lightest one. Most exclusion limits for top partners are obtained through analyses optimized for the situation in cluster 9, and it would be interesting to see how those limits change if more resonances are considered, specially if they overlap significantly.

In Fig. 13 we show how the benchmark points are placed in the parameter space, together with the example points of Table 1 and the rest of the points in the scan not excluded by constraints. We can see that the benchmark points, complemented by the example ones, are well distributed in the parameter space. We finally list the benchmark points and their main features in Table 5, where we can verify many of the features visible in the distribution plots of Figs. 11 and 12. Points in Region I (C_4 , C_5 , C_6 and C_7) have on average higher couplings y_L and y_R and wider $T^{(1)}$ than those in Region II, although the extreme cases in each region can be similar. The point C_7 , which contains a narrow $T^{(1)}$ for Region I standards, is quite similar to C_{10} , in which $T^{(1)}$ is exceptionally wide for Region II.

Another striking feature of Table 5 is that for all of the benchmark points (but C_3) there is at least a 10% branching ratio in 3-body decays. Similarly striking and linked to the previous observation, we note that for all points but this same C_3 point, the 2-body decay into bW is very small, namely between 0% and 2.4%. That is relevant as most top partner searches were done under the assumption that the three 2-body channels (th , tZ and bW) comprise the full width. We will explore the phenomenology of these non-standard branching ratios in a future work.

4.3.2 Clustering of the $MCHM_{14}$

We applied the same clustering method to the $MCHM_{14}$, using again Eqs. 4.1 and 4.2 as constraints. The ideal clustering, following the criteria of homogeneity within clusters while keeping the number of clusters small, was obtained including $M[t, h_1]$, $p_T[t]$ and $\Delta R[h_1, t]$ in the samples and stopping at 12 clusters. The distribution of the benchmark points can be seen in Figure 14 and their main properties are listed in Table 6. We omit the plots of all distributions and clusters as the general features are very similar to

¹³This is also responsible for the white region in Fig. 2, where the top mass cannot be reached without breaking our perturbativity bound on $y_{L,R}$.

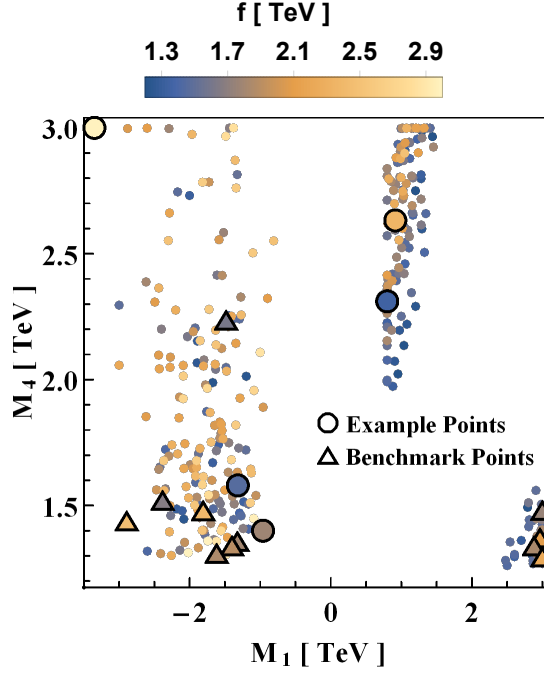


Figure 13. Low scale scan of the MCHM₅ parameter space, including example points of Table 1, benchmark points of Table 5 and the points consistent with constraints in Eqs. 4.1 and 4.2.

		C ₁	C ₂	C ₃	C ₄	C ₅	C ₆	C ₇	C ₈	C ₉	C ₁₀	C ₁₁
parameters	M ₁ (GeV)	-1323	-1809	-1483	2965	2882	2999	3000	-1400	-1618	-2384	-2892
	M ₄ (GeV)	1357	1479	2235	1370	1339	1479	1295	1339	1309	1519	1437
	f(GeV)	1199	1593	1071	1393	1220	1168	1484	1265	1229	1110	1646
	y _L	0.91	2.25	1.38	2.35	1.83	2.33	1.98	1.34	1.22	0.51	1.03
	y _R	0.88	0.58	0.72	3.38	3.57	3.28	3.25	0.66	0.74	2.30	0.85
μ(t \bar{t} h) (All Energies)		0.90	0.94	0.86	0.83	0.78	0.79	0.84	0.91	0.90	0.81	0.94
μ(t \bar{t} hh) (14 TeV)		2.14	1.47	0.80	1.51	1.53	1.02	2.00	2.25	2.41	1.39	1.58
μ(t \bar{t} hh) (100 TeV)		14.58	8.84	3.28	10.28	11.18	7.04	13.42	15.20	16.11	13.68	10.57
NR-t \bar{t} hh/t \bar{t} hh (14 TeV)		0.37	0.59	0.88	0.45	0.40	0.61	0.35	0.36	0.33	0.46	0.55
NR-t \bar{t} hh/t \bar{t} hh (100 TeV)		0.05	0.10	0.22	0.07	0.05	0.09	0.05	0.05	0.05	0.05	0.08
M _{T(1)} (TeV)		1.36	1.48	1.66	1.40	1.38	1.51	1.32	1.34	1.31	1.54	1.44
M _{T(2)} (TeV)		1.63	2.02	2.24	3.55	2.61	3.10	3.22	1.61	1.80	1.63	2.20
M _{T(3)} (TeV)		1.79	3.88	2.68	5.55	5.21	4.85	5.67	2.17	2.02	3.47	3.21
M _{B(1)} (TeV)		1.74	3.87	2.68	3.55	2.60	3.10	3.22	2.16	1.99	1.62	2.22
M _{X_{5/3}} (TeV)		1.36	1.48	2.24	1.37	1.34	1.48	1.29	1.34	1.31	1.52	1.44
Γ _{T(1)} (GeV)		8.83	5.49	26.22	51.92	60.01	71.68	44.33	6.44	7.49	43.78	10.63
BR(T ⁽¹⁾ → th)		0.49	0.45	0.31	0.44	0.43	0.42	0.44	0.47	0.47	0.34	0.45
BR(T ⁽¹⁾ → W ⁺ b)		0.018	0	0.47	0.004	0.004	0.003	0.006	0.024	0.016	0.005	0.010
BR(T ⁽¹⁾ → tZ)		0.39	0.41	0.22	0.42	0.43	0.42	0.43	0.40	0.41	0.50	0.41
BR(T ⁽¹⁾ → W ⁺ W ⁻ t)		0.11	0.13	0	0.13	0.13	0.16	0.12	0.10	0.10	0.14	0.12

Table 5. Benchmark points for the MCHM₅ at low scale and their main features. Red and blue column headings indicate points belonging to Region I and II respectively.

the MCHM₅, with the points without light resonances decaying to $t\bar{t}hh$ being grouped into less homogeneous clusters (specially clusters 4 and 9), but all the plots are available online [64]. There is still a tendency towards narrower resonances when M_1 and M_4 have opposite signs (Regions II and IV), as expected due to the $1-r_1$ term in Eq. 2.25, but now

there is a ξ -proportional correction that is also sensitive to the sign of M_4 (as $M_9 > 0$) and makes this tendency weaker (and hard to notice if one looks only to the benchmark points).

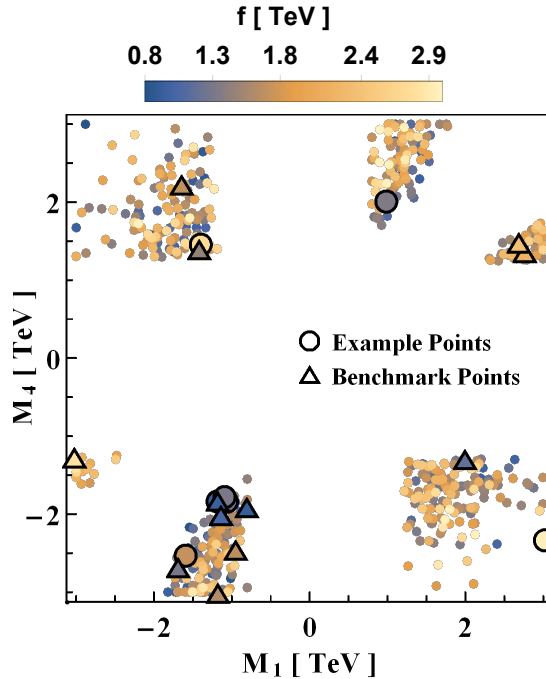


Figure 14. Low scale scan of the $MCHM_{14}$ parameter space, including example points of Table 2, benchmark points of Table 6 and the points consistent with constraints in Eqs. 4.1 and 4.2.

Figure 14 shows that, between the example points of section 4.2.2 and the benchmark points obtained here we are covering the parameter space quite well. One can see that Table 6 contains many points that have a sizeable 3-body decay in all regions and, like in the case of the $MCHM_5$, a fair amount of the scanned points have overlapping resonances (which is the case for the benchmark points of clusters 3, 8 and 11), both of which are relevant concerns for top partner searches and constraints.

We would finally like to stress the presence of the benchmark points D_1 and D_9 , both with a marked increase in $\sigma(t\bar{t}h)$, showing that such a situation is not uncommon in the $MCHM_{14}$ and is a really interesting possibility to evidence this realization of the MCHM.

5 MCHM at High Scale

We continue the analysis of the two studied MCHM scenarios, extending the dimensional parameters to higher scales that can be accessible only in the context of the high CM energy pp colliders in project [11–13, 65–67]. A higher CM energy around 100 TeV is, indeed, requested to confront scenarios with very high mass resonances, with a possible deviation of the $t\bar{t}h$ cross section from the SM value at the percent level (or even less),

		D ₁	D ₂	D ₃	D ₄	D ₅	D ₆	D ₇	D ₈	D ₉	D ₁₀	D ₁₁	D ₁₂
parameters	M ₁ (GeV)	-1173	-943	1979	-1631	2737	-2998	-801	-1130	-1677	2664	-1408	-1169
	M ₄ (GeV)	-1823	-2447	-1297	2196	1340	-1272	-1907	-2005	-2670	1460	1373	-2997
	M ₉ (GeV)	-1382	2000	3889	3236	2836	3473	1500	1467	2000	3230	2965	1329
	f (GeV)	881	1275	1012	1288	1550	1912	863	931	1071	1648	1155	1244
	y _L	1.98	1.33	0.85	2.68	1.67	1.11	1.23	2.93	2.06	2.40	1.04	1.25
	y _R	3.90	1.07	0.73	0.30	1.93	1.86	1.67	1.23	2.65	2.67	0.49	1.32
μ(<i>tth</i>) (All Energies)		1.39	0.90	0.48	0.71	0.68	0.68	0.93	0.98	1.22	0.71	0.68	0.93
μ(<i>tthh</i>) (14 TeV)		4.27	0.97	2.82	0.55	1.34	1.81	2.15	1.57	1.70	0.93	1.83	2.86
μ(<i>t̄thh</i>) (100 TeV)		27.70	6.32	28.44	3.05	10.87	13.69	19.94	11.20	5.21	7.35	16.04	21.53
NR- <i>tthh</i> / <i>tthh</i> (14 TeV)		0.46	0.82	0.08	0.87	0.33	0.25	0.37	0.61	0.87	0.53	0.23	0.30
NR- <i>t̄thh</i> / <i>t̄thh</i> (100 TeV)		0.07	0.13	0.01	0.16	0.04	0.03	0.04	0.09	0.28	0.07	0.03	0.04
M _{T(1)} (TeV)		1.38	1.62	1.31	1.70	1.38	1.31	1.42	1.46	2.00	1.50	1.38	1.33
M _{T(2)} (TeV)		1.38	2.00	1.52	2.20	2.66	2.45	1.50	1.47	2.00	3.16	1.49	1.33
M _{T(3)} (TeV)		1.41	2.00	2.11	3.16	2.84	3.47	1.50	1.47	2.02	3.23	1.81	1.36
M _{B(1)} (TeV)		1.38	2.00	1.54	3.18	2.69	2.45	1.50	1.47	2.00	3.17	1.80	1.33
M _{X_{5/3}(1)} (TeV)		1.38	2.00	1.30	2.20	1.34	1.27	1.50	1.47	2.00	1.46	1.37	1.33
Γ _{T(1)} (GeV)		12.17	91.45	22.06	157.07	67.39	53.12	64.23	79.22	17.70	82.52	17.55	3.63
BR(T ⁽¹⁾ → th)		0.40	0.25	0.44	0.26	0.42	0.42	0.28	0.11	0.26	0.42	0.46	0.17
BR(T ⁽¹⁾ → W ⁺ b)		0.35	0.51	0.05	0.48	0.01	0.01	0.45	0.61	0.36	0.005	0.11	0.43
BR(T ⁽¹⁾ → tZ)		0.16	0.24	0.41	0.22	0.43	0.44	0.24	0.27	0.20	0.42	0.34	0.32
BR(T ⁽¹⁾ → W ⁺ W ⁻ t)		0.09	0	0.10	0.04	0.14	0.13	0.02	0.02	0.18	0.16	0.08	0.08

Table 6. Benchmark points for the low scale MCHM₁₄ scan and their main features. Column headings indicate region, with red and orange meaning respectively Regions I and III (with same sign M_1 and M_4) and blue and cyan respectively for regions II and IV (with opposite sign M_1 and M_4).

with the requested precision to study the $t\bar{t}hh$ process (e.g. the various NR components) and to measure the branching ratios of various decays of the produced resonances, even if, for instance, the lightest one is detected at the HL-LHC.

5.1 Scanning Over Parameter Space

The numerical strategy we use here is the same as the one we followed for the Low Scale analysis and described in Subsection 3.1 but with the following extended range of parameters in order to perform a high scale scan. For the MCHM₅ we consider:

$$\begin{aligned}
|M_1| &\in [2, 30] \text{ TeV}, & M_4 &\in [2, 30] \text{ TeV}, \\
f &\in [0.8, 8.0] \text{ TeV}, & y_L &\in [0.5, 3.0],
\end{aligned}$$

and for the MCHM₁₄, we use:

$$\begin{aligned}
|M_1| &\in [2, 30] \text{ TeV}, & |M_4| &\in [2, 30] \text{ TeV}, & M_9 &\in [2, 30] \text{ TeV}, \\
f &\in [0.8, 8.0] \text{ TeV}, & y_L &\in [0.5, 3.0].
\end{aligned}$$

We divide the parameter space of the MCHM₅ and the MCHM₁₄ in the same regions we used for the Low Scale analysis (Sec. 4.1). In each region for each model we scanned 200 random points. We present the main results of the scans in Fig. 15 and Fig. 17, where we joined all the possible regions for each model.

Fig. 15 displays the normalized $t\bar{t}h$ cross section as a function of f for a center of mass energy of 100 TeV. As shown already in the low scale study, the $t\bar{t}h$ cross section depends mainly on the scale of global symmetry breaking f and, as expected, for high

values of f we get smaller deviations from the SM, either suppressed or enhanced (only in the MCHM_{14}).

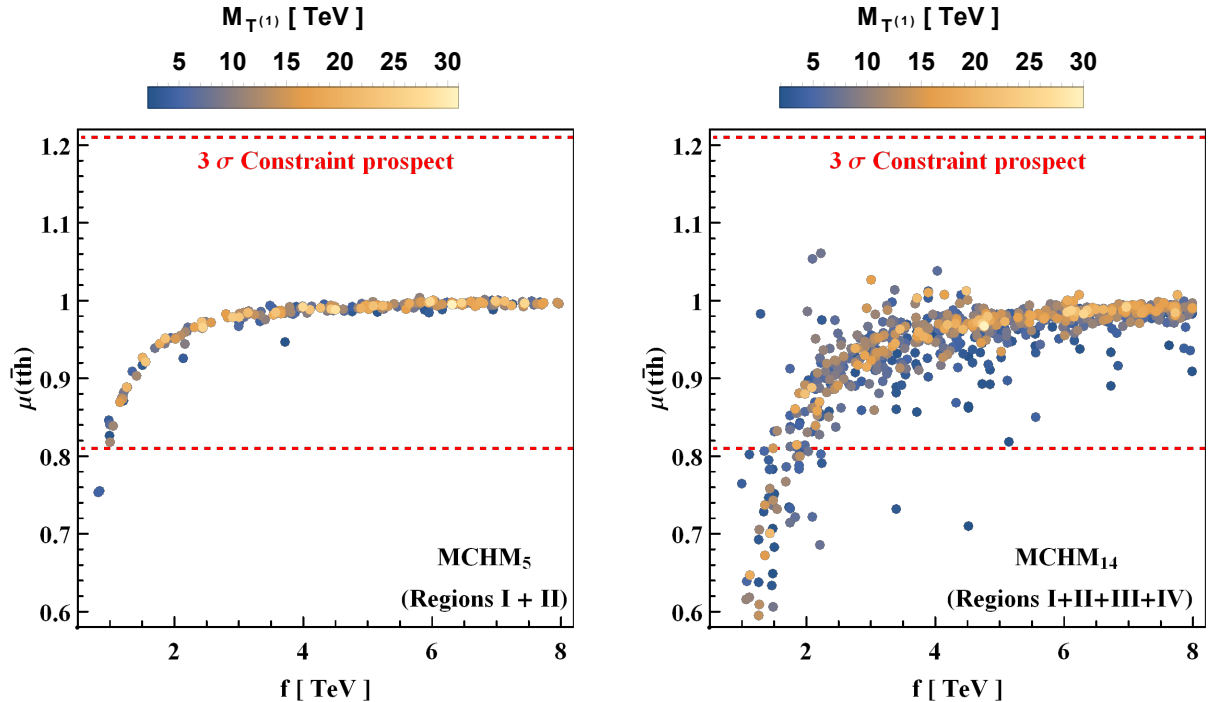


Figure 15. Normalized $t\bar{t}h$ cross section as a function of f . We also color code the lightest vector-like mass. These points are obtained by joining all the regions in each model. The dashed red lines represent the prospects for the 3σ uncertainty on the $t\bar{t}h$ signal strength after the HL-LHC measurements (see Sec. 5.2).

Fig. 17 shows the normalized $t\bar{t}hh$ cross section (at $\sqrt{s} = 100$ TeV) as a function of the mass of the lightest top resonance, $M_{T(1)}$, with color coded values of f . As explained in Subsection 3.7, at low scales the main contribution to this cross section comes from the QCD vector-like pair production. However, the later process undergoes a quick drop for heavy resonances, so it is expected that beyond certain value of $M_{T(1)}$ the QCD resonance pair production becomes a subdominant part of the total $t\bar{t}hh$ cross section. In the plots of Fig. 17, we see that this value is about $M_{T(1)} \approx 4$ TeV as the cross section becomes basically independent from $M_{T(1)}$ beyond that point. In the left plot, corresponding to the MCHM_5 , above this value there is no point with a $\mu(t\bar{t}hh)$ bigger than one, meaning that the main contributor is now the non-resonant part of the process, which, as we saw in Fig. 10, is directly related to $\mu(t\bar{t}h)$ and always suppressed w.r.t the SM. Since the later is, in turn, mainly controlled by the compositeness scale f (see Fig. 15), the points with smaller values of f have a more strongly suppressed cross section and as it increases, the cross section approaches the SM limit.

We see that, in the right plot of Fig. 17 (corresponding to the MCHM_{14}) there are still points with considerable enhancements with respect to the SM beyond $M_{T(1)} \approx 4$ TeV. There are two kinds of points with this behaviour: some points present enhancements in the $t\bar{t}h$ Yukawa coupling which reflect in enhancements in the NR- $t\bar{t}hh$ and consequently

in an increase of order 10% in $t\bar{t}hh$. The second case is more subtle and is responsible for the biggest cross sections in the region above $M_{T^{(1)}} \approx 4$ TeV. Those are finely tuned points, in which the parameters lead to strong coupling interaction between the top, a vector-like resonance and the Higgs. This vertex enters in diagrams like the one in Fig. 16, in which a single intermediate top partner is produced (not to be confused with weak single production), increasing the cross section as well. It is important to mention that the second type of points usually has a low compositeness scale ($f < 2$ TeV) and can be constrained by the increased precision on the measurement of the top Yukawa attainable by the HL-LHC (see Fig 15).

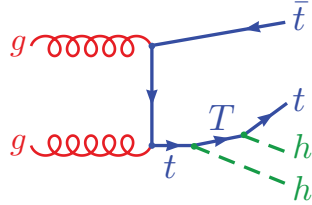


Figure 16. Example diagram for the Yukawa mediated single T contribution to $t\bar{t}hh$.

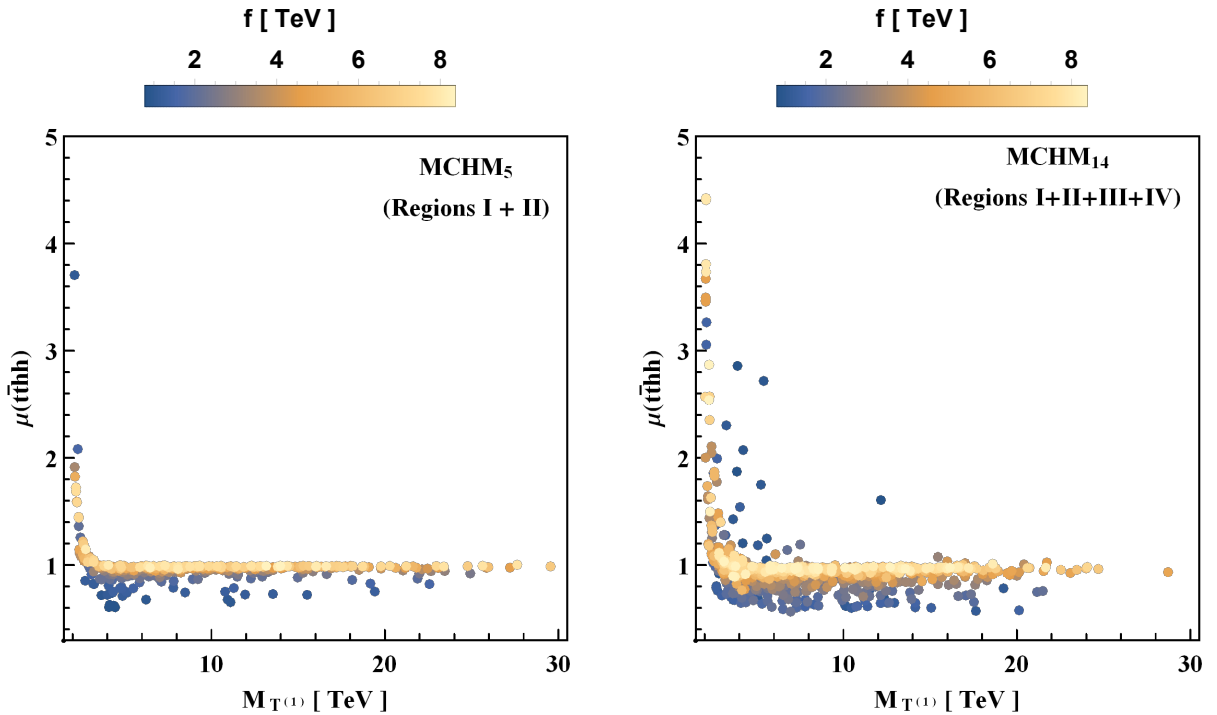


Figure 17. Normalized $t\bar{t}hh$ cross section as a function of the lightest $Q = 2/3$ resonance mass at $\sqrt{s} = 100$ TeV. The value of the global scale of symmetry breaking is also color coded. These points are obtained by joining all the regions in each model.

5.2 Cluster analysis applied to the MCHM at High scale

Following the analysis of Secs. 4.2 and 4.3 we look now at specific points in the parameter space in order to examine the phenomenological features of the MCHM at high scale. As we show below, the increased mass range in the scan demanded a slightly different strategy in regards to the clustering technique of Section 3.4. In what follows, we divided the points of the scan in smaller sets before clustering. This approach, together with the fact the phenomenological behaviour at higher scales is more uniform, provides enough points to showcase all the interesting features of the model. For that reason we have not chosen additional example points for the High Scale scan, and we proceed directly to the results of the clustering algorithm.

5.2.1 Clustering of the MCHM₅

We start with the 400 points of the scan in the previous section (200 in each region) and discard all points violating the following constraint on κ_t , the top Yukawa coupling normalized w.r.t. to the SM:

$$0.9 < \kappa_t < 1.1 \quad (5.1)$$

This constraint is based on the projected precision on the top Yukawa measurement in the High Luminosity phase of the LHC. In [51] the 1σ uncertainty on κ_t is projected to be 3.4% for an accumulated luminosity of 3000 fb^{-1} . We constrain our points to the region that is 3 times that uncertainty around the SM value $\kappa_t = 1$, as a rough estimate of the 3σ region. We do this in order to keep points that have a smaller chance of being constrained by measurements at the time when the 100 TeV pp collider starts its operation. We can directly translate eq. 5.1 into constraints in $\mu(t\bar{t}h)$, and we show these limits as red dashed lines in Fig. 15, where one can see that this allows for fairly small values of $\mu(t\bar{t}h)$ ($\gtrsim 0.8$). By the end of the HL-LHC phase the points close to that limit will be of course at the edge of the allowed region, and could be even excluded, specially if the central value of $\mu(t\bar{t}h)$ turns out to be above 1 or the precision is better than expected. But on the other hand, it is still a possibility that the opposite happens (central value of $\mu(t\bar{t}h) < 1$ for instance) so we understand it is too early to disregard those points.

The remaining points are clustered following the method described in Section 5.1. Different combinations of kinematic distributions are considered but, in all of them, the clustering procedure was giving too much weight to the position of peaks on points with lighter resonances, creating many low population clusters for those and leaving the ones with heavier resonances combined in a unique cluster. This is similar to what happened in the clusterization of the low Scale MCHM₅ (see cluster 3 in Fig. 12), but the problem is exacerbated by the fact that, in this case, we are working with a bigger range of parameters and, consequently, with a wider variety of resonance masses. As we are interested in selecting points distributed in the whole parameter space, we decide to first group the points in slices, guided by the mass of the lightest resonance, and then to apply the clustering algorithm to each slice individually. The following five slices, are used:

$$\begin{aligned}
2 \text{ TeV} &< M_{T^{(1)}} < 3 \text{ TeV} \\
3 \text{ TeV} &< M_{T^{(1)}} < 4 \text{ TeV} \\
4 \text{ TeV} &< M_{T^{(1)}} < 5 \text{ TeV} \\
5 \text{ TeV} &< M_{T^{(1)}} < 6 \text{ TeV} \\
6 \text{ TeV} &< M_{T^{(1)}} < 30 \text{ TeV}
\end{aligned} \tag{5.2}$$

In this way we ensure we are clustering the points in a more homogeneous way. The last slice groups all the points with resonances heavier than 6 TeV since, as we see in Fig. 17, it is expected that all of them possess similar kinematic characteristics because the contribution of the resonances for them are negligible. The selected clustering is realized by using the $M[t, h_1]$, $p_T[t]$ and $\theta[t]$ distributions and stopping at 2 clusters in each slice, for a total of 10 clusters. The plots showing the clustering in full detail are available online [64]. The benchmark points corresponding to each cluster are listed in Table 7.

		E ₁	E ₂	E ₃	E ₄	E ₅	E ₆	E ₇	E ₈	E ₉	E ₁₀
parameters	M ₁ (TeV)	22.7	19.2	11.1	23.0	26.5	3.6	19.3	10.5	-10.7	-22.9
	M ₄ (TeV)	2.4	2.1	3.2	3.2	4.0	22.5	5.1	5.1	25.6	13.5
	f (GeV)	1913	3273	7144	1190	1300	1711	1288	2812	2432	1199
	y _L	2.45	0.87	2.85	2.43	0.99	2.00	2.35	1.84	2.57	2.46
	y _R	1.10	1.24	2.01	1.54	3.53	1.31	2.35	3.13	1.11	2.62
$\mu(t\bar{t}h)$ (All Energies)		0.95	0.97	0.99	0.88	0.83	0.94	0.88	0.97	0.96	0.87
$\mu(t\bar{t}hh)$ (100 TeV)		1.26	1.91	1.03	0.82	0.81	0.86	0.75	0.91	0.92	0.73
NR- $t\bar{t}hh/t\bar{t}hh$ (100 TeV)		0.71	0.48	0.95	0.90	0.82	1.00	1.00	1.02	1.01	1.01
$M_{T^{(1)}}$ (TeV)		2.45	2.12	3.21	3.23	4.07	4.28	5.08	5.15	11.02	13.55
$M_{T^{(2)}}$ (TeV)		5.27	3.55	18.13	4.32	4.28	22.50	5.90	7.31	25.62	13.86
$M_{T^{(3)}}$ (TeV)		22.81	19.65	20.61	23.12	26.91	22.76	19.51	13.68	26.37	23.15
$M_{B^{(1)}}$ (TeV)		5.28	3.55	20.61	4.33	4.24	22.76	5.90	7.30	26.37	13.86
$M_{X_{5/3}}$ (TeV)		2.44	2.11	3.20	3.22	4.04	22.50	5.06	5.14	25.62	13.54
$\Gamma_{T^{(1)}}$ (TeV)		0.04	0.04	0.08	0.14	0.96	0.28	0.76	0.84	1.22	11.8
$\Gamma_{T^{(1)}}/M_{T^{(1)}}$		1.6%	1.9%	2.5%	4.3%	24%	6.5%	15%	16%	11%	87%
BR(T ⁽¹⁾ → t \bar{t})		0.35	0.38	0.29	0.29	0.15	0.26	0.18	0.17	0.25	0.04
BR(T ⁽¹⁾ → W ⁺ b)		0.003	0.004	0	0.001	0	0.50	0	0	0.50	0
BR(T ⁽¹⁾ → tZ)		0.34	0.37	0.28	0.28	0.33	0.25	0.18	0.18	0.25	0.04
BR(T ⁽¹⁾ → W ⁺ W ⁻ t)		0.30	0.25	0.43	0.43	0.52	0	0.64	0.65	0	0.92

Table 7. Benchmark points for the MCHM₅ at high scale and their main features. Red and blue column headings indicate points belonging to Region I and II respectively.

The first general feature to be noticed in Table 7 is the importance of the NR- $t\bar{t}hh$ contribution to the total cross-section. Only in point E_2 it is not the dominant contribution, although it is still about half of the cross section. Even in the points with resonances in the 2 ~ 3 TeV range the NR contribution is high (0.7 in E_1 , ≥ 0.9 in E_3 and E_4). As the resonances get heavier, the NR component becomes almost all of the cross section. The increasing suppression of the $T^{(1)}$ pair production also causes $\mu(t\bar{t}hh)$ to be close to or below 1 for the points with heavier resonances (E_3 to E_{10}), as expected for the NR contribution in the MCHM₅.

The second striking feature is the number of points with a sizeable or 3-body decay (all points with the exception of E_6 and E_9). The effect happens when both $M_{T^{(1)}}$ and $M_{X_{5/3}}$ are largely controlled by M_4 , and are thus almost degenerate (whereas in E_6 and

E_9 , $M_{T^{(1)}}$ is closer to M_1). In these cases, there is also a marked suppression of $\text{BR}(T^{(1)} \rightarrow W^+b)$. This was already present in the low scale scan but becomes more prominent here, and one can check in the Table that the 3-body decay becomes more important as $M_{T^{(1)}}$ increases. Considering the points with this property (which are the majority of the benchmark points) we see that the 3-body branching ratio increases from $\sim 10\%$ at $M_{T^{(1)}} \approx 1.3$ TeV (see Table 5) to quickly becoming the dominant decay channel around $M_{T^{(1)}} \approx 3$ TeV, being already 25% in point E_2 (with $M_{T^{(1)}} = 2.1$ TeV). This makes it extremely important to take three body decays into consideration if one wishes to push the direct search exclusion of top partners beyond the present ballpark of 1.3 TeV. Additionally, the fact that this decay happens through the exotically charged $X_{5/3}$, also highlights the importance of examining more complete models of the fermionic sector, as opposed to simplified models that only include a single electroweak doublet or singlet top partner.

On the other hand, points E_6 and E_9 exhibit the behaviour typically well captured by simplified models. In these, $M_{T^{(1)}} \approx M_1$ is well separated from the rest of the spectrum, which is dominated by masses close to a much higher M_4 . The branching ratios follow then the expected pattern: the W^+b channel branching ratio is twice that of the th and tZ channels.

Other features already present in the low scale scan are also present at higher scale, specially the presence of double peaked structures in many points. Among the benchmark points, we highlight points E_5 and E_{10} where we find two top partners close in mass. In fact in these two points, the exotic $X_{5/3}$ and the bottom partner $B^{(1)}$ are also close by, allowing the 3-body decay to go through either of those channels. This causes the width of $T^{(1)}$ to increase a lot: $(\Gamma/M)_{T^{(1)}} = 24\%$ for E_5 and even up to $(\Gamma/M)_{T^{(1)}} = 87\%$ for E_{10} . Points E_7 and E_8 also exhibit similar behaviour, but there is a bigger mass gap and smaller $(\Gamma/M)_{T^{(1)}}$.

Figure 19 shows the scanned points as well as the benchmark points in the $M_1 - M_4$ plane with color coded f . There, we see that the benchmark points obtained with the clustering technique are covering both regions of the model. Besides verifying the homogeneity of each cluster we also searched for points that have behaviours that deviate significantly from the benchmarks, and found none. This indicates that the behaviour of the model is quite uniform and well represented by the benchmark points, even in the region with a small number of them, as for instance in Region II (negative M_1). The same is true for regions with high M_1 , M_4 , and specially high f , as we are moving towards the decoupling limit of the model and the points become more similar to each other and to the SM (which explains why only one point, E_3 , was chosen to represent the high f region). For these reasons, it would be superfluous to choose and include additional example points.

5.2.2 Clustering of the MCHM₁₄

In the case of the MCHM₁₄ at high scale we started with 800 points evenly distributed in the four regions of the $M_1 - M_4$ space as described in Section 5.1. Then, we selected all points allowed by the constraint in Eq. 5.1 and proceed with the clustering technique. As in the MCHM₅, we divide the points in the five slices of Eq. 5.2. We stopped at 2

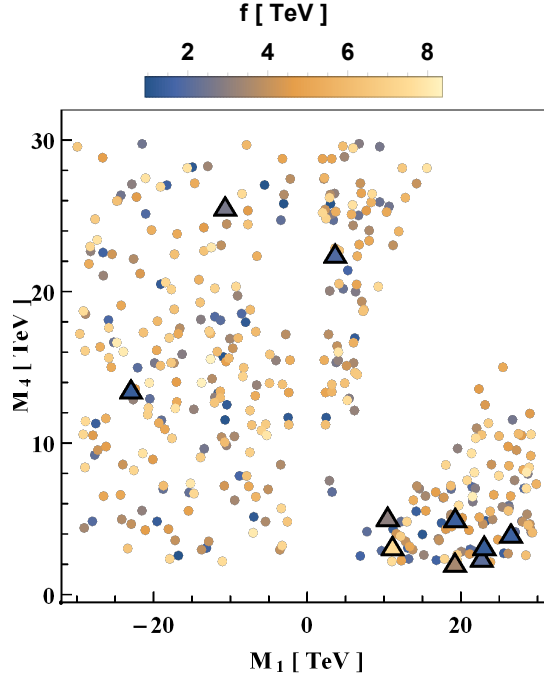


Figure 18. High scale scan of the MCHM₅ parameter space, including the benchmark points of Table 7 represented by triangles and the points satisfying the constraint in Eq. 5.1. The compositeness scale f is color coded.

or 3 clusters in each slice, depending on how homogeneous were the obtained clusters, and the corresponding benchmark points are listed in Table 8. The plots showing the clustering in full detail are available online [64].

Many features are similar to the MCHM₅: the NR- $t\bar{t}hh$ once again becomes dominant once $M_{T^{(1)}}$ goes above 3 TeV, and both $\mu(t\bar{t}h)$ and $\mu(t\bar{t}hh)$ go below 1 when that happens. In principle, the MCHM₁₄ could allow for an increased top Yukawa and thus $\mu(t\bar{t}h) > 1$ and $\mu(t\bar{t}hh) > 1$ even in the non-resonant regime. Only one point with that behaviour was selected by the algorithm (F_{11}), but all scales for that point are so high that it is almost SM-like.

In regard to the spectrum and decay of the lightest top partner, many points mimic the behaviour of the MCHM₅, but the situation is richer here:

- The points F_1, F_3, F_7, F_9 and F_{10} reproduce the dominant behaviour in the MCHM₅, with the masses of $T^{(1)}$ and $X_{2/3}$ essentially set by M_4 , large branching ratios in 3-body decays and suppressed Wb decays. All the important remarks made in that case apply.
- The points F_5 and F_8 have the split spectrum similar to E_6 and E_9 . The top partner has a mass set by M_1 and the rest of the spectrum is much heavier. Decay channels follow the pattern assumed in simplified models.
- The points F_2, F_4 and F_6 are qualitatively new. The mass scale is largely set by M_9 and we have three top partners that are degenerate not only among themselves,

		F ₁	F ₂	F ₃	F ₄	F ₅	F ₆	F ₇	F ₈	F ₉	F ₁₀	F ₁₁
parameters	M ₁ (TeV)	-10.1	4.10	25.2	14.5	-4.20	27.5	12.0	4.93	11.1	-17.6	-16.7
	M ₄ (TeV)	-2.27	-15.9	3.71	29.6	29.7	11.3	4.04	-10.5	-5.62	-7.20	-27.0
	M ₉ (TeV)	6.16	2.06	10.2	3.31	29.9	4.38	18.7	25.8	24.3	8.31	26.9
	f (TeV)	3.41	4.52	4.89	6.84	7.89	4.35	2.13	4.81	1.98	3.13	4.48
	y _L	1.29	1.83	0.53	2.07	2.41	2.20	2.23	2.58	1.93	1.33	2.38
	y _R	0.83	0.26	1.15	1.53	0.13	1.47	1.13	0.24	0.67	2.01	3.13
$\mu(t\bar{t}h)$ (All Energies)		0.93	0.86	0.96	0.92	0.97	0.98	0.87	0.97	0.86	0.88	1.01
$\mu(t\bar{t}hh)$ (100 TeV)		1.44	3.46	0.93	1.03	0.91	0.99	0.74	0.92	0.71	0.74	1.02
NR- $t\bar{t}hh/t\bar{t}hh$ (100 TeV)		0.59	0.22	0.97	0.81	1.02	0.97	0.99	1.01	1.00	1.02	0.99
M _{T⁽¹⁾} (TeV)		2.28	2.06	3.72	3.31	4.36	4.38	4.05	5.07	5.62	7.22	21.7
M _{T⁽²⁾} (TeV)		4.90	2.06	4.53	3.31	29.7	4.38	6.18	10.45	6.74	8.23	26.9
M _{T⁽³⁾} (TeV)		6.16	2.11	10.2	3.35	29.9	4.40	12.2	16.2	11.2	8.31	26.9
M _{B⁽¹⁾} (TeV)		4.92	2.06	4.52	3.31	29.9	4.38	6.22	16.2	6.77	8.23	27.0
M _{X_{5/3}⁽¹⁾} (TeV)		2.27	2.06	3.71	3.31	29.7	4.38	4.04	10.5	5.62	7.20	26.9
$\Gamma_{T^{(1)}} (TeV)$		0.05	0.06	0.24	0.18	0.83	0.25	0.28	0.63	0.23	3.00	45.8
$\Gamma_{T^{(1)}}/M_{T^{(1)}}$		2.2%	2.9%	6.4%	5.4%	19%	5.7%	6.9%	12%	4.1%	42%	211%
BR(T ⁽¹⁾ → t \bar{t})		0.36	0	0.24	0	0.25	0	0.23	0.25	0.16	0.10	0.04
BR(T ⁽¹⁾ → W ⁺ b)		0.006	0.27	0.001	0.21	0.50	0.16	0.005	0.50	0.007	0	0.07
BR(T ⁽¹⁾ → tZ)		0.35	0.53	0.25	0.41	0.25	0.32	0.23	0.25	0.16	0.11	0.03
BR(T ⁽¹⁾ → W ⁺ W ⁻ t)		0.28	0.20	0.50	0.39	0	0.52	0.54	0	0.68	0.79	0.86

Table 8. Benchmark points for the high scale MCHM₁₄ scan and their main features. Column headings indicate the region at which the point belongs, with red and orange meaning respectively Regions I and III (with same sign M_1 and M_4) and blue and cyan respectively for regions II and IV (with opposite sign M_1 and M_4).

but also coincide with the masses of the lightest exotically charged fermion and the bottom partner. The width of $T^{(1)}$ does not increase as in the degenerate cases of the MCHM₅, and there is a suppression of the th channel. A complete survey of all the decay channels of $T^{(2)}$ and $T^{(3)}$ would be needed to disentangle these states (and determine which are contributing to $t\bar{t}hh$ and in what degree), but that is beyond the scope of this work. We intend to explore this point in a future study.

Moreover, unlike the points F_4 and F_6 , the point F_2 , if still valid after HL-LHC, will be evidenced at a 100 TeV machine thanks to the high precision measurement of $\mu(t\bar{t}h)$ and, more importantly, to the large deviation from the SM in $\mu(t\bar{t}hh)$.

- The point F_{11} is really SM-like from several experimental viewpoints; even with the high precision reachable on $\mu(t\bar{t}h)$ and $\mu(t\bar{t}hh)$ measurements at a 100 TeV collider, it will not be possible to disentangle them from SM. Besides, the very high mass and highly degenerate in M_4 and M_9 resonance spectrum, only shows a highly dominant 3 body decay of $T^{(1)}$, as particular features. Let's note that points F_5 and F_8 have the same highly degenerate in M_4 and M_9 resonance spectrum but, as mentioned above, with a pattern of decay channels similar to simplified models. The F_{11} point would deserve some specific phenomenological and experimental study, that goes beyond the scope of this paper.

Figure 19 shows the benchmark points in the $M_1 - M_4$ plane with color coded values of f . The benchmark points obtained with the clustering cover this space homogeneously and then we decided also not to add example points.

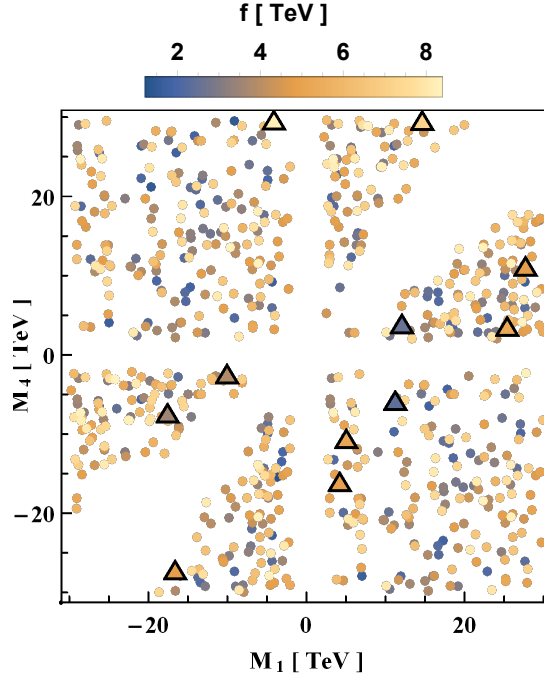


Figure 19. High scale scan of the MCHM₁₄ parameter space, including the benchmark points of Table 8 represented by triangles and the points satisfying the constraint in Eq. 5.1. The compositeness scale f is color coded.

6 Effective Field Theory Perspective

In the analysis reported in the previous sections, we always consider the effect of the fermionic resonances in the cross sections, however, for the points in parameter space with larger masses, decoupling occurs and the processes are then largely non-resonant. In this case, it can be useful to present expressions for the modifications of the SM couplings, in the context of an effective field theory, in which the heavy degrees of freedom are out of experimental reach and can be safely integrated out¹⁴, in order to facilitate a comparison with other non-resonant studies in the literature.

The aim of this section is to more generally show the interplay between the considered MCHM scenarios in their overall scanned parameter spaces, and the EFT framework. To do so we present our results in terms of modifications to the SM couplings, which are more directly comparable to the increasing number of experimental results on these parameters. It is straightforward to express these results in terms of a non-redundant operator basis such as the strongly-interacting light Higgs (SILH) basis [68]. The Higgs effective Lagrangian we consider here, after EWSB and neglecting the light fermion interactions,

¹⁴In the case of the pair production of top partners decaying to $t\bar{t}hh$, this occurs for $M_{T(1)} > 4$ TeV, as can be seen in figure 17 as the curve bends sharply when we go from resonant to non-resonant production.

is given below:

$$\begin{aligned} \mathcal{L}_h = & \frac{1}{2} \partial_\mu h \partial^\mu h - \frac{1}{2} m_h^2 h^2 - \kappa_\lambda \lambda_{\text{SM}} v h^3 - \frac{m_t}{v} \left(v + \kappa_t h + \frac{c_2}{v} h h \right) (\bar{t}_L t_R + \text{h.c.}) \\ & + \frac{1}{4} \frac{\alpha_s}{3\pi v} \left(c_g h - \frac{c_{2g}}{2v} h h \right) G^{\mu\nu} G_{\mu\nu} \end{aligned} \quad (6.1)$$

where κ_λ , κ_t , c_2 , c_g and c_{2g} are coefficients that encode the modifications to the SM. We do not present here the expression for c_{2g} as this operator will not contribute to the $t\bar{t}h$ and $t\bar{t}hh$ processes at tree level. The coupling κ_λ is the same in both the MCHM₅ and the MCHM₁₄:¹⁵

$$\kappa_\lambda = \frac{1 - 2\xi}{\sqrt{1 - \xi}} \quad (6.2)$$

For the MCHM₅, the remaining couplings are given by:

$$\kappa_t^5 = 1 + \left[-\frac{3}{2} + \frac{1}{2} \left(1 - \frac{1}{r_1^2} \right) \sin^2 \theta_L + (1 - r_1^2) \sin^2 \theta_R \right] \xi + \dots \quad (6.3)$$

$$c_2^5 = \left[-2 + \frac{3}{4} \left(1 - \frac{1}{r_1^2} \right) \sin^2 \theta_L + \frac{3}{2} (1 - r_1^2) \sin^2 \theta_R \right] \xi + \dots \quad (6.4)$$

$$c_g^5 = \frac{1 - 2\xi}{\sqrt{1 - \xi}} \quad (6.5)$$

Here we defined θ_L and θ_R by $\tan \theta_L = y_L f / M_4$ and $\tan \theta_R = y_R f / M_1$.

For the MCHM₁₄, the corresponding couplings are given by:

$$\kappa_t^{14} = 1 + \left[-4 - \frac{3}{2} \frac{1 - r_9}{1 - r_1} + \frac{5}{4} \left(2 - \frac{1}{r_1^2} - \frac{1}{r_9^2} \right) \sin^2 \theta_L + \frac{5}{2} (1 - r_1^2) \sin^2 \theta_R \right] \xi + \dots \quad (6.6)$$

$$c_2^{14} = \left[-6 - \frac{9}{4} \frac{1 - r_9}{1 - r_1} + \frac{15}{8} \left(1 - \frac{1}{r_1^2} + 1 - \frac{1}{r_9^2} \right) \sin^2 \theta_L + \frac{15}{4} (1 - r_1^2) \sin^2 \theta_R \right] \xi + \dots \quad (6.7)$$

$$c_g^{14} = c_g^t + c_g^b \quad (6.8)$$

with c_g^t and c_g^b defined in equations 2.29 and 2.30, respectively.

In Figs. 20 and 21, we have plotted selected EFT parameters against each other, for the points scanned in Sections. 4 and 5. The colors identify different regions in the parameter space of each model for Fig. 20, which covers the low scale region of the

¹⁵Some of the expressions below are reported also in [19], and presented here again for completeness.

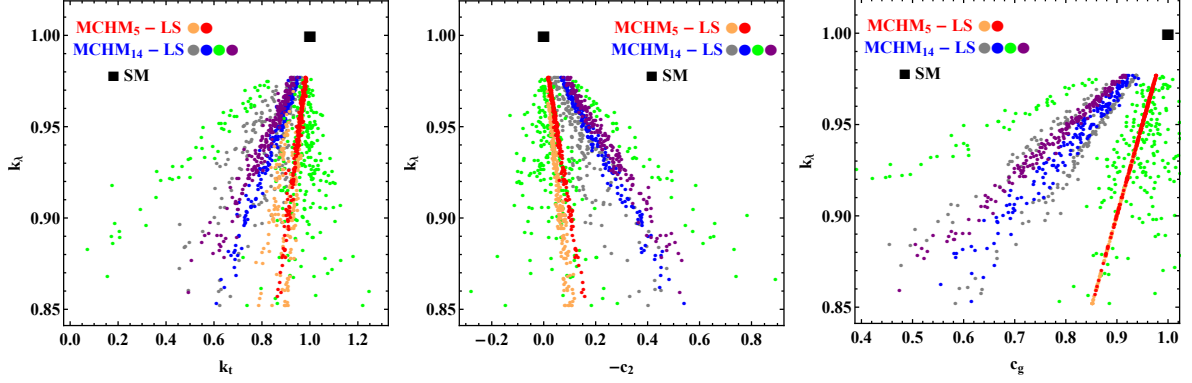


Figure 20. Values of some selected EFT parameters in the low scale scan of the $MCHM_5$ and the $MCHM_{14}$ parameter spaces. The colors indicate the different Regions in each model (I and II for the $MCHM_5$ and I, II, III and IV for the $MCHM_{14}$, in that order). The SM is represented by the black square.

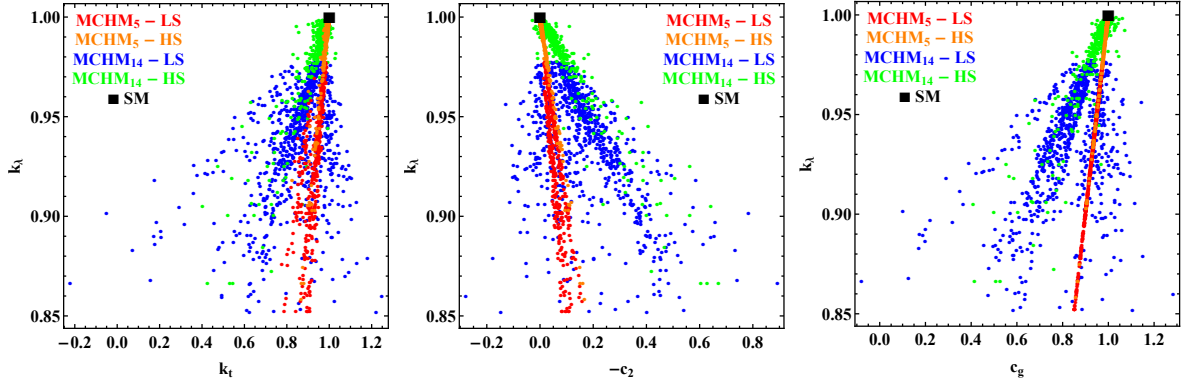


Figure 21. Values of some selected EFT parameters in the low and high scale scans of the $MCHM_5$ and the $MCHM_{14}$ parameter spaces. The SM parameters position is represented by the black square.

parameter space only, while in Fig. 21 the colors differentiate the low and high scale scans for the $MCHM_5$ and the $MCHM_{14}$. The vertical axis is chosen to be κ_λ , which depends only on the f scale, see Eq. (6.2). The low energy scan only covers up to $f \leq 2$ TeV, corresponding to $\kappa_\lambda \leq 0.98$, such that points with values closer to the SM will not be present in this case. On the horizontal axis, we show κ_t , $-c_2$ and c_g . Clearly the $MCHM_5$ and the $MCHM_{14}$ show distinct behavior, including between the different Regions defined in the $M_1 - M_4$ parameter space of each case (especially for $MCHM_{14}$), with considerable more spread for the $MCHM_{14}$, owing to a more involved dependence of the coefficients on the microscopic parameters in this case. The couplings defined above and their interplay can be used as discriminators in case a deviation from the SM is found; furthermore, by combining the $t\bar{t}h$ and $t\bar{t}h\bar{h}$ channels with other channels such as the double higgs production, which is sensitive to c_g , it should be possible to exclude some combinations of Region and MCHM scenarios or pinpoint which of them is realized in nature. In particular, one can verify that the $MCHM_5$ is much easier to discard than

the MCHM₁₄. For instance, it can be seen that the aforementioned enhancement in κ_t is only present for Region III in the **14**, while the relation $\kappa_\lambda = c_g$ is only satisfied for the MCHM₅; therefore, a measurement of $\kappa_t > 1$ or $\kappa_\lambda \neq c_g$ would argue strongly against the MCHM₅. Evidence of non-zero c_2 is also particularly interesting since this vertex is absent in the SM.

As expected, for smaller values of the compositeness scale f , the deviations from the SM are of course larger, and the separation between the different models is easier.

7 Conclusions and Outlook

The Minimal Composite Higgs Models MCHM₅ and MCHM₁₄ are studied here as an important show-case for the exploration of the beyond standard Model world, in the top-Higgs sector at high energy hadron colliders. The full generation and simulation framework is developed which allows a phenomenological analysis over the whole parameter space of these two models. Besides, the developed generation and simulation software defines a preliminary experimental framework; they are ready for use by more detailed data analysis at the LHC and HL-LHC experiments and by advanced detector simulations developed for the 100 TeV machines in project.

The focus is on the analysis of the $t\bar{t}h$ and $t\bar{t}hh$ production processes, covering in the later both the production of heavy fermions and the non-resonant contributions. In this paper we have gauged the relative contribution of these two cases to $t\bar{t}hh$ and shown that the non-resonant is sizeable, in fact dominant once the fermions are heavier than 4 TeV (even in the case with 100 TeV of center of mass energy), and gives access not only to the trilinear Higgs self-coupling, as it does in the SM case, but also to the double Yukawa coupling ($t\bar{t}hh$ vertex) which is introduced by the MCHM. The relative contributions of the top-Yukawa, the trilinear Higgs and the double Yukawa couplings were also analysed, showing that the trilinear Higgs coupling contributes approximately with 15% of the non-resonant cross section (see tables **3** and **4**).

A systematic exploration of the parameter space of both models was conducted. Using a clustering algorithm, it was possible to find a small number of benchmark points that showcase the phenomenology in a comprehensive way. These points were then complemented by exceptional points where needed, and the most important phenomenological data is summarized in tables **1**, **5** and **7** for the MCHM₅, and tables **2**, **6** and **8** for the MCHM₁₄. This exploration was done in two steps, first covering physics at “Low Scale”, where we focus on the part of the parameter space that is within reach of the HL-LHC. On a second step we extend the analysis to the “High Scale” region, with mass parameters reaching up to 30 TeV, which will be of interest for planned future colliders such as the 100 TeV FCC-hh and the SppC.

The first observations from the phenomenological and preliminary experimental analysis are that a deviation from the SM in the $t\bar{t}h$ production is also an essential measurement for MCHM. An increase will reject the MCHM₅ scenario and greatly refine the areas of the parameter space where MCHM₁₄ would be valid. A deficit instead, would make MCHM₅ and MCHM₁₄ both possible. The measurement of this observable is expected to be achieved with 3.4% accuracy at the HL-LHC and thus with a very

high accuracy (at least at the percent level) at the future high energy hadron collider in project at 100 TeV.

Regarding the search for fermionic resonances that are present in the partial compositeness scenario we explored, we find that in most of the benchmark points the 3-body decay channel of the lightest top-partner starts to become increasingly important as its mass grows. For all the benchmark points in this category, the 3-body decay is already 10% of the branching ratio when the mass is around 1.3 TeV, increasing to around 25% at 2 TeV and becomes the main decay channel when the top-partner reaches 3 TeV. The same points also have a marked suppression of decays to W^+b . As expected (see e.g. [39]), we find that it is not so common to have a “split spectrum” with a low lying top-partner separated in mass from other fermionic resonances since a full $SO(4)$ multiplet is controlled by a single mass parameter. This results in complicated interplay between the many states present, and is part of the reason for the increase in three 3-body decay channel. This makes it extremely important to take 3-body decays into consideration in future top-partner searches, and we intend to explore the decay patterns of all the fermionic resonances, and the resulting search strategies, in a upcoming work.

A comparison with the EFT, valid in energy regimes where the masses of the fermionic resonances are not reached, is also provided (see figures 20 and 21). This is specially interesting in the situation we are right now, and most probably will be at least until the end of the HL-LHC phase, in which no new states have been discovered but great improvements on the measurements of the coupling constants are being made. If deviations from the SM in more than one of these couplings are found, the specific combination of deviations can be used to differentiate not only between the MCHM₅ and the MCHM₁₄, but also between different regions of those models, as these regions generate different correlations between the effective couplings.

For the process $t\bar{t}hh$, both MCHM scenarios can deviate significantly from the SM expectation, either as a deficit or an increase. For this reason also this channel will play an important role in searches of composite Higgs models. The issue is the relatively low SM cross section of about 1 fb at tree level at 14 TeV, whereas $t\bar{t}h$ is roughly a factor 500 higher. Thus, the aim at HL-LHC will be to evidence this process and to get a first indication of a strong deviation from the SM. For really exploring MCHM, higher energy together with higher luminosity as foreseen in the pp colliders in project towards the second half of this century (100 TeV and exceeding 20 ab⁻¹ total integrated luminosity) are not only a plus but indeed even a necessity.

Acknowledgments

The authors thank Geum Bong Yu for useful discussions and references. One of us L. A. F. do Prado thanks IRFU-CEA, University Paris Saclay for hospitality. This work was supported by the São Paulo Research Foundation (FAPESP) under grants #2016/01343-7, #2013/01907-0, #2015/26624-6 and #2018/11505-0, by Science Without Borders / CAPES for UNESP-SPRACE under the Grant No. 88887.116917/2016-00 and in part by the Coordenação de Aperfeiçoamento de Pessoal de Nível Superior – Brasil (CAPES) – Finance Code 001.

A Representations of SO(5)

We use the following 5×5 matrix representation of the generators T^B of SO(5):

$$\begin{aligned}
T_L^1 &= \begin{pmatrix} 0 & 0 & 0 & -\frac{i}{2} & 0 \\ 0 & 0 & -\frac{i}{2} & 0 & 0 \\ 0 & \frac{i}{2} & 0 & 0 & 0 \\ \frac{i}{2} & 0 & 0 & 0 & 0 \\ 0 & 0 & 0 & 0 & 0 \end{pmatrix}, \quad T_L^2 = \begin{pmatrix} 0 & 0 & \frac{i}{2} & 0 & 0 \\ 0 & 0 & 0 & -\frac{i}{2} & 0 \\ -\frac{i}{2} & 0 & 0 & 0 & 0 \\ 0 & \frac{i}{2} & 0 & 0 & 0 \\ 0 & 0 & 0 & 0 & 0 \end{pmatrix}, \quad T_L^3 = \begin{pmatrix} 0 & -\frac{i}{2} & 0 & 0 & 0 \\ \frac{i}{2} & 0 & 0 & 0 & 0 \\ 0 & 0 & 0 & -\frac{i}{2} & 0 \\ 0 & 0 & \frac{i}{2} & 0 & 0 \\ 0 & 0 & 0 & 0 & 0 \end{pmatrix}, \\
T_R^1 &= \begin{pmatrix} 0 & 0 & 0 & \frac{i}{2} & 0 \\ 0 & 0 & -\frac{i}{2} & 0 & 0 \\ 0 & \frac{i}{2} & 0 & 0 & 0 \\ -\frac{i}{2} & 0 & 0 & 0 & 0 \\ 0 & 0 & 0 & 0 & 0 \end{pmatrix}, \quad T_R^2 = \begin{pmatrix} 0 & 0 & \frac{i}{2} & 0 & 0 \\ 0 & 0 & 0 & \frac{i}{2} & 0 \\ -\frac{i}{2} & 0 & 0 & 0 & 0 \\ 0 & -\frac{i}{2} & 0 & 0 & 0 \\ 0 & 0 & 0 & 0 & 0 \end{pmatrix}, \quad T_R^3 = \begin{pmatrix} 0 & -\frac{i}{2} & 0 & 0 & 0 \\ \frac{i}{2} & 0 & 0 & 0 & 0 \\ 0 & 0 & 0 & \frac{i}{2} & 0 \\ 0 & 0 & -\frac{i}{2} & 0 & 0 \\ 0 & 0 & 0 & 0 & 0 \end{pmatrix}, \\
T^{\hat{1}} &= \begin{pmatrix} 0 & 0 & 0 & 0 & -\frac{i}{\sqrt{2}} \\ 0 & 0 & 0 & 0 & 0 \\ 0 & 0 & 0 & 0 & 0 \\ 0 & 0 & 0 & 0 & 0 \\ \frac{i}{\sqrt{2}} & 0 & 0 & 0 & 0 \end{pmatrix}, \quad T^{\hat{2}} = \begin{pmatrix} 0 & 0 & 0 & 0 & 0 \\ 0 & 0 & 0 & 0 & -\frac{i}{\sqrt{2}} \\ 0 & 0 & 0 & 0 & 0 \\ 0 & 0 & 0 & 0 & 0 \\ 0 & \frac{i}{\sqrt{2}} & 0 & 0 & 0 \end{pmatrix}, \\
T^{\hat{3}} &= \begin{pmatrix} 0 & 0 & 0 & 0 & 0 \\ 0 & 0 & 0 & 0 & 0 \\ 0 & 0 & 0 & 0 & -\frac{i}{\sqrt{2}} \\ 0 & 0 & 0 & 0 & 0 \\ 0 & 0 & \frac{i}{\sqrt{2}} & 0 & 0 \end{pmatrix}, \quad T^{\hat{4}} = \begin{pmatrix} 0 & 0 & 0 & 0 & 0 \\ 0 & 0 & 0 & 0 & 0 \\ 0 & 0 & 0 & 0 & 0 \\ 0 & 0 & 0 & 0 & -\frac{i}{\sqrt{2}} \\ 0 & 0 & 0 & \frac{i}{\sqrt{2}} & 0 \end{pmatrix}, \tag{A.1}
\end{aligned}$$

which act on the fundamental representation $\mathbf{5}$ of SO(5) as $\delta\Psi_{\mathbf{5}} = T^B\Psi_{\mathbf{5}}$. We write the $\mathbf{5}$ representation (using a notation appropriate for states with $U(1)_X$ charge $X = 2/3$) as

$$\Psi_{\mathbf{5}}^{(2/3)} = X_{5/3} v_{\frac{1}{2}, \frac{1}{2}} + X_{2/3} v_{-\frac{1}{2}, \frac{1}{2}} + T v_{\frac{1}{2}, -\frac{1}{2}} + B v_{-\frac{1}{2}, -\frac{1}{2}} + \tilde{T} v_0, \tag{A.2}$$

where we used the normalized basis

$$v_{\frac{1}{2}, \frac{1}{2}} = \frac{1}{\sqrt{2}} \begin{pmatrix} i \\ -1 \\ 0 \\ 0 \\ 0 \end{pmatrix}, \quad v_{-\frac{1}{2}, \frac{1}{2}} = \frac{1}{\sqrt{2}} \begin{pmatrix} 0 \\ 0 \\ -i \\ -1 \\ 0 \end{pmatrix}, \quad v_{\frac{1}{2}, -\frac{1}{2}} = \frac{1}{\sqrt{2}} \begin{pmatrix} 0 \\ 0 \\ -i \\ 1 \\ 0 \end{pmatrix}, \quad v_{-\frac{1}{2}, -\frac{1}{2}} = \frac{1}{\sqrt{2}} \begin{pmatrix} -i \\ -1 \\ 0 \\ 0 \\ 0 \end{pmatrix},$$

and

$$v_0^T = (0, 0, 0, 0, 1).$$

The notation is such that the subindices a, b denote the $T_{L,R}^3$ eigenvalues: $T_L^3 v_{a,b} = a v_{a,b}$, $T_R^3 v_{a,b} = b v_{a,b}$, while v_0 denotes the complete singlet, $T_L^i v_0 = T_R^i v_0 = 0$. Furthermore, one has $T_L^+ v_{\frac{1}{2}, \pm \frac{1}{2}} = 0$, $T_L^+ v_{-\frac{1}{2}, \pm \frac{1}{2}} = v_{\frac{1}{2}, \pm \frac{1}{2}}$, $T_L^- v_{\frac{1}{2}, \pm \frac{1}{2}} = v_{-\frac{1}{2}, \pm \frac{1}{2}}$, $T_L^- v_{-\frac{1}{2}, \pm \frac{1}{2}} = 0$, and similarly $T_R^+ v_{\pm \frac{1}{2}, \frac{1}{2}} = 0$, $T_R^+ v_{\pm \frac{1}{2}, -\frac{1}{2}} = v_{\pm \frac{1}{2}, \frac{1}{2}}$, $T_R^- v_{\pm \frac{1}{2}, \frac{1}{2}} = v_{\pm \frac{1}{2}, -\frac{1}{2}}$, $T_R^- v_{\pm \frac{1}{2}, -\frac{1}{2}} = 0$, where $T_{L,R}^\pm \equiv T_{L,R}^1 \pm iT_{L,R}^2$ are the standard $SU(2)$ raising and lowering operators, satisfying

$$\begin{aligned} [T_L^3, T_L^\pm] &= \pm T_L^\pm, & [T_R^3, T_R^\pm] &= \pm T_R^\pm, \\ [T_L^+, T_L^-] &= 2T_L^3, & [T_R^+, T_R^-] &= 2T_R^3, \end{aligned}$$

and $[T_L^i, T_R^j] = 0$. The states satisfy the standard normalization

$$\begin{aligned} T_L^\pm |s_L, m_L; s_R, m_R\rangle &= \sqrt{s_L(s_L \mp 1) - m_L(m_L \mp 1)} |s_L, m_L \pm 1; s_R, m_R\rangle, \\ T_R^\pm |s_L, m_L; s_R, m_R\rangle &= \sqrt{s_R(s_R \mp 1) - m_R(m_R \mp 1)} |s_L, m_L; s_R, m_R \pm 1\rangle. \end{aligned}$$

Thus, $\Psi_4 \sim (X_{5/3}, X_{2/3}, T, B)$ is a bi-doublet $(\mathbf{2}, \mathbf{2})$ of $SU(2)_L \times SU(2)_R$ with $(s_L, s_R) = (1/2, 1/2)$, while $\Psi_1 \sim \tilde{T}$ is a singlet with $(s_L, s_R) = (0, 0)$.

The $\mathbf{14}$ representation of $SO(5)$ can be written in terms of a 5×5 symmetric and traceless matrix, such that the $SO(5)$ generators (A.1) act as $\delta\Psi_{\mathbf{14}} = [T^B, \Psi_{\mathbf{14}}]$. Using again the notation for states with $X = 2/3$, we write

$$\begin{aligned} \Psi_{\mathbf{14}}^{(2/3)} &= \tilde{T} S_0 + (X_{\frac{5}{3}} S_{\frac{1}{2}, \frac{1}{2}} + X_{\frac{2}{3}} S_{-\frac{1}{2}, \frac{1}{2}} + T S_{\frac{1}{2}, -\frac{1}{2}} + B S_{-\frac{1}{2}, -\frac{1}{2}}) \\ &+ [U_{\frac{8}{3}} S_{1,1} + U_{\frac{5}{3}} S_{0,1} + U_{\frac{2}{3}} S_{-1,1} \\ &+ V_{\frac{5}{3}} S_{1,0} + V_{\frac{2}{3}} S_{0,0} + V_{-\frac{1}{3}} S_{-1,0} \\ &+ F_{\frac{2}{3}} S_{1,-1} + F_{-\frac{1}{3}} S_{0,-1} + F_{-\frac{4}{3}} S_{-1,-1}] \end{aligned} \quad (\text{A.3})$$

which exhibits the decomposition $\mathbf{14} \sim (\mathbf{3}, \mathbf{3}) + (\mathbf{2}, \mathbf{2}) + (\mathbf{1}, \mathbf{1})$ under $SU(2)_L \times SU(2)_R$.

The notation for the basis $S_{a,b}$ is the same as explained above, e.g. $[T_L^3, S_{a,b}] = a S_{a,b}$, $[T_R^3, S_{a,b}] = b S_{a,b}$, while S_0 denotes the complete singlet, $[T_L^i, S_0] = [T_R^i, S_0] = 0$. The states $\Psi_9 \sim (U_{8/3}, U_{5/3}, U_{2/3}, V_{5/3}, V_{2/3}, V_{-1/3}, F_{2/3}, F_{-1/3}, F_{-4/3})$ transform as a bi-triplet of $SU(2)_L \times SU(2)_R$ with $(s_L, s_R) = (1, 1)$, and the bi-doublet Ψ_4 and singlet Ψ_1 follow the same notation used for the $\mathbf{5}$ of $SO(5)$ above. The subindices on the fields denote the electric charge, given by

$$Q = T_L^3 + T_R^3 + X. \quad (\text{A.4})$$

Explicitly, the $S_{a,b}$ and S_0 matrices are given by:

$$S_{1,1} = \frac{1}{2} \begin{pmatrix} 1 & i & 0 & 0 & 0 \\ i & -1 & 0 & 0 & 0 \\ 0 & 0 & 0 & 0 & 0 \\ 0 & 0 & 0 & 0 & 0 \\ 0 & 0 & 0 & 0 & 0 \end{pmatrix}, \quad S_{1,0} = \frac{1}{2\sqrt{2}} \begin{pmatrix} 0 & 0 & -1 & -i & 0 \\ 0 & 0 & -i & 1 & 0 \\ -1 & -i & 0 & 0 & 0 \\ -i & 1 & 0 & 0 & 0 \\ 0 & 0 & 0 & 0 & 0 \end{pmatrix}, \quad S_{1,-1} = \frac{1}{2} \begin{pmatrix} 0 & 0 & 0 & 0 & 0 \\ 0 & 0 & 0 & 0 & 0 \\ 0 & 0 & 1 & i & 0 \\ 0 & 0 & i & -1 & 0 \\ 0 & 0 & 0 & 0 & 0 \end{pmatrix},$$

$$S_{0,1} = \frac{1}{2\sqrt{2}} \begin{pmatrix} 0 & 0 & -1 & i & 0 \\ 0 & 0 & -i & -1 & 0 \\ -1 & -i & 0 & 0 & 0 \\ i & -1 & 0 & 0 & 0 \\ 0 & 0 & 0 & 0 & 0 \end{pmatrix}, S_{0,0} = \frac{1}{2} \begin{pmatrix} -1 & 0 & 0 & 0 & 0 \\ 0 & -1 & 0 & 0 & 0 \\ 0 & 0 & 1 & 0 & 0 \\ 0 & 0 & 0 & 1 & 0 \\ 0 & 0 & 0 & 0 & 0 \end{pmatrix}, S_{0,-1} = \frac{1}{2\sqrt{2}} \begin{pmatrix} 0 & 0 & 1 & i & 0 \\ 0 & 0 & -i & 1 & 0 \\ 1 & -i & 0 & 0 & 0 \\ i & 1 & 0 & 0 & 0 \\ 0 & 0 & 0 & 0 & 0 \end{pmatrix},$$

$$S_{-1,1} = \frac{1}{2} \begin{pmatrix} 0 & 0 & 0 & 0 & 0 \\ 0 & 0 & 0 & 0 & 0 \\ 0 & 0 & 1 & -i & 0 \\ 0 & 0 & -i & -1 & 0 \\ 0 & 0 & 0 & 0 & 0 \end{pmatrix}, S_{-1,0} = \frac{1}{2\sqrt{2}} \begin{pmatrix} 0 & 0 & 1 & -i & 0 \\ 0 & 0 & -i & -1 & 0 \\ 1 & -i & 0 & 0 & 0 \\ -i & -1 & 0 & 0 & 0 \\ 0 & 0 & 0 & 0 & 0 \end{pmatrix}, S_{-1,-1} = \frac{1}{2} \begin{pmatrix} 1 & -i & 0 & 0 & 0 \\ -i & -1 & 0 & 0 & 0 \\ 0 & 0 & 0 & 0 & 0 \\ 0 & 0 & 0 & 0 & 0 \\ 0 & 0 & 0 & 0 & 0 \end{pmatrix},$$

for the **9** of $SO(4) = SU(2)_L \times SU(2)_R$,

$$S_{\frac{1}{2},\frac{1}{2}} = \frac{1}{2} \begin{pmatrix} 0 & 0 & 0 & 0 & i \\ 0 & 0 & 0 & 0 & -1 \\ 0 & 0 & 0 & 0 & 0 \\ 0 & 0 & 0 & 0 & 0 \\ i & -1 & 0 & 0 & 0 \end{pmatrix}, S_{\frac{1}{2},-\frac{1}{2}} = \frac{1}{2} \begin{pmatrix} 0 & 0 & 0 & 0 & 0 \\ 0 & 0 & 0 & 0 & 0 \\ 0 & 0 & 0 & 0 & -i \\ 0 & 0 & 0 & 0 & 1 \\ 0 & 0 & -i & 1 & 0 \end{pmatrix},$$

$$S_{-\frac{1}{2},\frac{1}{2}} = \frac{1}{2} \begin{pmatrix} 0 & 0 & 0 & 0 & 0 \\ 0 & 0 & 0 & 0 & 0 \\ 0 & 0 & 0 & 0 & -i \\ 0 & 0 & 0 & 0 & -1 \\ 0 & 0 & -i & -1 & 0 \end{pmatrix}, S_{-\frac{1}{2},-\frac{1}{2}} = \frac{1}{2} \begin{pmatrix} 0 & 0 & 0 & 0 & -i \\ 0 & 0 & 0 & 0 & -1 \\ 0 & 0 & 0 & 0 & 0 \\ 0 & 0 & 0 & 0 & 0 \\ -i & -1 & 0 & 0 & 0 \end{pmatrix},$$

for the **4** of $SO(4)$, and

$$S_0 = \frac{1}{2\sqrt{5}} \begin{pmatrix} 1 & 0 & 0 & 0 & 0 \\ 0 & 1 & 0 & 0 & 0 \\ 0 & 0 & 1 & 0 & 0 \\ 0 & 0 & 0 & 1 & 0 \\ 0 & 0 & 0 & 0 & -4 \end{pmatrix}.$$

for the $SO(4)$ singlet. These matrices form an orthonormal basis: $\text{Tr}(S_A^* S_B) = \delta_{AB}$.

B Embeddings of $SO(4)$ into $SO(5)$

The four NGBs resulting from the spontaneous breaking of $SO(5) \rightarrow SO(4) = SU(2)_L \times SU(2)_R$ can be parametrized as

$$U = e^{i\frac{\sqrt{2}}{f} h^{\hat{a}} T^{\hat{a}}}, \quad (\text{B.1})$$

where $T^{\hat{a}}$ are the (four) broken generators in $SO(5)/SO(4)$ given in Eq (A.1) and f is the scale of spontaneous symmetry breaking. The $h^{\hat{a}}$ transform as a 4-plet of $SO(4)$, and can be arranged in a doublet of $SU(2)_L$ as:

$$H = \frac{1}{\sqrt{2}} \begin{pmatrix} h_2 + ih_1 \\ h_4 - ih_3 \end{pmatrix}. \quad (\text{B.2})$$

One can assume that EWSB proceeds through a non-vanishing vev $h_0 = \langle h_4 \rangle$, with the vev's of the other components vanishing. In unitary gauge, $h_1 = h_2 = h_3 = 0$ and $h_4 = h_0 + h$, where h is the physical Higgs boson. Using the explicit form of the broken generators results in the matrix given in Eq. (2.1).

It is also easy to embed the various fermion $SO(4)$ multiplets used in the main text into (incomplete) representations of $SO(5)$ that simplify the writing of the Lagrangian. For example,

- For the MCHM₅:

The elementary fermions are written as

$$\begin{aligned} Q_L^5 &= t_L v_{\frac{1}{2}, -\frac{1}{2}} + b_L v_{-\frac{1}{2}, -\frac{1}{2}}, \\ T_R^5 &= t_R v_0, \end{aligned}$$

and the composite fermions are written as

$$\begin{aligned} \Psi_4 &= X_{5/3} v_{\frac{1}{2}, \frac{1}{2}} + X_{2/3} v_{-\frac{1}{2}, \frac{1}{2}} + T v_{\frac{1}{2}, -\frac{1}{2}} + B v_{-\frac{1}{2}, -\frac{1}{2}}, \\ \Psi_1 &= \tilde{T} v_0. \end{aligned}$$

These result in Eqs. (2.8) and (2.9).

- For the MCHM₁₄:

The elementary fermions are written as

$$\begin{aligned} Q_L^{14} &= t_L S_{\frac{1}{2}, -\frac{1}{2}} + b_L S_{-\frac{1}{2}, -\frac{1}{2}}, \\ T_R^{14} &= t_R S_0, \end{aligned}$$

and the composite fermions are written as

$$\begin{aligned} \Psi_9 &= [U_{\frac{8}{3}} S_{1,1} + U_{\frac{5}{3}} S_{0,1} + U_{\frac{2}{3}} S_{-1,1} \\ &\quad + V_{\frac{5}{3}} S_{1,0} + V_{\frac{2}{3}} S_{0,0} + V_{-\frac{1}{3}} S_{-1,0} \\ &\quad + F_{\frac{2}{3}} S_{1,-1} + F_{-\frac{1}{3}} S_{0,-1} + F_{-\frac{4}{3}} S_{-1,-1}] \\ \Psi_4 &= X_{5/3} S_{\frac{1}{2}, \frac{1}{2}} + X_{2/3} S_{-\frac{1}{2}, \frac{1}{2}} + T S_{\frac{1}{2}, -\frac{1}{2}} + B S_{-\frac{1}{2}, -\frac{1}{2}}, \\ \Psi_1 &= \tilde{T} S_0. \end{aligned}$$

All of these are traceless, symmetric 5×5 matrices. It is then straightforward to form a complete **14** of $SO(5)$ as

$$\Psi_{14} = \Psi_9 + \Psi_4 + \Psi_1.$$

C Explicit form of gauge and Higgs interactions

In unitary gauge, the gauged d_μ and e_μ symbols are given by

$$d_\mu = \left\{ \frac{g}{\sqrt{2}} W_\mu^1 s_h, \frac{g}{\sqrt{2}} W_\mu^2 s_h, \frac{gW_\mu^3 - g'B_\mu}{\sqrt{2}} s_h, \frac{\partial_\mu h}{f} \right\}$$

$$e_\mu = \frac{i}{2} \begin{pmatrix} 0 & -g'B_\mu - gW_\mu^3 & gW_\mu^2 & -gW_\mu^1 c_h \\ g'B_\mu + gW_\mu^3 & 0 & -gW_\mu^1 & -gW_\mu^2 c_h \\ -gW_\mu^2 & gW_\mu^1 & 0 & (g'B_\mu - gW_\mu^3) c_h \\ gW_\mu^1 c_h & gW_\mu^2 c_h & -(g'B_\mu - gW_\mu^3) c_h & 0 \end{pmatrix}, \quad (\text{C.1})$$

where $c_h = \cos \frac{h_0+h}{f}$ and $s_h = \sin \frac{h_0+h}{f}$. Under $SO(4)$, d_μ^i transforms in the fundamental and e_μ^a in the adjoint. In terms of these, as well as the fermion embeddings from the previous appendices, we may write explicitly the vertices from the Lagrangians $\mathcal{L}_{\text{int}}^{5,14}$ in the interaction basis as

$$\mathcal{L}_{\text{int}}^5 = c_R \left\{ g\sqrt{\xi} \left[\frac{1}{\sqrt{2}} (\bar{X}_{5/3})_R W^+ \tilde{T}_R - \frac{1}{\sqrt{2}} \bar{B}_R W^- \tilde{T}_R - \frac{1}{2c_w} \bar{T}_R \not{Z} \tilde{T}_R \right. \right. \\ \left. \left. - \frac{1}{2c_w} (\bar{X}_{2/3})_R \not{Z} \tilde{T}_R \right] + i \left[(\bar{X}_{2/3})_R - \bar{T}_R \right] \frac{\not{\partial} h}{f} \tilde{T}_R \right\} + (R \rightarrow L) + \text{h.c.} \quad (\text{C.2})$$

$$\begin{aligned}
\mathcal{L}_{\text{int}}^{14} = & c_4 \left[g\sqrt{\xi} \left(\frac{1}{\sqrt{2}} \bar{X}_{5/3} \mathcal{W}^+ \tilde{T} - \frac{1}{\sqrt{2}} \bar{B} \mathcal{W}^- \tilde{T} - \frac{1}{2c_w} \bar{T} \not{Z} \tilde{T} - \frac{1}{2c_w} \bar{X}_{2/3} \not{Z} \tilde{T} \right) \right. \\
& \left. + i \left(\bar{X}_{2/3} - \bar{T} \right) \frac{\not{\partial} h}{f} \tilde{T} \right] \\
& - \frac{1}{4} c_9 \frac{g_2}{c_w} \sqrt{\xi} \left\{ \sqrt{2} \left[\bar{V}_{-1/3} + \bar{F}_{-1/3} \right] \not{Z} B + \left[\bar{V}_{2/3} + 2\bar{U}_{2/3} \right] \not{Z} X_{2/3} \right. \\
& \left. + \left[\bar{V}_{2/3} + 2\bar{F}_{2/3} \right] \not{Z} T + \sqrt{2} \left[\bar{U}_{5/3} + \bar{V}_{5/3} \right] \not{Z} X_{5/3} \right\} \\
& - \frac{1}{4} c_9 g_2 \sqrt{\xi} \left\{ \sqrt{2} \bar{V}_{2/3} \mathcal{W}^- \bar{X}_{5/3} + 2\sqrt{2} \bar{F}_{-4/3} \mathcal{W}^- B + 2\bar{F}_{-1/3} \mathcal{W}^- T + 2\bar{V}_{-1/3} \mathcal{W}^- X_{2/3} \right. \\
& \left. - \sqrt{2} \bar{V}_{2/3} \mathcal{W}^+ B + 2\sqrt{2} \bar{U}_{8/3} \mathcal{W}^+ X_{5/3} + 2\bar{V}_{5/3} \mathcal{W}^+ T + 2\bar{U}_{5/3} \mathcal{W}^+ X_{2/3} \right\} \\
& + \frac{i}{2f} c_9 \left\{ \sqrt{2} \left[\bar{V}_{-1/3} - \bar{F}_{-1/3} \right] \not{\partial} h B + \left[\bar{V}_{2/3} - 2\bar{F}_{2/3} \right] \not{\partial} h T + \right. \\
& \left. \left[2\bar{U}_{2/3} - \bar{V}_{2/3} \right] \not{\partial} h X_{2/3} + \sqrt{2} \left[\bar{U}_{5/3} - \bar{V}_{5/3} \right] \not{\partial} h X_{5/3} \right\} \\
& + \frac{i c_{T9}}{4\pi f^3} \partial_\mu h \partial^\mu h \left[\bar{U}_{2/3} - \bar{V}_{2/3} + \bar{F}_{2/3} \right] \tilde{T} \\
& + \frac{c_{T9} g_2 \sqrt{\xi}}{4\pi f^2 c_w} Z_\mu \left[\partial^\mu h \left(\bar{F}_{2/3} - \bar{U}_{2/3} \right) + W_\mu^+ \left(\bar{U}_{5/3} - \bar{V}_{5/3} \right) + W_\mu^- \left(\bar{F}_{-1/3} - \bar{V}_{-1/3} \right) \right] \tilde{T} \\
& + \frac{i c_{T9} g_2^2 \xi}{8\pi f} \left[-\frac{Z_\mu Z^\mu}{2c_w} \left(\bar{U}_{2/3} + \bar{V}_{2/3} + \bar{F}_{2/3} \right) - W_\mu^+ W^{+\mu} \bar{U}_{8/3} - W_\mu^- W^{-\mu} \bar{F}_{-4/3} \right. \\
& \left. + W_\mu^+ W^{-\mu} \bar{V}_{2/3} - \frac{Z_\mu W^{-\mu}}{c_w} \left(\bar{V}_{-1/3} + \bar{F}_{-1/3} \right) + \frac{Z_\mu W^{+\mu}}{c_w} \left(\bar{U}_{5/3} + \bar{V}_{5/3} \right) \right] \tilde{T} + \text{h. c.},
\end{aligned}$$

where c_w is the cosine of the Weinberg angle.

Furthermore, the e_μ symbol in the covariant derivatives lead to compositeness corrected electroweak interactions for the resonances in the fourplet and nonet, given by

$$\begin{aligned}
\mathcal{L}_{\text{gauge}}^5 = & \bar{\Psi}_4 \left(\frac{2}{3} g' \not{B} - \not{\epsilon} \right) \Psi_4 \\
= & \frac{g}{c_w} \left[\left(-\frac{1}{2} + \frac{1}{3} s_w^2 \right) \bar{B} \not{Z} B + \left(\frac{1}{2} - \frac{5}{3} s_w^2 \right) \bar{X}_{5/3} \not{Z} X_{5/3} \right. \\
& \left. + \left(\frac{\sqrt{1-\xi}}{2} - \frac{2}{3} s_w^2 \right) \bar{T} \not{Z} T + \left(-\frac{\sqrt{1-\xi}}{2} - \frac{2}{3} s_w^2 \right) \bar{X}_{2/3} \not{Z} X_{2/3} \right] \\
& + \frac{g}{\sqrt{2}} \frac{1 + \sqrt{1-\xi}}{2} \left[\bar{B} \mathcal{W}^- T + \bar{X}_{5/3} \mathcal{W}^+ X_{2/3} + \text{h. c.} \right] \\
& + \frac{g}{\sqrt{2}} \frac{1 - \sqrt{1-\xi}}{2} \left[\bar{X}_{5/3} \mathcal{W}^+ T + \bar{B} \mathcal{W}^- X_{2/3} + \text{h. c.} \right], \tag{C.3}
\end{aligned}$$

plus standard photon couplings, for the fourplet (these are the same as in reference [39], reported here again for completeness), and

$$\begin{aligned}
\mathcal{L}_{\text{gauge}}^{14} &= \bar{\Psi}_9 \left(\frac{2}{3} g' \not{B} \Psi_9 - [\not{\epsilon}, \Psi_9] \right) \\
&= \frac{g}{c_w} \left[\left(-\sqrt{1-\xi} + -\frac{2}{3} s_w^2 \right) \bar{U}_{2/3} \not{Z} U_{2/3} + \left(\frac{1-\sqrt{1-\xi}}{2} - \frac{5}{3} s_w^2 \right) \bar{U}_{5/3} \not{Z} U_{5/3} \right. \\
&\quad + \left(\frac{1}{2} - \frac{8}{3} s_w^2 \right) \bar{U}_{8/3} \not{Z} U_{8/3} + \left(-\frac{1+\sqrt{1-\xi}}{2} + \frac{1}{3} s_w^2 \right) \bar{V}_{-1/3} \not{Z} V_{-1/3} \\
&\quad + -\frac{2}{3} s_w^2 \bar{V}_{2/3} \not{Z} V_{2/3} + \left(\frac{1+\sqrt{1-\xi}}{2} + \frac{1}{3} s_w^2 \right) \bar{V}_{5/3} \not{Z} V_{5/3} \\
&\quad + \left(-1 + \frac{4}{3} s_w^2 \right) \bar{F}_{-4/3} \not{Z} F_{-4/3} + \left(-\frac{1-\sqrt{1-\xi}}{2} + \frac{1}{3} s_w^2 \right) \bar{F}_{-1/3} \not{Z} F_{-1/3} \\
&\quad \left. + \left(\sqrt{1-\xi} - \frac{2}{3} s_w^2 \right) \bar{F}_{2/3} \not{Z} F_{2/3} \right] \\
&\quad + \frac{g}{2} (1 + \sqrt{1-\xi}) \left[\bar{V}_{5/3} \not{W}^+ V_{2/3} + \bar{V}_{2/3} \not{W}^+ V_{-1/3} \right. \\
&\quad + \bar{F}_{-1/3} \not{W}^+ F_{-4/3} + \bar{F}_{2/3} \not{W}^+ F_{-1/3} \\
&\quad \left. + \bar{U}_{8/3} \not{W}^+ U_{5/3} + \bar{U}_{5/3} \not{W}^+ U_{2/3} + \text{h. c.} \right] \\
&\quad + \frac{g}{2} (1 - \sqrt{1-\xi}) \left[\bar{V}_{-1/3} \not{W}^+ F_{-4/3} + \bar{V}_{2/3} \not{W}^+ F_{-1/3} \right. \\
&\quad + \bar{V}_{5/3} \not{W}^+ F_{2/3} + \bar{U}_{5/3} \not{W}^+ V_{2/3} \\
&\quad \left. + \bar{U}_{8/3} \not{W}^+ V_{5/3} + \bar{U}_{2/3} \not{W}^+ V_{-1/3} + \text{h. c.} \right], \tag{C.4}
\end{aligned}$$

plus standard photon couplings, for the nonet.

References

- [1] ATLAS collaboration, G. Aad et al., *Observation of a new particle in the search for the Standard Model Higgs boson with the ATLAS detector at the LHC*, *Phys. Lett.* **B716** (2012) 1 [1207.7214].
- [2] CMS collaboration, S. Chatrchyan et al., *Observation of a new boson at a mass of 125 GeV with the CMS experiment at the LHC*, *Phys. Lett.* **B716** (2012) 30 [1207.7235].
- [3] K. Agashe, R. Contino and A. Pomarol, *The Minimal composite Higgs model*, *Nucl. Phys.* **B719** (2005) 165 [hep-ph/0412089].
- [4] L. Randall and R. Sundrum, *A Large mass hierarchy from a small extra dimension*, *Phys. Rev. Lett.* **83** (1999) 3370 [hep-ph/9905221].
- [5] ATLAS collaboration, M. Aaboud et al., *Observation of Higgs boson production in association with a top quark pair at the LHC with the ATLAS detector*, *Phys. Lett.* **B784** (2018) 173 [1806.00425].
- [6] CMS collaboration, A. M. Sirunyan et al., *Observation of $t\bar{t}H$ production*, *Phys. Rev. Lett.* **120** (2018) 231801 [1804.02610].

- [7] L. A. F. do Prado, “Exploring the Higgs sector Beyond the Standard Model with the Top Yukawa coupling: a phenomenological and experimental search.” PhD thesis defended in July, 2020, available at <https://repositorio.unesp.br/handle/11449/193301?locale-attribute=en>.
- [8] ATLAS collaboration, M. Aaboud et al., *Search for pair production of up-type vector-like quarks and for four-top-quark events in final states with multiple b-jets with the atlas detector*, *JHEP* **07** (2018) 089 [[1803.09678](#)].
- [9] ATLAS collaboration, M. Aaboud et al., *Combination of the searches for pair-produced vector-like partners of the third-generation quarks at $\sqrt{s} = 13$ tev with the atlas detector*, [1808.02343](#).
- [10] CMS collaboration, A. M. Sirunyan et al., *Search for vector-like T and B quark pairs in final states with leptons at $\sqrt{s} = 13$ TeV*, *JHEP* **08** (2018) 177 [[1805.04758](#)].
- [11] FCC collaboration, A. Abada, M. Abbrescia, S. AbdusSalam et al., *FCC-hh: The Hadron Collider*, *Eur. Phys. J. Spec. Top.* **228** (2019) 755–1107.
- [12] CEPC STUDY GROUP collaboration, *CEPC Conceptual Design Report: Volume 1 - Accelerator*, [1809.00285](#).
- [13] J. Gao, *CEPC and SPPC Status from the completion of the CDR towards TDR*, *Journal of Modern Physics A* (2020) to be published.
- [14] G. Panico and A. Wulzer, *The Composite Nambu-Goldstone Higgs*, *Lect. Notes Phys.* **913** (2016) pp.1 [[1506.01961](#)].
- [15] A. Falkowski, F. Riva and A. Urbano, *Higgs at last*, *JHEP* **11** (2013) 111 [[1303.1812](#)].
- [16] M. Carena, L. Da Rold and E. Pontón, *Minimal Composite Higgs Models at the LHC*, *JHEP* **06** (2014) 159 [[1402.2987](#)].
- [17] G. Buchalla, O. Cata and C. Krause, *A Systematic Approach to the SILH Lagrangian*, *Nucl. Phys.* **B894** (2015) 602 [[1412.6356](#)].
- [18] V. Sanz and J. Setford, *Composite Higgs Models after Run 2*, *Adv. High Energy Phys.* **2018** (2018) 7168480 [[1703.10190](#)].
- [19] D. Liu, I. Low and C. E. M. Wagner, *Modification of Higgs Couplings in Minimal Composite Models*, *Phys. Rev.* **D96** (2017) 035013 [[1703.07791](#)].
- [20] A. Banerjee, G. Bhattacharyya, N. Kumar and T. S. Ray, *Constraining Composite Higgs Models using LHC data*, *JHEP* **03** (2018) 062 [[1712.07494](#)].
- [21] J. de Blas, O. Eberhardt and C. Krause, *Current and Future Constraints on Higgs Couplings in the Nonlinear Effective Theory*, *JHEP* **07** (2018) 048 [[1803.00939](#)].
- [22] K. Agashe, R. Contino, L. Da Rold and A. Pomarol, *A Custodial symmetry for $Zb\bar{b}$* , *Phys. Lett.* **B641** (2006) 62 [[hep-ph/0605341](#)].
- [23] M. Carena, E. Pontón, J. Santiago and C. E. M. Wagner, *Light Kaluza Klein States in Randall-Sundrum Models with Custodial $SU(2)$* , *Nucl. Phys.* **B759** (2006) 202 [[hep-ph/0607106](#)].
- [24] C. Anastasiou, E. Furlan and J. Santiago, *Realistic Composite Higgs Models*, *Phys. Rev.* **D79** (2009) 075003 [[0901.2117](#)].

- [25] A. Orgogozo and S. Rychkov, *The S parameter for a Light Composite Higgs: a Dispersion Relation Approach*, *JHEP* **06** (2013) 014 [[1211.5543](#)].
- [26] C. Grojean, O. Matsedonskyi and G. Panico, *Light top partners and precision physics*, *JHEP* **10** (2013) 160 [[1306.4655](#)].
- [27] A. Pich, I. Rosell and J. J. Sanz-Cillero, *Oblique S and T Constraints on Electroweak Strongly-Coupled Models with a Light Higgs*, *JHEP* **01** (2014) 157 [[1310.3121](#)].
- [28] C. Englert, A. Freitas, M. M. Muhlleitner, T. Plehn, M. Rauch, M. Spira et al., *Precision Measurements of Higgs Couplings: Implications for New Physics Scales*, *J. Phys.* **G41** (2014) 113001 [[1403.7191](#)].
- [29] D. Croon, B. M. Dillon, S. J. Huber and V. Sanz, *Exploring holographic Composite Higgs models*, *JHEP* **07** (2016) 072 [[1510.08482](#)].
- [30] A. Pomarol and F. Riva, *The Composite Higgs and Light Resonance Connection*, *JHEP* **08** (2012) 135 [[1205.6434](#)].
- [31] G. Panico, M. Redi, A. Tesi and A. Wulzer, *On the Tuning and the Mass of the Composite Higgs*, *JHEP* **03** (2013) 051 [[1210.7114](#)].
- [32] M. Montull, F. Riva, E. Salvioni and R. Torre, *Higgs Couplings in Composite Models*, *Phys. Rev.* **D88** (2013) 095006 [[1308.0559](#)].
- [33] A. Carmona and F. Goertz, *A naturally light Higgs without light Top Partners*, *JHEP* **05** (2015) 002 [[1410.8555](#)].
- [34] S. Kanemura, K. Kaneta, N. Machida, S. Odori and T. Shindou, *Single and double production of the higgs boson at hadron and lepton colliders in minimal composite higgs models*, *Phys. Rev.* **D94** (2016) 015028 [[1603.05588](#)].
- [35] M. B. Gavela, K. Kanshin, P. A. N. Machado and S. Saa, *The linear-non-linear frontier for the Goldstone Higgs*, *Eur. Phys. J.* **C76** (2016) 690 [[1610.08083](#)].
- [36] S. R. Coleman, J. Wess and B. Zumino, *Structure of phenomenological Lagrangians. 1.*, *Phys. Rev.* **177** (1969) 2239.
- [37] C. G. Callan, Jr., S. R. Coleman, J. Wess and B. Zumino, *Structure of phenomenological Lagrangians. 2.*, *Phys. Rev.* **177** (1969) 2247.
- [38] D. B. Kaplan, *Flavor at SSC energies: A new mechanism for dynamically generated fermion masses*, *Nuclear Physics B* **365** (1991) 259 .
- [39] A. De Simone, O. Matsedonskyi, R. Rattazzi and A. Wulzer, *A first top partner hunter's guide*, *Journal of High Energy Physics* **2013** (2013) .
- [40] ATLAS, CMS collaboration, G. Aad et al., *Measurements of the Higgs boson production and decay rates and constraints on its couplings from a combined ATLAS and CMS analysis of the LHC pp collision data at $\sqrt{s} = 7$ and 8 TeV*, *JHEP* **08** (2016) 045 [[1606.02266](#)].
- [41] K. Agashe, G. Perez and A. Soni, *Flavor structure of warped extra dimension models*, *Physical Review D* **71** (2005) .
- [42] T. Gherghetta and A. Pomarol, *Bulk fields and supersymmetry in a slice of AdS*, *Nuclear Physics B* **586** (2000) 141–162.

- [43] M. Redi and A. Weiler, *Flavor and CP invariant composite Higgs models*, *Journal of High Energy Physics* **2011** (2011) .
- [44] Wolfram Research, *Mathematica 8.0*, 2010.
- [45] D. Liu, L. T. Wang and K. Xie, *Prospects of searching for composite resonances at the LHC and beyond*, *JHEP* **01** (2019) 157 [[1810.08954v2](#)].
- [46] A. Carvalho, M. Dall’Osso, T. Dorigo, F. Goertz, C. A. Gottardo and M. Tosi, *Higgs Pair Production: Choosing Benchmarks With Cluster Analysis*, *JHEP* **04** (2016) 126 [[1507.02245](#)].
- [47] A. Alloul, N. D. Christensen, C. Degrande, C. Duhr and B. Fuks, *FeynRules 2.0 - A complete toolbox for tree-level phenomenology*, *Comput. Phys. Commun.* **185** (2014) 2250 [[1310.1921](#)].
- [48] J. Alwall, R. Frederix, S. Frixione, V. Hirschi, F. Maltoni, O. Mattelaer et al., *The automated computation of tree-level and next-to-leading order differential cross sections, and their matching to parton shower simulations*, *JHEP* **07** (2014) 079 [[1405.0301](#)].
- [49] E. Conte, B. Fuks and G. Serret, *MadAnalysis 5, A User-Friendly Framework for Collider Phenomenology*, *Comput. Phys. Commun.* **184** (2013) 222 [[1206.1599](#)].
- [50] R. Contino, M. Ghezzi, M. Moretti, G. Panico, F. Piccinini and A. Wulzer, *Anomalous Couplings in Double Higgs Production*, *JHEP* **08** (2012) 154 [[1205.5444](#)].
- [51] M. Cepeda et al., *Report from Working Group 2: Higgs Physics at the HL-LHC and HE-LHC*, vol. 7, pp. 221–584. 12, 2019. [1902.00134](#). 10.23731/CYRM-2019-007.221.
- [52] CMS collaboration, *Sensitivity projections for Higgs boson properties measurements at the HL-LHC*, *CMS-PAS-FTR-18-011* (2018) .
- [53] ATLAS collaboration, *Projections for measurements of Higgs boson cross sections, branching ratios, coupling parameters and mass with the ATLAS detector at the HL-LHC*, *ATL-PHYS-PUB-2018-054* (2018) .
- [54] R. Di Nardo et al., *Combination of Higgs Boson Measurement Projections*, [1902.00134](#).
- [55] ATLAS collaboration, M. Aaboud et al., *Search for pair production of Higgs bosons in the $b\bar{b}b\bar{b}$ final state using proton-proton collisions at $\sqrt{s} = 13$ TeV with the ATLAS detector*, *JHEP* **01** (2019) 030 [[1804.06174](#)].
- [56] CMS collaboration, A. M. Sirunyan et al., *Search for nonresonant Higgs boson pair production in the $b\bar{b}b\bar{b}$ final state at $\sqrt{s} = 13$ TeV*, *JHEP* **04** (2019) 112 [[1810.11854](#)].
- [57] A. Arganda, C. Garcia-Garcia and M. Herrero, *Probing the Higgs self-coupling through double Higgs production in Vector Boson scattering at the LHC*, *Nucl. Phys.* **B945** (2019) 114687.
- [58] ATLAS collaboration, G. Aad et al., *Search for the $HH \rightarrow b\bar{b}b\bar{b}$ process via vector-boson fusion production using proton-proton collisions at $\sqrt{s} = 13$ TeV with the ATLAS detector*, *JHEP* **07** (2020) 108 [[2001.05178](#)].
- [59] C. Englert, F. Krauss, M. Spannowsky and J. M. Thompson, *Di-Higgs Phenomenology in $t\bar{t}h$ channel: the forgotten channel*, *Phys. Lett.* **B743** (2015) 93.
- [60] S. Banerjee, F. Krauss and M. Spannowsky, *Revisiting the $t\bar{t}h$ channel at the FCC-hh*, *Phys. Rev.* **D100** (2019) 073012.

- [61] M. Gillioz, R. Gröber, C. Grojean, M. Mühlleitner and E. Salvioni, *Higgs low-energy theorem (and its corrections) in composite models*, *Journal of High Energy Physics* **2012** (2012) .
- [62] A. M. Sirunyan, A. Tumasyan, W. Adam, F. Ambrogio, T. Bergauer, J. Brandstetter et al., *Measurement of top quark pair production in association with a Z boson in proton-proton collisions at $\sqrt{s} = 13$ TeV*, *Journal of High Energy Physics* **2020** (2020) .
- [63] ATLAS collaboration, M. Aaboud et al., *Measurement of the $t\bar{t}Z$ and $t\bar{t}W$ cross sections in proton-proton collisions at $\sqrt{s} = 13$ TeV with the ATLAS detector*, *Phys. Rev. D* **99** (2019) 072009 [[1901.03584](#)].
- [64] anc/* in the source of the arXiv version of this manuscript.
- [65] N. Arkani-Hamed, T. Han, M. Mangano and L.-T. Wang, *Physics opportunities of a 100 TeV proton-proton collider*, *Phys. Rept.* **652** (2016) 1 [[1511.06495](#)].
- [66] T. Golling et al., *Physics at a 100 TeV pp collider: beyond the Standard Model phenomena*, *CERN Yellow Rep.* (2017) 441 [[1606.00947](#)].
- [67] R. Contino et al., *Physics at a 100 TeV pp collider: Higgs and EW symmetry breaking studies*, *CERN Yellow Rep.* (2017) 255 [[1606.09408](#)].
- [68] G. F. Giudice, C. Grojean, A. Pomarol and R. Rattazzi, *The strongly-interacting light Higgs*, *Journal of High Energy Physics* **2007** (2007) 045–045.